Bellcomm, Inc.

TR-69-103-7-1

NATURAL ENVIRONMENT AND PHYSICAL STANDARD DATA FOR MARS, VENUS AND INTER-PLANETARY SPACE THROUGH THE ASTEROID BELT

MARCH, 1969

M. Liwshitz, Editor

Work performed for Manned Space Flight, National Aeronautics and Space Administration under Contract NASW-417.

INTRODUCTION

This document compiles the natural environment and physical standard data, in preliminary form, to provide a uniform basis for specific planetary and interplanetary mission studies. Data on the physical environment in interplanetary space and on the physical environment of the planets Mars and Venus are presented. The only astrodynamical data presented are a few fundamental constants on the planets. It does not cover the earth's magnetosphere or the moon, nor does it include values for the induced environment of space vehicles. Where the effect of the natural environment on space vehicles or space missions is not obvious, an effort has been made to point out briefly potential effects induced by the environment.

The explanatory background material, necessary for understanding and use of environmental data, by both engineers and scientists in need of data beyond their immediate fields of specialization, is included. Whenever authoritative values for environmental data are available, they are used. A limited range of values is presented in the area where agreed upon data are lacking, with preferred values indicated wherever possible. In case of highly controversial or uncertain data, a proper caveat is included in the data presentation. Reference lists are included. The cgs unit system is used, except where other units are in exclusive use by the majority of workers in a field.

Different sections in this document were supplied by experts in the corresponding fields, and their assistance is hereby acknowledged. Special thanks are due to A. C. Buffalano, J. S. Dohnanyi and R. H. Hilberg of Bellcomm, Inc., who provided the major part of entire chapters, to Dr. B. G. Smith, who had a major share in the initial stages of this project, and to many colleagues in the general scientific community, who were frequently consulted on specific questions.

TABLE OF CONTENTS

INTRODUCTION

PART I. INTERPLANETARY SPACE

CHAPTER IA. SOLAR ELECTROMAGNETIC RADIATION

(a) Introduction IA-1

(b) General Structure IA-2

(c) Black-Body Steady State Solar Radiation IA-4

(d) Fraunhofer Lines IA-5

(e) Non-Black Body Radiation in the UV IA-7

(f) Variations in Solar Activity IA-9

(g) Solar Cycle Variations in the Radio Emission IA-9

(h) Short Time Scale Variations in the Radio Emission IA-11

(i) Variations in the Solar Extreme Ultraviolet Emission between 200-1215.7Å IA-11

(j) Variations in Solar X-Ray Emission IA-15

References IA-17

CHAPTER IB. NON-SOLAR ELECTROMAGNETIC RADIATION

(a) Introduction IB-1

(b) Reflection of Light by Planetary Bodies and Their Gray-Body Emission IB-1

(c) Photometric Parameters of Planetary Bodies IB-2

(d) Planetary Radio Emission IB-4

(e) Electromagnetic Radiation Originating Outside the Solar System IB-4

References IB-7

TABLE OF CONTENTS (Cont'd)

CHAPTER IC. SOLAR WIND, INTERPLANETARY GAS AND MAGNETIC FIELDS

(a) Introduction IC-1

(b) Density and Composition IC-1

(c) Mean Velocity, Random Motions and Temperature in the Solar Wind IC-2

(d) Magnetic Fields IC-4

(e) Solar Wind Interaction with the Geomagnetic Field IC-6

(f) Solar Storms IC-8

(g) Termination of the Solar Wind IC-9

References IC-10

CHAPTER ID. SOLAR COSMIC RADIATION

(a) Introduction ID-1

(b) Composition, Energy Range, Flux and Total Energy ID-1

(c) Intensity and Spectra of Cosmic Rays ID-1

(d) Variations with Solar Distance ID-4

(e) Time Development of Solar Events ID-4

(f) Momentum Spectrum ID-7

(g) Statistics of Solar Events ID-7

(h) Dosage and Shielding ID-9

References ID-10

CHAPTER IE. GALACTIC COSMIC RADIATION

(a) Flux and Energy Spectrum IE-1

(b) Composition IE-1

TABLE OF CONTENTS (Cont'd)

CHAPTER IE. GALACTIC COSMIC RADIATION (Cont'd)

(c) Dosage and Shielding IE-1

References IE-3

CHAPTER IF. METEOROID ENVIRONMENT

(a) Introduction IF-1

(b) Cometary Meteoroids IF-1

(c) Asteroidal Meteoroids IF-3

(d) Meteorites IF-4

(e) Meteor Showers IF-5

(f) Calculation of Particle Fluxes IF-5

(g) Meteoroid Fluxes at Planetary Surfaces IF-6

(h) Penetration Mechanics IF-6

References IF-9

PART II. MARS

CHAPTER IIA. GENERAL PHYSICAL PROPERTIES OF MARS

(a) Introduction IIA- 1

(b) Geometric and Photometric Relationships Related to Planetary Observations IIA- 1

(c) Photometric Properties of Mars IIA- 5

(d) Polarimetry IIA- 7

(e) Radar Reflectivity and Scattering by Mars IIA- 9

(f) Gross Thermal Properties IIA-11

(g) Magnetic Field and Radiation Belts IIA-12

(h) Satellites IIA-12

References IIA-13

TABLE OF CONTENTS (Cont'd)

CHAPTER IIB. SURFACE PROPERTIES OF MARS

(a) General Appearance IIB-1

(b) Polar Caps IIB-1

(c) Bright Areas IIB-3

(d) Dark Areas IIB-3

(e) Thermal Properties IIB-3

(f) Topography IIB-5

(g) Soil Mechanics IIB-7

References IIB-8

CHAPTER IIC. ATMOSPHERIC PROPERTIES OF MARS

(a) Composition IIC-1

(b) Temperature Profile IIC-2

(c) Pressure and Density Profiles IIC-4

(d) Ionosphere IIC-6

(e) Clouds and Haze IIC-10

(f) Wind IIC-10

References IIC-12

PART III. VENUS

CHAPTER IIIA. GENERAL PHYSICAL PROPERTIES OF VENUS

(a) Introduction IIIA-1

(b) Geometric and Photometric Relationships IIIA-3

(c) Photometric Properties of Venus IIIA-3

(d) Polarimetry IIIA-3

TABLE OF CONTENTS (Cont'd)

CHAPTER IIIA. GENERAL PHYSICAL PROPERTIES OF VENUS (Cont'd)

(e) Radar Reflectivity and Scattering IIIA-3

(f) Gross Thermal Properties IIIA-7

(g) Magnetic Field and Radiation Belts IIIA-8

References IIIA-9

CHAPTER IIIB. SURFACE PROPERTIES OF VENUS

(a) Introduction IIIB-1

(b) Topography IIIB-2

(c) Surface Composition and Texture IIIB-6

(d) Thermal Properties IIIB-6

References IIIB-7

CHAPTER IIIC. ATMOSPHERIC PROPERTIES OF VENUS

(a) Composition IIIC-1

(b) Temperature Profile IIIC-2

(c) Pressure and Density Profiles IIIC-4

(d) Ionosphere IIIC-6

(e) Clouds and Haze IIIC-6

(f) Circulation and Winds IIIC-7

(g) Attenuation of High Frequency Radio Waves IIIC-7

References IIIC-15

LIST OF FIGURES

FIGURE		PAGE
IA1	The Solar Electromagnetic Radiation Spectrum	IA-3
IA2	Solar Spectral Irradiance above the Earth's Atmosphere	IA-6
IA3	Variation with Wavelength of Planckian Temperature in Solar Ultraviolet Continuum	IA-8
IA4	Solar Ultraviolet Irradiance at 1 AU Between 700 and 2100A	IA-8
IA5	Predicted and Observed Sunspot Numbers	IA-10
IA6	Relation Between Flux Density at 10.7 cm and the Sunspot Number for the IGY Period	IA-12
IA7	Monthly Mean Solar 10.7 cm Fluxes and Relative Sunspot Numbers from 1947 to 1963	IA-12
IA8	Motion of Active Centers Across the Sun	IA-14
IA9	Solar Ultraviolet Irradiance below 1000A at 1 AU	IA-14
IB1	Maximum Microwave Flux Density for each Planet and two Satellites	IB-5
IB2	Radio Maps of a Galactic Region	IB-6
IC1	The Solar Ecliptic Coordinate System	IC-3
IC2	Proton Velocity Contour Mappings	IC-3
IC3	A Polar Plot of Temperature, Defined in Terms of V^2_{Random}	IC-5
IC4	Topology of the Solar Magnetic Field	IC-5
IC5	Schematic Diagram of Interaction of Solar Wind with the Magnetosphere	IC-7
ID1	Distribution of Characteristic Rigidity	ID-3

LIST OF FIGURES (Cont'd)

FIGURE	TITLE	PAGE
ID2	NEPSAP Model Solar Cosmic Ray Event	ID-3
ID3	Integral Flux Distribution	ID-6
ID4	Size Distribution of Solar Particle Events	ID-6
ID5	Size Distribution of Solar Particle Events	ID-8
ID6	Probability per Mission of an Occurrence of a Solar Cosmic Ray Event	ID-8
IE1	Galactic Cosmic Ray Differential Energy Spectra	IE-2
IE2	Doses Resulting from Galactic Cosmic Rays	IE-2
IF1	Mass Distribution of Meteoroids	IF-2
IIA1	Geometric Relationship for Photometric and Polarimetric Description	IIA-2
IIA2	Spectral Variation of Phase Integral and Spherical Albedo	IIA-2
IIA3	Visual Phase Function of Mars	IIA-6
IIA4	Contour Map of Equal Relative Brightness for the Planet Mars	IIA-6
IIA5	Average Polarization Curve of Light Regions on Mars	IIA-8
IIA6	Variation of Martian Radar Cross Cross Section	IIA-8
IIB1	Latitude Boundaries of the Polar Caps and the Darkening Wave on Mars	IIB-2
IIB2	Average Martian Isotherms	IIB-4

LIST OF FIGURES (Cont'd)

FIGURE	TITLE	PAGE
IIB3	Diurnal Variation of Surface Temperature in the Equatorial Region of Mars	IIB-6
IIB4	Martian Height Profile at 21°N Latitude	IIB-6
IIC1	Atmospheric Temperature Profile of Mars	IIC-3
IIC2	Atmospheric Density Profile of Mars	IIC-3
IIC3	Atmospheric Pressure Profile	IIC-5
IIC4	Mean Zonal and Meridional Wind Profiles for Mars	IIC-5
IIIA1	Visual Phase Function of Venus	IIIA-2
IIIA2	Visual Polarization Curves of Venus	IIIA-4
IIIA3	Polarization Curves of Venus in the Infrared	IIIA-4
IIIA4	The Radar Cross Section of Venus vs Wavelength	IIIA-6
IIIA5	The Observed Microwave Brightness Temperature of Venus	IIIA-6
IIIB1	CW Radar Spectrum of Venus	IIIB-3
IIIB2	$P(\phi)$, Backscattering Function of Venus	IIIB-3
IIIB3	The Mean Radar Angular Power Spectrum of Venus	IIIB-5
IIIB4	Typical Model of Isotherms on Venus	IIIB-5
IIIC1	Atmospheric Temperature Profile of Venus	IIIC-3
IIIC2	Atmospheric Pressure Profile of Venus	IIIC-3

LIST OF FIGURES (Cont'd)

FIGURE	TITLE	PAGE
IIIC3	Atmospheric Density Profile of Venus	IIIC-5
IIIC4	Ionospheric Electron Profiles of Venus	IIIC-5
IIIC5	Suggested Circulation in the Atmosphere of Venus	IIIC-7
IIIC6	Computed Wind Velocities for Venus	IIIC-7

(I) INTERPLANETARY SPACE

(IA) SOLAR ELECTROMAGNETIC RADIATION

(a) INTRODUCTION

The dominant source of electromagnetic radiation in interplanetary space is the sun. Table IA.1 provides a summary of important physical parameters related to the sun's dimensions and its position in interplanetary space [Allen, 1963; Landolt-Börnstein, 1965; NASA-SE 015-001-1, 1965; Melbourne et al., 1968].

Table IA.1

Important solar parameters

Ratio of sun's mass to earth's mass	332945.6
Gravitational parameter	$1.32712499 \times 10^{26}$ cm^3 sec^{-2}
Radius	6.95992×10^{10} cm
Angular rotation velocity (at 16° latitude)	2.87×10^{-6} radian sec^{-1}
Mean distance from earth ≡ 1 AU	$1.49597893 \times 10^{13}$ cm
Semi-diameter at 1 AU	0.004652 radian =959.63"
Apparent visual magnitude	-26.78

Owing to the high opacity of solar gases, the observed solar radiation originates in the sun's outer envelope, the *solar atmosphere*. Three distinctive layers in the sun's atmosphere are recognized on account of their different physical and radiative properties:

1) *Photosphere* - defined as the gaseous shell extending from the sun's outer edge, as observed in visible light, down to the level at which gases become completely opaque. The depth of the photosphere is $\sim$350 km, and its effective average temperature is $\sim$5800°K. The photosphere accounts for the overwhelming portion of solar electromagnetic radiation.

2) *Chromosphere* - observed as the red ring during total solar eclipses, when the sun's bright disk is occulted by the moon. Its thickness is $\sim$15000 km, and its temperature varies from $\sim$4400°K at its interface with the photosphere to $\sim 10^6$°K at its outer edge. Emission from the chromosphere dominates the solar spectrum between $\sim$100 and $\sim$1700 Å.

3) *Corona* - observed during eclipses as an extensive greenish-white halo, drawn out to tens of solar radii. The corona is the source of the sun's radio emission at meter wavelengths and of its emission of soft X-rays and ultraviolet radiation below 100 Å.

Section IA deals exclusively with phenomena associated with direct solar emission.

(b) GENERAL STRUCTURE

The observed spectrum of direct solar emission spans all wavelengths between X-rays of a few angstroms and the $\sim$30m cutoff of the ionosphere. The solar electromagnetic radiation is conveniently divided into three main categories:

1) Black-body steady state

2) Non-black-body steady state

3) Non-steady state

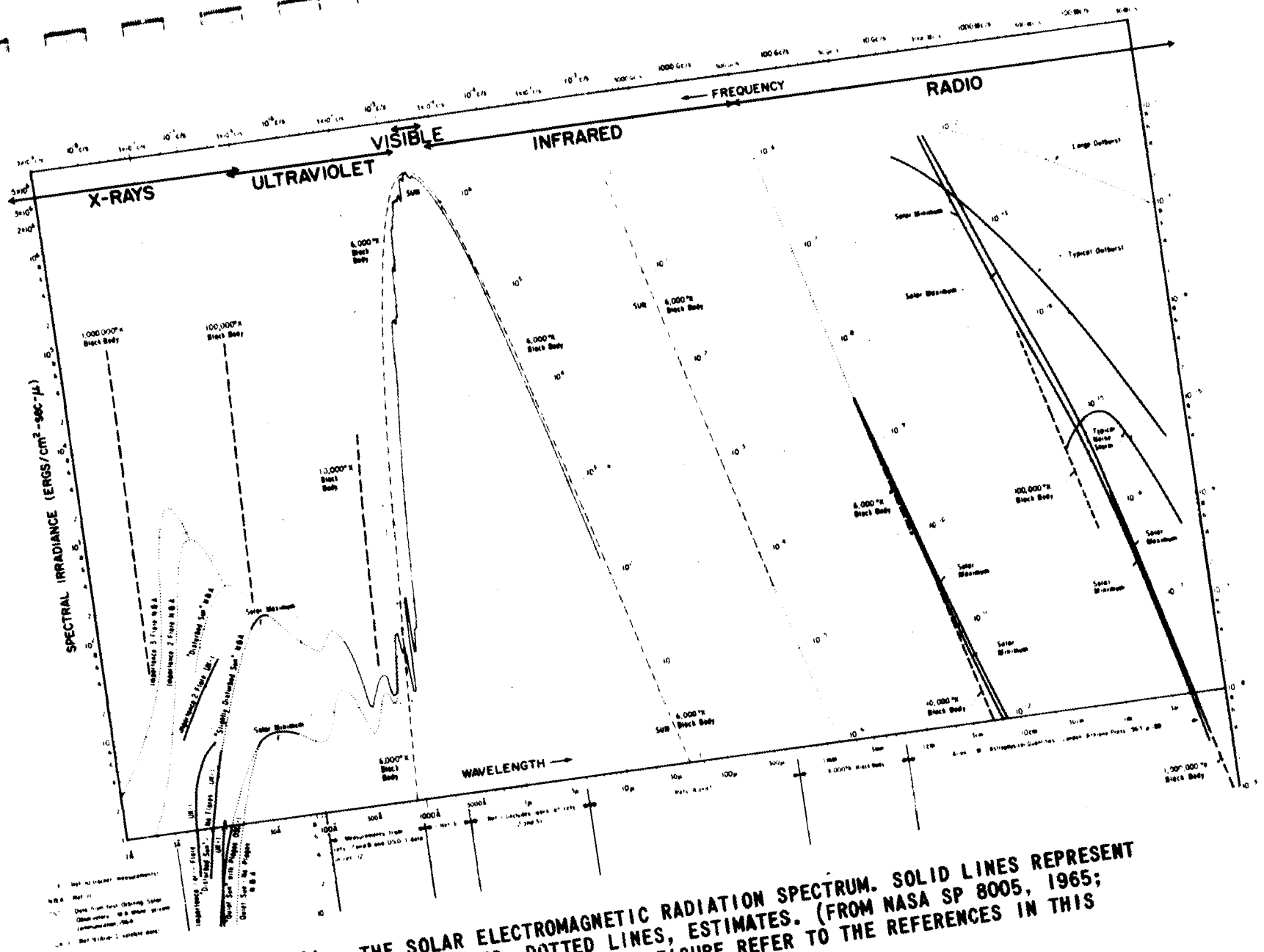

FIGURE IAI - THE SOLAR ELECTROMAGNETIC RADIATION SPECTRUM. SOLID LINES REPRESENT MEASUREMENTS; DOTTED LINES, ESTIMATES. (FROM NASA SP 8005, 1965; REFERENCE NUMBERS IN THE FIGURE REFER TO THE REFERENCES IN THIS DOCUMENT)

A concise survey of observational data on the solar radiation has recently been published by NASA [NASA SP-8005, 1965], containing a useful list of references. Figure IA1, from this document, illustrates the general structure of solar electromagnetic radiation.

(c) BLACK-BODY STEADY STATE SOLAR RADIATION

Black-Body steady state radiation encompasses the bulk of solar electromagnetic radiation. Its properties are summarized in Table IA.2.

Table IA.2

Characteristics of steady state solar black-body radiation

Equivalent overall effective black-body temperature	5800°K
Equivalent black-body temperature for the visible and infrared spectrum	6000°K
Solar Constant; defined as solar radiation intensity at 1 AU	2.00 cal cm^{-2} min^{-1} = 1.40 x 10^6 erg cm^{-2} sec^{-1} = 0.140 watt cm^{-2}
Radiation pressure at 1 AU on a body with albedo α	$(1+\alpha)$ x 4.67 x 10^{-5} dynes cm^{-2}
% of irradiance in the solar spectrum at 1 AU	
UV < 3800 Å	7.3% 0.146 cal $cm^{-2}min^{-1}$
3800 - 7500 Å	46.4% 0.928 cal $cm^{-2}min^{-1}$
Infrared > 7500 Å	46.3% 0.926 cal $cm^{-2}min^{-1}$
Peak irradiance	
4500 Å	0.22 watt cm^{-2} $micron^{-1}$
4750 Å	0.22 watt cm^{-2} $micron^{-1}$

Figure IA2 [Johnson, 1965] shows concisely the distribution of solar irradiance versus wavelength in the visible and near infrared.

Figure IA1 shows that solar radiation below $\sim$1000Å and above $\sim$1 cm is markedly time dependent. This reflects the origin of radiation at these wavelengths in the upper layers of the solar atmosphere which are subject to strong cyclic and transient variations. Between these limits the solar spectrum is quite constant in time, but displays varying departure from ideal blackbody radiation at 6000°K.

(d) FRAUNHOFER LINES

The Fraunhofer line spectrum comprises a series of dark lines observed in the solar spectrum from the UV through the infrared. The dark lines are due to absorption of the solar continuum radiation, emitted in the photosphere, by gases in higher layers of the solar atmosphere. Table IA.3 [Allen, 1963] lists the prominent Fraunhofer lines in the visible part of the spectrum. The Fraunhofer spectrum is the primary tool for identification of solar constituents.

Table IA.3
Prominent Fraunhofer lines in the visible spectrum

Atom	Name	λ (Å)
Ca II	K	3933.7
Ca II	H	3968.5
Fe I		4045.8
H I	Hδ	4101.7
H I	Hβ	4861.3
Mg I	b_1	5183.6
Na I	D_2	5890.0
Na I	D_1	5896.0
H I	Hα	6562.8

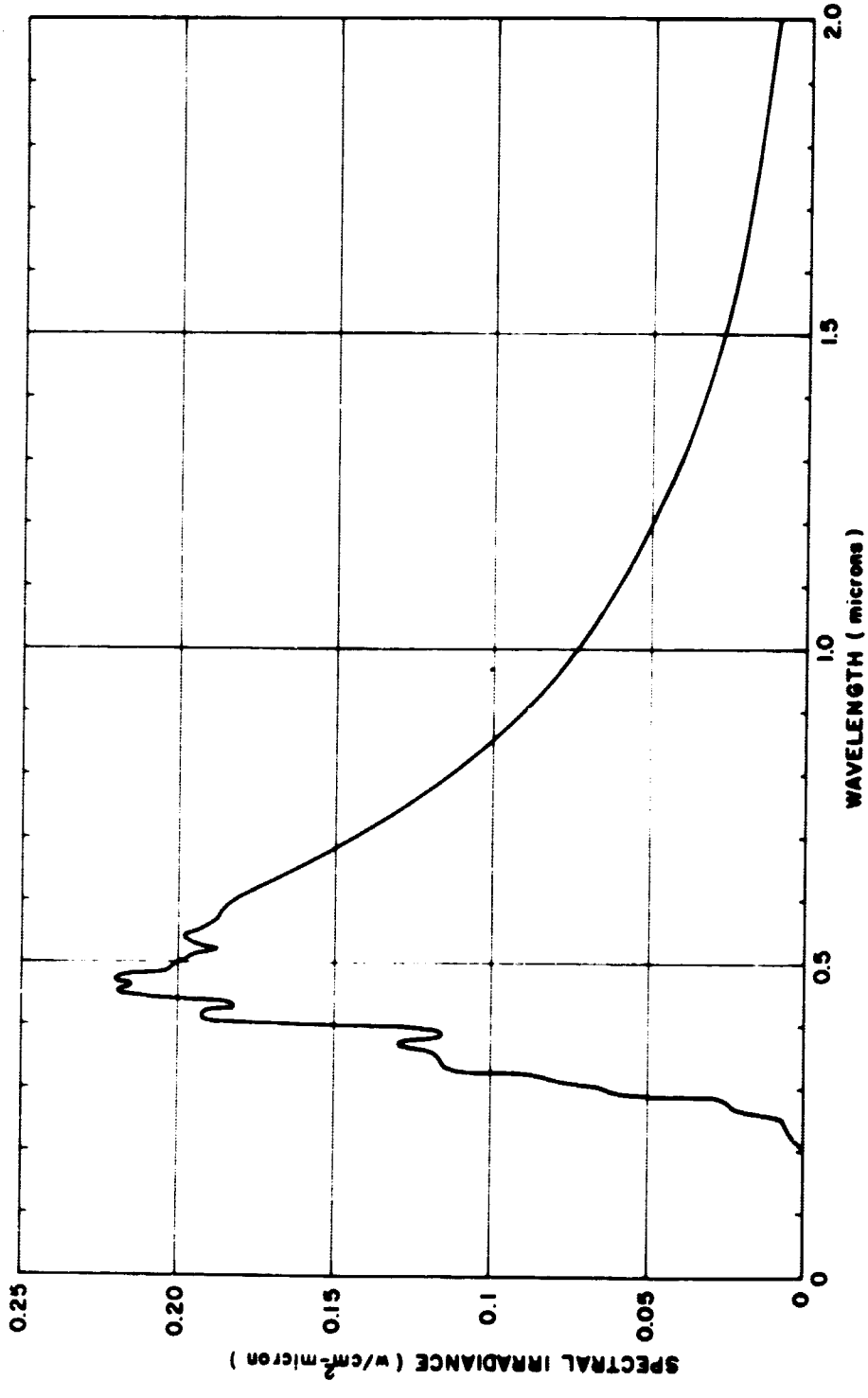

FIGURE IA2 - SOLAR SPECTRAL IRRADIANCE ABOVE THE EARTH'S ATMOSPHERE AT THE EARTH'S MEAN DISTANCE FROM THE SUN.
(FROM JOHNSON, 1965)

Though absorption in localized regions may be quite variable in time, the local variations will be usually obliterated in spectra taken over the entire disk, except in the case of a few selected lines, such as the Ca K line. Thus for most practical purposes, the Fraunhofer spectrum may be regarded as constant.

(e) NON-BLACK BODY RADIATION IN THE UV

Figure IA1 shows that below ∿4000 Å the solar spectrum departs from 6000°K black-body radiation, and displays time variations, which increase toward shorter wavelengths. The continuum down to 2085 Å is stable within ∿5%, and below 2500 Å corresponds to a Planckian temperature of ∿5500°K, as shown in Figure IA3 [Goldberg, 1967]. Between 2085 and 1216 Å solar radiation is stable within ∿50%, but displays a complex structure of emission lines superimposed on a continuum corresponding to ∿4700°K, as can be seen in Figures IA4 [Johnson, 1965] and IA3. Apart from the Lyman α region, most of the emitted energy is contained in the continuum. Table IA.4 lists prominent lines in the solar UV spectrum from 1215-2000 Å [Hinteregger, 1965].

Table IA.4
Prominent lines in the solar UV spectrum from 1000-2000Å

Line Identification	λ(Å)	Intensity (10^{-8} watt cm^{-2})a
H Ly-α	1215.67	51.0
C IV	1548.19	1.1
C I[b]	1657.00	1.6
Si II	1808.01	1.5
Si II[b]	1817.42	4.5
Si III	1892.03	1.0

a - within a 1Å bandwidth centered on line

b - blended with additional lines

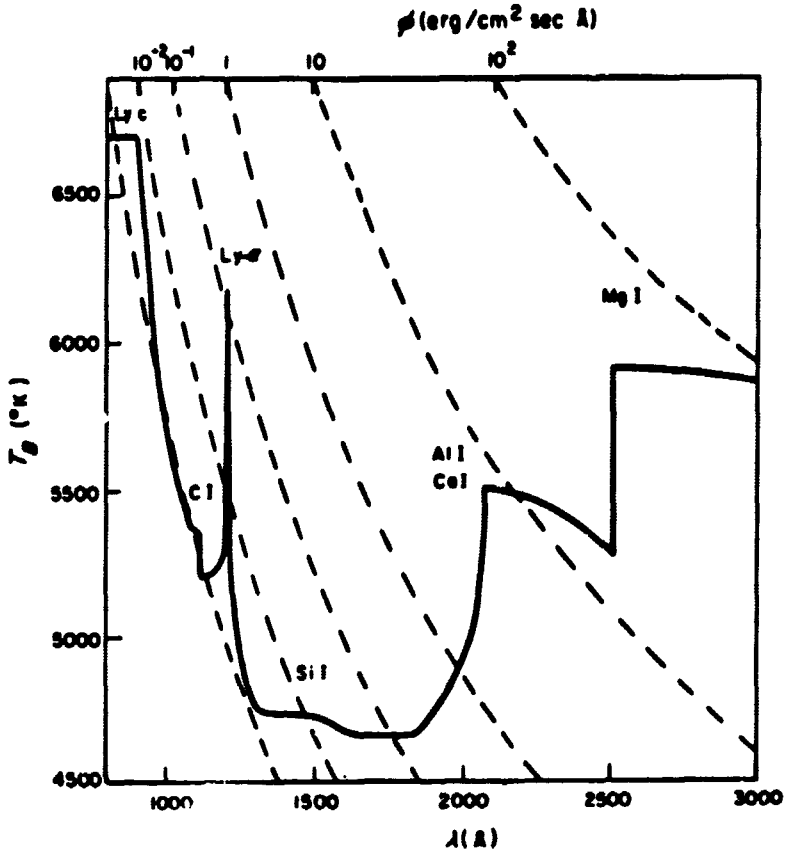

FIGURE IA3 - VARIATION WITH WAVELENGTH OF PLANCKIAN TEMPERATURE IN SOLAR ULTRAVIOLET CONTINUUM. THE SERIES LIMITS OF SEVERAL ABUNDANT NEUTRAL ATOMS ARE MARKED, AS IS THE POSITION OF LYMAN-α. ISOINTENSITY CONTOURS ARE ALSO DRAWN AT INTERVALS OF A FACTOR OF TEN (FROM GOLDBERG, 1967)

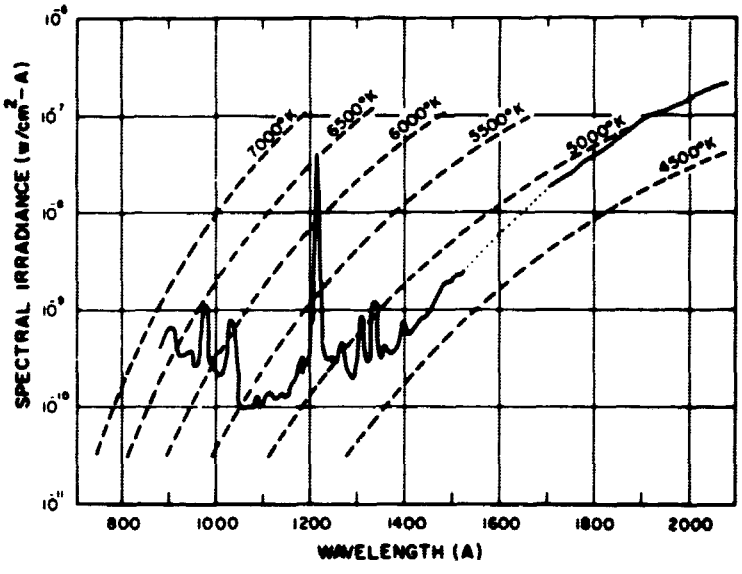

FIGURE IA4 - SOLAR ULTRAVIOLET IRRADIANCE AT 1 AU BETWEEN 700 AND 2100 A (FROM JOHNSON, 1965)

(f) VARIATIONS IN SOLAR ACTIVITY

Solar activity varies periodically with the mean solar cycle of ~11.4 years. Physical manifestations of variable solar activity are twofold:

1) periodic changes in the *frequency of occurrence of transient phenomena*, such as sunspots, solar flares, etc., these may be associated with short-lived, but copious production of corpuscular and electromagnetic radiation, such as X-ray and radio bursts;

2) periodic changes in the *average level of solar radiation* over certain frequency bands, such as emission of X-rays, EUV (extreme ultraviolet) and radio waves.

The most convenient index of varying solar activity is the so-called "sunspot number." This is the conventional measure of the frequency of sunspots, which are the most easily observed transient optical phenomena on the sun. The "sunspot number," which is relatively insensitive to observational bias, has been directly recorded since 1849, and earlier records, going back to ~1750, have been reduced to this measure [Kiepenheuer, 1953]. Figure IA5 [ESSA, 1967] is a plot of the monthly averages of sunspot numbers over the last two complete cycles and the present cycle through March 1967, and shows the mean of the last twelve cycles.

(g) SOLAR CYCLE VARIATIONS IN THE RADIO EMISSION

Figure IA1 shows that above ~1mm the quiet sun radio emission increasingly diverges from black body radiation at 6000°K. The variation of this departure with wavelength is evidence of the different altitudes of the regions of emission in the solar atmosphere, whose temperature increases from ~6000°K in the photosphere to ~10^6°K in the corona. Figure IA1 also shows the striking increase in solar radio emission with mounting solar activity, with the greatest relative difference between solar maximum and solar minimum occurring in the decimeter region.

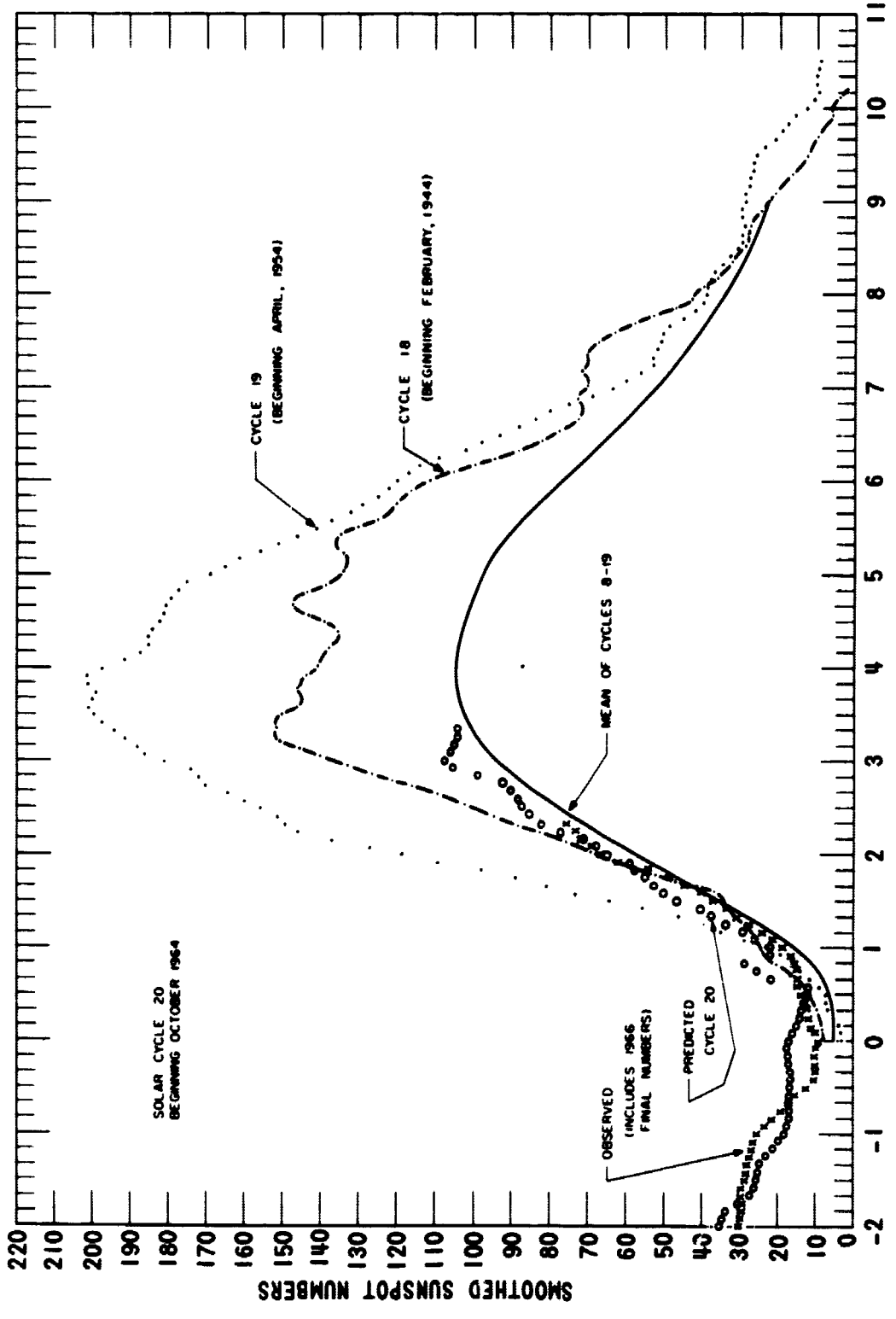

FIGURE IA5 - PREDICTED AND OBSERVED SUNSPOT NUMBERS (AFTER ESSA, 1967)

The solar radio emission at 10.7 cm, which has been continuously recorded since the mid-40's, is, indeed, another convenient index of solar activity. Its strong correlation with sunspot number is demonstrated in Figures IA6 [Smerd, 1964] and IA7 [Johnson, 1965]. The latter figure traces the cyclic variation of the mean monthly 10.7 cm solar radio noise flux since 1947.

(h) SHORT TIME SCALE VARIATIONS IN THE RADIO EMISSION

Superimposed on the general cyclic trend of solar radio emission are variations with varying time scales, short compared to the 11.4 year period. The "slowly varying component," with the longest time scale, shows a periodicity of $\sim$27 days, similar to sunspot frequency. It is responsible for the numerous wiggles in the upper curve of Figure IA7, which reflect the motion of active centers across the sun's visible disk, as illustrated in Figure IA8 [Steinberg and Lequeux, 1963].

On a yet shorter time scale are solar radio noise storms and bursts of various types. The characteristics of solar radio emission are summarized in Table IA.5 [Steinberg and Lequeux, 1963; Smith and Smith, 1963].

(i) VARIATION IN THE SOLAR EXTREME ULTRAVIOLET EMISSION BETWEEN 200-1215.7 Å

The total energy emitted by the sun between Hydrogen Lyman-α and 200 Å near solar minimum is about 7.0×10^{-7} watt cm^{-2} at 1 AU, of which $\sim 4.0 \times 10^{-7}$ watt cm^{-2} are due to Lyman-α [Hinteregger, 1968]. About one third of the remaining $\sim 3 \times 10^{-7}$ watt cm^{-2} is contained in prominent emission lines. Figure IA9 [Johnson, 1965] shows the major part of this spectral region.

Though systematic observations of this region cover only part of the preceding solar cycle, the intensity of the line spectrum displays considerable dependence on solar activity. This is indicated in Table IA.6

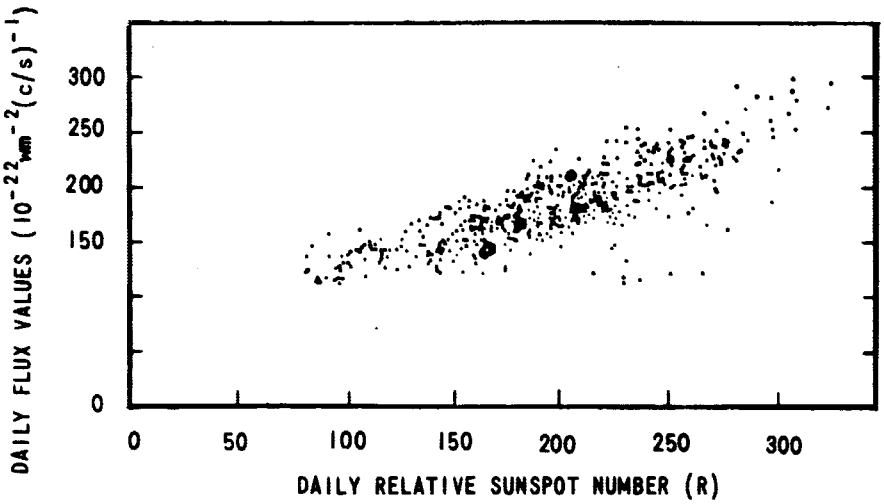

FIGURE IA6 - RELATION BETWEEN FLUX DENSITY AT 10.7 CM AND THE SUNSPOT NUMBER FOR THE IGY PERIOD (FROM SMERD, 1964)

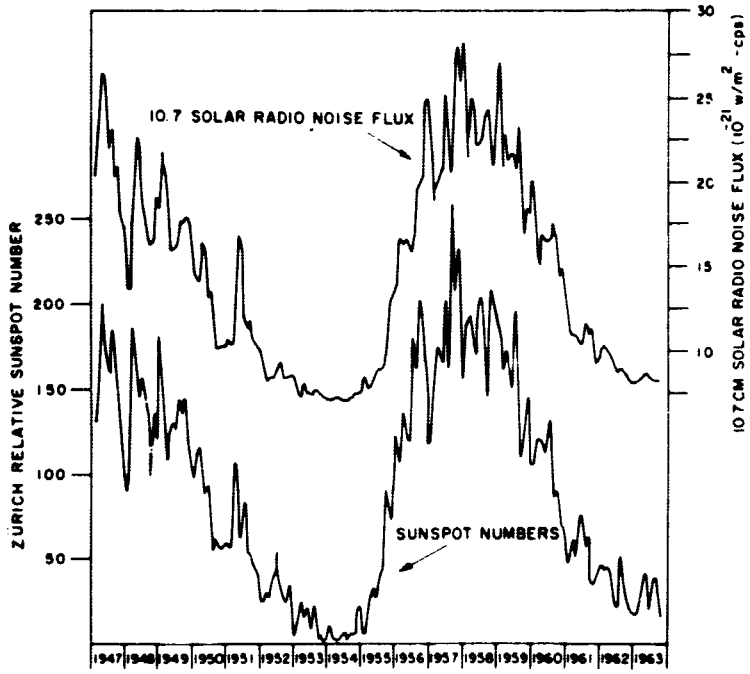

FIGURE IA7 - UPPER CURVE: MONTHLY MEANS OF 10.7-CM SOLAR RADIO-NOISE FLUX RECORDED BY COVINGTON AT NATIONAL RESEARCH COUNCIL, OTTAWA, CANADA (UNITS ARE 10^{-21} WATTS/M -CPS). LOWER CURVE: MONTHLY MEANS OF THE ZURICH RELATIVE SUNSPOT NUMBERS FROM 1947 TO 1963 (FROM JOHNSON, 1965)

TABLE IA.5

DIFFERENT TYPES OF SOLAR RADIO EMISSION

TYPE	DURATION	DIAMETER	APPARENT TEMPERATURE	INTENSITIES AT 100 Mc/s (WATTS/M^2-CPS)	SPECTRUM	POLARIZATION	ORIGIN	REMARKS
QUIET SUN	11-YEAR CYCLE?	~ 32', INCREASING WITH WAVELENGTH	10^6 K	3×10^{-22}	m,dm,cm	UNPOLARIZED	THERMAL	
SLOWLY VARYING COMPONENT	DAYS TO MONTHS	AS FOR SPOTS AND FACULAE	2×10^6 K	300 Mc/s: 50×10^{-22} 1000 Mc/s: 30×10^{-22}	dm,cm;m?	UNPOLARIZED	THERMAL	COMPLEX BEHAVIOR ON CM WAVELENGTHS WITH CIRCULAR POLARIZATION
TYPE III BURSTS	SECONDS; OFTEN IN GROUPS	UP TO 10' ? INCREASING WITH WAVELENGTH	10^{11} K	USUALLY 10^{-20}	m,dm; 5 Mc/s BANDWIDTH; FAST DRIFT	USUALLY UNPOLARIZED	PLASMA OSCILLATIONS ? SYNCHROTRON ? CERENKOV ?	CAUSED BY FAST-ESCAPING PARTICLES ? FLARE-ASSOCIATED
TYPE V BURSTS	MINUTES	LARGE	10^{11} K	OFTEN 10^{-19} TO 10^{-20}	m; WIDE BANDWIDTH	SOMETIMES ELLIPTICALLY POLARIZED	SYNCHROTRON	FOLLOWING TYPE III
TYPE II BURSTS	MINUTES COMPLEX	?	10^{11} K	OFTEN 10^{-19} TO 10^{-20}	m,dm; 50 Mc/s BANDWIDTH; SLOW DRIFT	USUALLY UNPOLARIZED	PLASMA OSCILLATIONS	DUE TO SHOCK WAVE; FOLLOWS START OF FLARE
TYPE IV BURSTS	MINUTES TO HOURS	UP TO 10'; INCREASING WITH WAVELENGTH	10^{11} K	OFTEN 10^{-19} TO 10^{-20}	m,dm,cm	OFTEN CIRCULARLY POLARIZED	SYNCHROTRON	OFTEN 10 TO 20 MIN AFTER FLARE; UPWARD MOTION; COSMIC RAY ASSOCIATION
NOISE STORMS	HOURS TO DAYS	SMALL (MINUTES OF ARC)	10^9 K	10^{-21} TO 10^{-19}	m	CIRCULARLY POLARIZED	CERENKOV ?	SIMULTANEOUS CONTINUUM AND SHORT BURSTS (TYPE I)

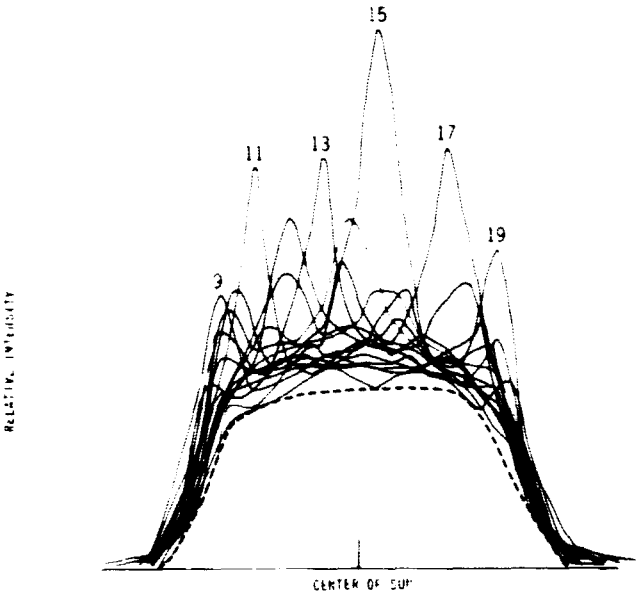

FIGURE IA8 - MOTION OF ACTIVE CENTERS ACROSS THE DISK OF THE SUN. SUPEROSITION OF 15 SOLAR INTERFEROGRAMS TAKEN ON 3 CM AT 2-DAY INTERVALS AT NANCAY
(FROM STEINBERG AND LEQUEUX, 1963)

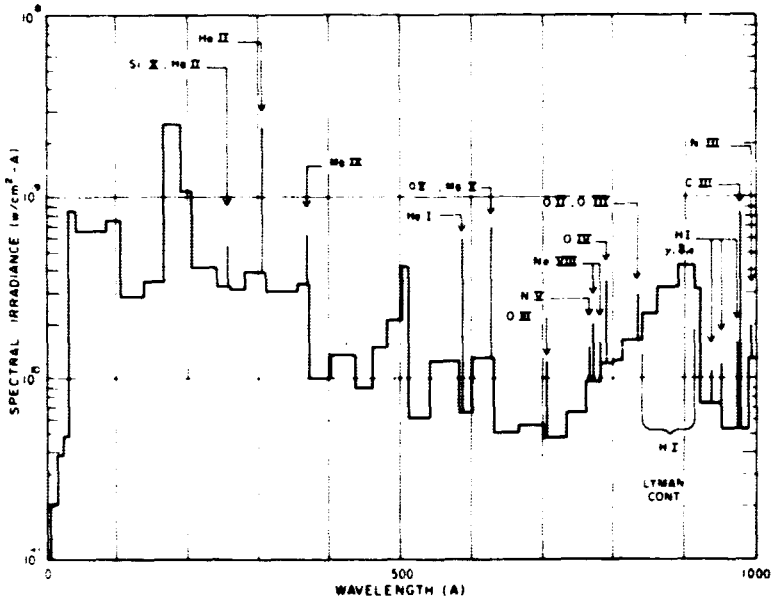

FIGURE IA9 - SOLAR ULTRAVIOLET IRRADIANCE BELOW 1000 A AT 1 AU. THE LINES ARE SHOWN AS IF THEY HAD AN EFFECTIVE LINE WITH OF 10 A
(FROM JOHNSON, 1965)

Hinteregger, 1965] where measurements taken at times of different solar activity [see Figure IA7] are compared. In view of the evidence for correlation between the 10.7 cm radio noise flux and EUV emission [Neupert, 1964], the following crude model is suggested for the solar cycle variation of energy flux contained in the EUV emission, until more complete information becomes available [Hinteregger, 1968]: the Lyman-α irradiance varies between $\sim$4 and $\sim$8 x 10^{-7} watt cm^{-2} between solar minimum and maximum; the irradiance in the remainder of the EUV spectrum, down to 200 Å, varies between $\sim$3 and $\sim$9 x 10^{-7} watts cm^{-2} over this time interval. In between a linear correlation with the 10.7 cm irradiance may be applied.

Table IA.6

Fluxes of solar EUV emission lines

(Unit = 10^9 Photons cm^{-2} sec^{-1})

Wavelength	Identification	(A) August 1961	(B) December 1963	Ratio (A)/(B)
1206.5	Si III	4.0	3.3	1.2
1025.7	H Ly-β	2.5	1.8	1.4
977.0	C III	4.0	3.0	1.3
770.4	Ne VIII	0.41	0.22	1.9
584.3	He I	0.89	0.42	2.1
335.0	Fe XVI	0.33	0.07	4.5
303.8	He II Ly-α	2.5	2.3	1.1

(j) VARIATIONS IN SOLAR X-RAY EMISSION

Below 200 Å both the quiescent and sporadic solar emission vary substantially over the solar cycle. The relative differences increase sharply with diminishing wavelengths. The total irradiance at 1 AU in this spectral region is $\sim$1.3 x 10^{-7} watt cm^{-2} near

solar minimum [Hinteregger, 1965]. The amplitude of solar cycle variations of irradiance in a number of observed X-ray bands is illustrated in Table IA.7 [Goldberg, 1967]. In the interim between extreme conditions, correlation of X-ray irradiance with the 10.7 cm radio flux is indicated [Landini et al., 1967].

Table IA.7

Quiescent solar X-ray irradiance

(Unit = 10^{-8} watt cm^{-2})

Spectral band	Solar minimum	Solar maximum
0-10 Å	10^{-12}	$\sim 3 \times 10^{-10}$
10-20 Å	10^{-11}	$\sim 1.5 \times 10^{-9}$
44-60 Å	10^{-9}	5×10^{-9}

Sporadic X-ray bursts may, temporarily, outweigh the quiescent solar emission at short wavelengths. These bursts are associated with active regions on the sun, such as flares and prominences, and last from a few seconds to tens of minutes. A large solar flare ("importance 3') may yield at 1 AU transient fluxes of up to 10^{-7} watt cm^{-2} in the 10-20 Å band, which is about 10^4 times the quiescent flux at solar minimum. At the same time the flux in the 44-60 Å band may also be $\sim 10^{-7}$ watt cm^{-2}, which is merely a hundredfold enhancement [De Jager, 1967].

(IA) SOLAR ELECTROMAGNETIC RADIATION - REFERENCES

Allen, C. W., Astrophysical Quantities, 2nd ed., University of London, The Athlone Press, London, 1963.

De Jager, C., "Note on solar hard X-ray bursts," Solar Physics, 2, 347-350, 1967.

ESSA, U. S. Dept. of Commerce, "Solar geophysical data," #277, Sept. 1967.

Goldberg, L., "Ultraviolet and X-rays from the sun," pp. 279-324, in Annual Review of Astronomy and Astrophysics, Vol. 5, L. Goldberg, D. Layzer and J. G. Phillips eds., Annual Reviews, Inc., Palo Alto, Calif., 1967.

Hinteregger, H. E., "Absolute intensity measurements in the extreme ultraviolet spectrum of solar radiation," Space Science Rev. 4, 461-497, 1965.

Hinteregger, H. E., Private communication, 1968.

Johnson, F. S., ed., Satellite Environment Handbook, Stanford University Press, 1965.

Kiepenheuer, K. O., "Solar activity," pp. 322-465, in The Sun, G. P. Kuiper ed., The University of Chicago Press, Chicago, Ill., 1953.

Landini, M., D. Russo and G. L. Tagliaferri, "Solar X-ray flux measured by the 1964-01-D solar radiation satellite during the I.Q.S.Y.," Planet. Space Sci., 15, 231-237, 1967.

Landolt-Bornstein, Numerical Data and Functional Relationships in Science and Technology, New Series, Group VI, Vol. 1, ch. 4.1, Springer Verlag, Berlin-Heidelberg-New York, 1965.

Melbourne, W. G., J. D. Mulholland, W. L. Sjogren and F. M. Sturms, Jr., "Constants and related information for astrodynamic calculations, 1968," Tech. Rep. 32-1306, J.P.L., 1968.

NASA, SE 015-001-1, "Natural environment and physical standards for the Apollo Program," April 1965.

NASA, SP-8005, "Solar electromagnetic radiation," June 1965.

Neupert, W. M., "Intensity variations in the solar extreme ultraviolet spectrum observed by OSO-1," Ann. d'Astrophys., 28, 446-456,1965.

Smerd, S. F., "Solar radio emissions," pp. 65-114 in Research in Geophysics, H. Odishaw ed., The M.I.T. Press, Cambridge, Mass., 1964.

Smith, H. J. and E. S. Smith, Solar Flares, MacMillan, New York, 1963.

Steinberg, J. L. and J. Lequeux, Radio Astronomy, McGraw-Hill, New York, 1963.

(IB) NON-SOLAR ELECTROMAGNETIC RADIATION

(a) INTRODUCTION

Except for part of the radio emission from Jupiter, the bulk of electromagnetic radiation in interplanetary space, not directly supplied by the sun, is due either to the sun's reflected energy, or to solar energy absorbed and re-radiated in a different region of the spectrum. Only planetary bodies contribute a significant amount of radiation, other bodies in the solar system being either too small, such as meteors, or of transitory character, such as comets.

(b) REFLECTION OF LIGHT BY PLANETARY BODIES AND THEIR GRAY-BODY EMISSION

Reflected light in the solar system is mostly directly reflected sunlight. A notable exception is the "dark side" radiance of planetary satellites, such as the moon. The intensity of light reflected by a body, in the region of wavelength centered on λ, is the product of the *spectral albedo* α_λ and the intensity of light intercepted by the body in this region. For the total reflected light intensity a *mean albedo* α is substituted. A *gray body*, at temperature T, emits radiation with a spectral distribution equal to that of a black body of the same temperature, but with an intensity diminished by the factor $(1-\alpha)$, where α is constant. Consequently, a planetary body at temperature T, considered as a gray body with albedo α, radiates energy with a spectral intensity

$$F_\lambda = \frac{(1-\alpha) \times 3.741 \times 10^4}{\lambda^5 \left(e^{\frac{1.439 \times 10^4}{\lambda T}} - 1 \right)} \text{ watt cm}^{-2} \text{ micron}^{-1}$$

where λ is measured in microns. The total power radiated by the body is given by

$$F = (1-\alpha) \times 5.699 \times 10^{-12} T^4 \text{ watt cm}^{-2}$$

(c) PHOTOMETRIC PARAMETERS OF PLANETARY BODIES

The observed, or apparent, *brightness* of heavenly bodies is a function of the *luminous flux* from their surface and their distance from the observer. In the case of the planets the luminous flux itself depends on their albedo and their distance from the sun.

The traditional measure of apparent brightness is the *visual magnitude*, m_v, defined by

$$m_v = \mu_1 - 2.4 \log_{10} E$$

$\mu_1 = -14.05 \pm 0.05$, [de Vaucouleurs, 1964], a constant; E, measured in lumen m^{-2}, is the *illumination* at the point of observation. 1 lumen m^{-2} = 1 candela sterad m^{-2} = 1 lux.

In practice, only magnitude differences, or illumination ratios are measured. Thus, the observed illumination E produced by a celestial object, is given by

$$E = 6.95 \times 10^{-12} \times 10^{-0.416 m_v} \times E_{sun}$$

where E_{sun} is the solar illumination, and m_v the object's apparent visual magnitude.

For a planet, at distance R from the sun and Δ from the earth, the reduced magnitude, m_v', is defined by

$$m_v' = m_v - 5 \log R\Delta \quad .$$

This is the magnitude which would be observed at 1 AU from the planet, if the latter were itself 1 AU distant from the sun.

Table IB.1 presents photometric parameters of the planets, some of their satellites, as well as of some bright stars [Allen, 1963; deVaucouleurs, 1964]. For comparison the normalized visual magnitudes of the Echo I and Pageos satellites are included [Emmons et al, 1967]. These satellites are aluminized spheres of 100 ft. diameter.

Table IB.1

Photometric parameters of celestial objects

Object	Distance from sun in AU	Mean solar irradiance in cal cm^{-2} min^{-1}	Reduced visual magnitude	Mean opposition magnitude	Mean visual albedo
Sun	0	-	-26.78		
Mercury	0.39	13.4	- 0.39	-	0.058
Venus	0.72	3.8	- 4.37	-	0.705
Earth	1.00	2.0	- 3.87	-	0.380
Moon	"	"	+ 0.21	-12.74	0.068
Mars	1.52	0.87	- 1.49	- 1.98	0.159
Phopos	"	"	+11.99	+11.50	-
Deimos	"	"	+12.99	+12.50	-
Jupiter	5.20	0.08	- 9.20	- 2.50	0.58
Io	"	"	- 1.18	+ 5.52	0.73
Europa	"	"	- 1.03	+ 5.67	0.68
Ganymede	"	"	- 1.52	+ 5.18	0.34
Callisto	"	"	- 0.50	+ 6.20	0.13
Saturn	9.55	0.022	- 8.88	+ 0.70	0.57
Uranus	19.20	0.0055	- 7.17	+ 5.51	0.80
Neptune	30.10	0.0022	- 6.87	+ 7.85	0.71
Pluto	39.50	0.0013	- 1.01	+14.87	0.15
Sirius	5.56×10^5	-	-	- 1.4	-
Canopus	1.15×10^7	-	-	- 0.9	-
Vega	1.67×10^7	-	-	0.0	-
Polaris	4.12×10^7	-	-	2.0	-
Echo I	at 1609 km		0.009		
Pageos			0.003		

(d) PLANETARY RADIO EMISSION

The major part of the absorbed solar radiation is *thermally* emitted in the microwave range. In addition, Jupiter emits a strong flux of *non-thermal* radiation. Figure IB1 [after Smith and Carr, 1964] presents the maximum microwave flux from the planets, and the microwave flux from the quiet sun [Boischot, 1967].

(e) ELECTROMAGNETIC RADIATION ORIGINATING OUTSIDE THE SOLAR SYSTEM

Cosmic electromagnetic radiation spans the entire spectrum from γ rays to radio waves. Whereas visible radiation has been the subject of astronomy for many centuries, the exploration of other spectral regions is still in its infancy.

Various sources of X-rays have been discovered, and tentatively located within and without our galaxy. At the other end of the spectrum, the radio spectrum of the galaxy has been mapped at several wave lengths. At λ = 15m, the *brightness temperature* exceeds in some regions 250,000°K, whereas at 3.5 cm it drops in places to 10°K and less. Figure IB 2 [Steinberg and Lequeux 1963] presents partial maps of the galaxy, as observed at 22 cm, and 3.5 cm. These maps display a large number of discrete sources superimposed on a continuous background, and indicate the sharp reduction in radiation away from the galactic plane.

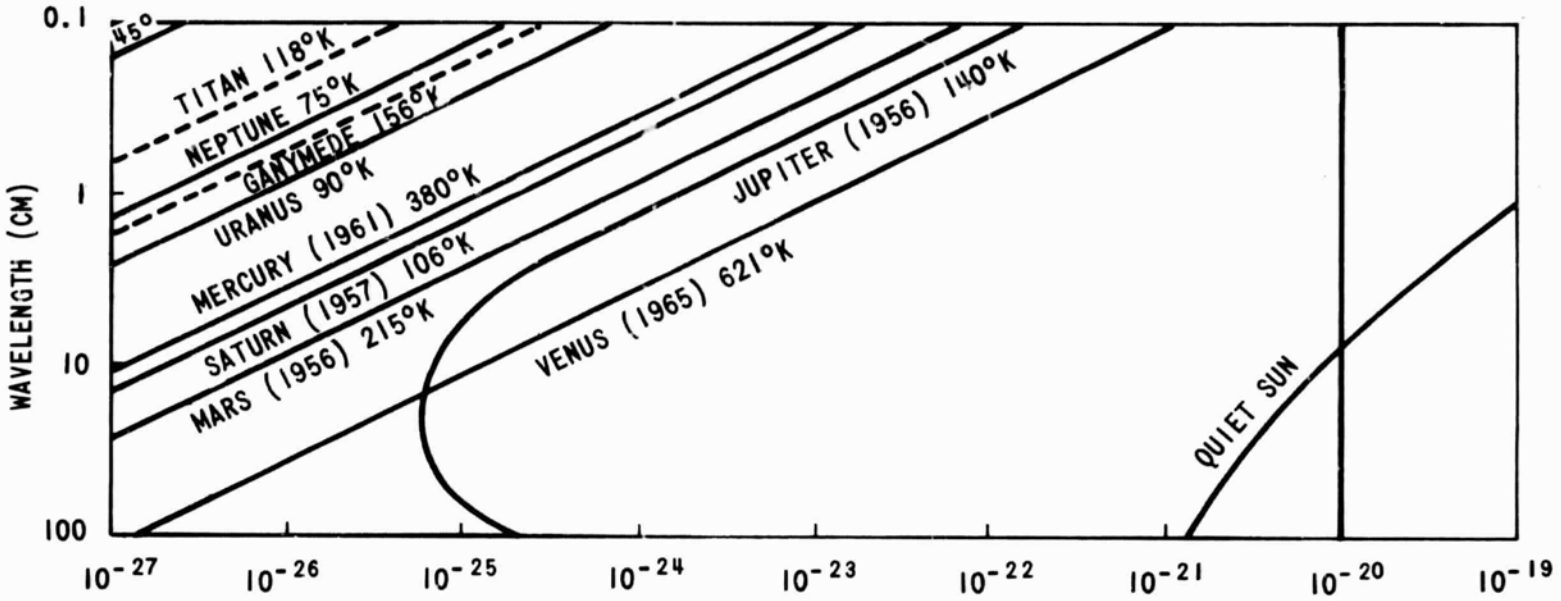

FIGURE IBI - MAXIMUM MICROWAVE FLUX DENSITY FOR EACH PLANET AND FOR TWO SATELLITES. THE UPTURNED TAIL ON THE JUPITER CURVE IS DUE TO NONTHERMAL EMISSION. FOR THE FIVE INNER PLANETS, NUMBERS IN PARENTHESES INDICATE THE DATE OF ACTUAL OBSERVATION. ALL CURVES APPLY TO MINIMUM DISTANCE OF THE BODY FROM THE EARTH EXCEPT FOR MERCURY, WHERE THE CURVE APPLIES TO MAXIMUM ANGULAR DISTANCE OF THE PLANET FROM THE SUN, WHICH IS THE ONLY CONDITION FOR WHICH SATISFACTORY OBSERVATION IS NOW POSSIBLE.

(AFTER SMITH AND CARR, 1963)

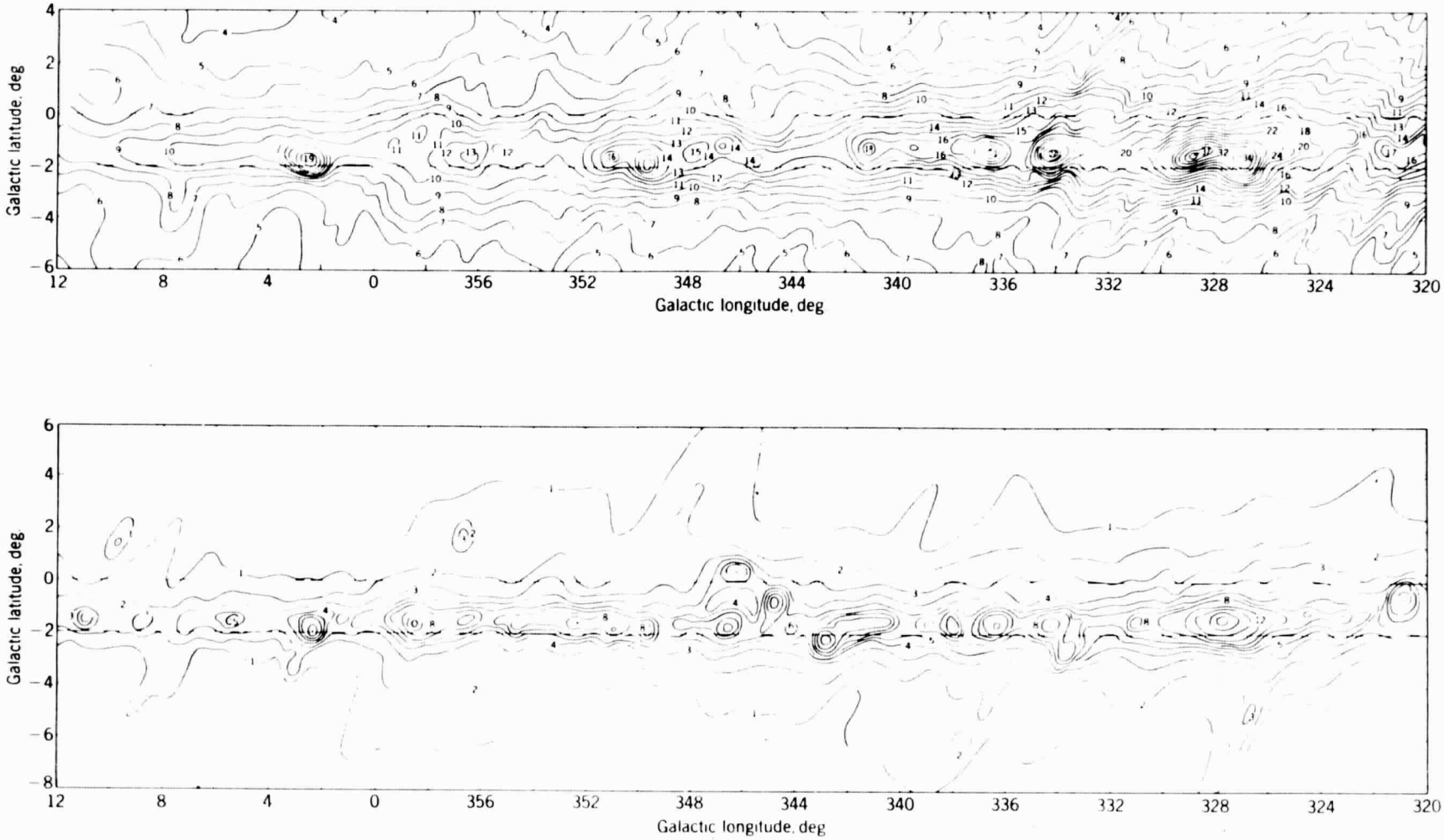

FIGURE IB2 - RADIO MAPS OF A GALACTIC REGION. UPPER MAP ON 3.5 m, CONTOUR UNIT IS 1000°K; LOWER MAP ON 22 cm, CONTOUR UNIT IS 3.25°K.

(FROM STEINBERG AND LEQUEUX, 1963)

(IB) NON-SOLAR ELECTROMAGNETIC RADIATION - REFERENCES

Allen, C. W., Astrophysical Quantities, 2nd ed., University of London, The Athlone Press, London, 1963.

Boischot, A., "Solar Radio Astronomy," in Solar Physics, J. Xanthakis ed., Interscience, London-New York-Sidney, 1967.

DeVaucouleurs, "Geometric and photometric parameters of the terrestrial planets," Icarus, 3, 187-235, 1964.

Emmons, R. H., C. L. Rogers and R. J. Preski, "Photometric observations of artificial satellites for determination of optical and physical characteristics I," Astron. J., 72, 939-944, 1967.

Smith, A. G. and T. D. Carr, Radio Exploration of the Planetary System, Van Nostrand, Princeton, N. J., 1964.

(IC) SOLAR WIND, INTERPLANETARY GAS AND MAGNETIC FIELDS

(a) INTRODUCTION

The sun is the source of particulate as well as electromagnetic radiation. Space probes and satellites have confirmed the existence of a continuous flux of low energy charged particles, called the solar wind, from the solar corona. This solar wind plasma, streaming nearly radially outward from the sun, behaves like a perfectly conducting fluid, whose energy density far exceeds that of the interplanetary magnetic field.

Effects of the solar wind (and its associated magnetic fields) are manifest on a variety of magnitude scales: its variation with solar activity modulates the penetration of galactic cosmic radiation [see Sec. (IE)] into the solar system; its interaction with planetary bodies affects their large scale physical environment, as in the case of the terrestrial magnetosphere or that of the Venusian ionosphere; finally, the solar wind flux plays a role in establishing the electric charge on a spacecraft moving in interplanetary space.

(b) DENSITY AND COMPOSITION

The solar wind is believed to be a *cold, collisionless, neutral plasma*; cold because its thermal energy is only about one hundredth of its streaming energy, and collisionless because the mean free path is roughly one astronomical unit. It is composed of electrons, protons H^+, alpha particles He^{++} and very small amounts of heavier ions. During the quiet periods of the sun, values of 3-5 protons cm^{-3}, 3-5 electrons cm^{-3} and .1-.2 alpha particles cm^{-3} are typical near the earth [Mackin and Neugebauer, 1966; Hundhausen et al., 1967]. Data taken on Mariners II and IV near the planets Venus and Mars are not inconsistent with a $1/r^2$ dependence of density on heliocentric distances in this region [Mackin and Neugebauer, 1966; Hundhausen et al., 1967].

The presence of a significant amount of neutral gas in interplanetary space has not yet been established. However, the presence of hydrogen atoms in interplanetary space has been invoked to explain in a satisfactory manner the Lyman-α radiation observed above one

hundred kilometers. Such neutrals might be solar protons which have undergone charge exchange with interstellar hydrogen atoms, and have been scattered back into the solar system, or they may be of terrestrial origin, surrounding the earth like the corona of a comet [Patterson et al., 1963; Brandt and Hodge, 1964].

(c) MEAN VELOCITY, RANDOM MOTIONS, AND TEMPERATURE IN THE SOLAR WIND

Observations indicate that all components of the solar wind move with the same mean velocity, v, and that v is independent of radius between .7 and 1.5 AU. v is typically 200-500 km sec^{-1} during quiet periods, and may increase to 500-800 km sec^{-1} during solar storms. These velocities correspond to proton energies in the range of keV, and electron energies in the range of eV. The flow appears to be radial, but deviations of $\pm 5°$ both from the earth-sun line and from the ecliptic plane have been recorded [Hundhausen et al., 1967]. Solar wind particle fluxes are typically of the order of 10^8 protons cm^{-2} sec^{-1}.

Solar wind particles appear to have a highly anisotropic, non-thermal random-velocity distribution function. The anisotropy is ascribed to the presence of a weak solar magnetic field, and has directional properties that are related to the magnetic field direction. On the assumption of symmetry of motion about the plane of the ecliptic, so that the mean velocity, v, lies in the plane of the ecliptic, the above anisotropy is best described in a solar ecliptic coordinate system, shown in Figure IC1 [Hundhausen et al., 1967]. Figure IC2 shows typical contour maps of the proton distribution function at 1 AU. The deviation of contours from circles indicates the deviation from isotropy in the random motion, and the asymmetry with respect to the v_1 axis indicates the departure of the solar wind flux from the earth-sun direction. Obviously both deviations are variable in time.

Owing to the anisotropy produced by the magnetic field it is common to define parallel and perpendicular particle temperatures, based on various measures

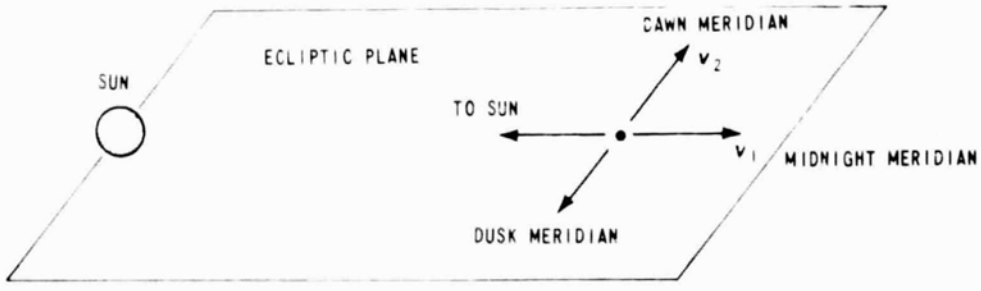

FIGURE IC1 - THE SOLAR ECLIPTIC COORDINATE SYSTEM. V_1 AND V_2 ARE IN THE DIRECTION OF RANDOM VELOCITY COMPONENTS IN THIS SYSTEM

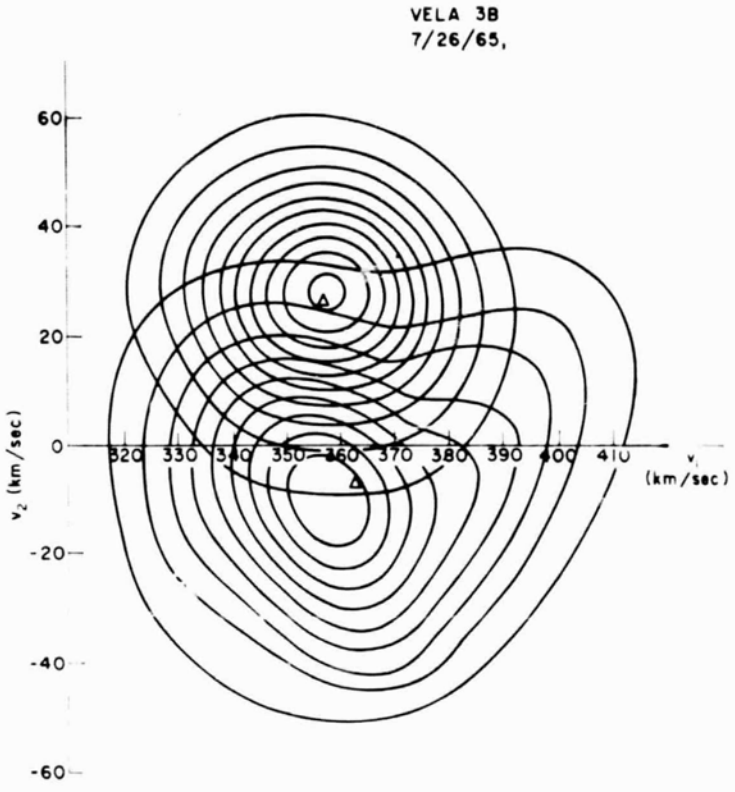

FIGURE IC2 - PROTON VELOCITY CONTOUR MAPPINGS. UPPER CONTOURS - FROM OBSERVATIONS ON VELA 3B ON 7/26/65; LOWER CONTOURS - 8/4/65. THE CONTOURS ARE PROJECTIONS ONTO THE V_1, V_2 PLANE OF CONTOUR LINES FOR $f(V_1, V_2) = 1/10, 2/10, \ldots$ TIMES f_{MAX}, WHERE $f(V_1, V_2)$ IS THE TWO-DIMENSIONAL DISTRIBUTION FUNCTION. THE SMALL TRIANGLES INDICATE MEAN VELOCITY. DEVIATION FROM CIRCULAR CONTOURS INDICATES ANISOTROPY (AFTER HUNDHAUSEN ET AL., 1967)

of the mean square random velocity, $\langle v^2 \rangle$, are used, and Maxwellian or bi-Maxwellian fits to the distribution function are possible. Because of disparate definitions, care must be exercised when comparing temperatures that appear in the literature.

In general the temperatures of the solar wind particles parallel and perpendicular to the local magnetic field are unequal, and the ratio $T_{\perp}/T_{||}$ lies in the range 1.0-2.5 for protons, and is smaller for electrons.

Figure IC3 demonstrates the variation of $T = (M/k)\langle v^2 \rangle$ as a function of orientation with respect to the magnetic field; here M is the proton mass and k is the Boltzmann constant. Electron temperature has been observed to be 1.5 to 5 times that of protons [Montgomery et al., 1968].

(d) MAGNETIC FIELDS

The solar wind behaves like a perfect conductor: interplanetary magnetic field lines may be viewed as "frozen" into it. Since the sun is rotating and the solar wind particles are moving nearly radially, the solar magnetic field lines tend to form long Archimedes' spirals as shown in Figure IC4. This is known as the garden hose effect, because the field lines are similar to the streaklines of a fluid sprayed from a rotating source. This pattern appears to co-rotate with the sun as well as show a segmented structure with oppositely directed fields separated by neutral sheets. This large scale structure appears to be relatively long lived, with these gross features preserved over many hours [Wilcox, and Ness, 1965; Hundhausen, 1967].

Near the ecliptic, the solar magnetic field is roughly contained in the plane of the ecliptic, but fields have been measured at $\pm$10-20° out of the ecliptic. Near the earth, fields of 4-7 γ are usual, with fields as high as 20-50 γ occurring during solar storms. At IAU the theoretical spiral angle is about 45°. [Ness and Wilcox, 1965].

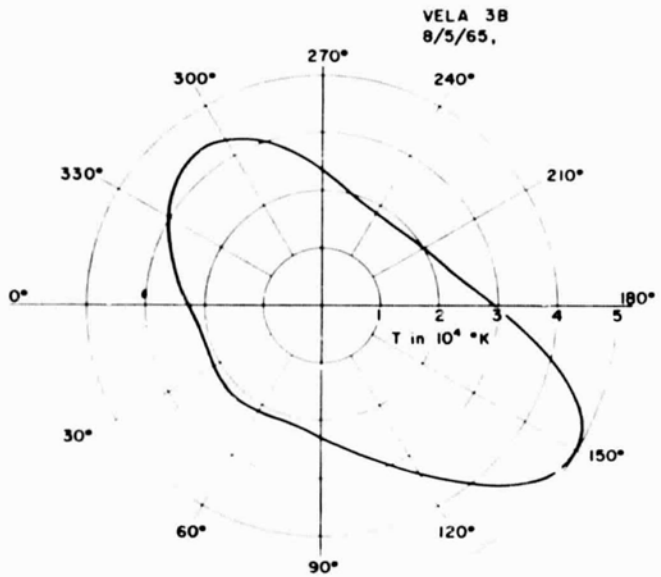

FIGURE IC3 - A POLAR PLOT OF THE TEMPERATURE, DEFINED IN TERMS OF v^2_{RANDOM} AS A FUNCTION OF DIRECTION (ϕ) IN THE V_1V_2 PLANE. THE ANGLE ϕ IS DEFINED TO BE 0 IN THE DIRECTION TION OF THE SUN (I.E., ALONG THE $-V_1$ AXIS) AND INCREASES IN A COUNTERCLOCKWISE ROTATION

(FROM HUNDHAUSEN ET AL, 1967)

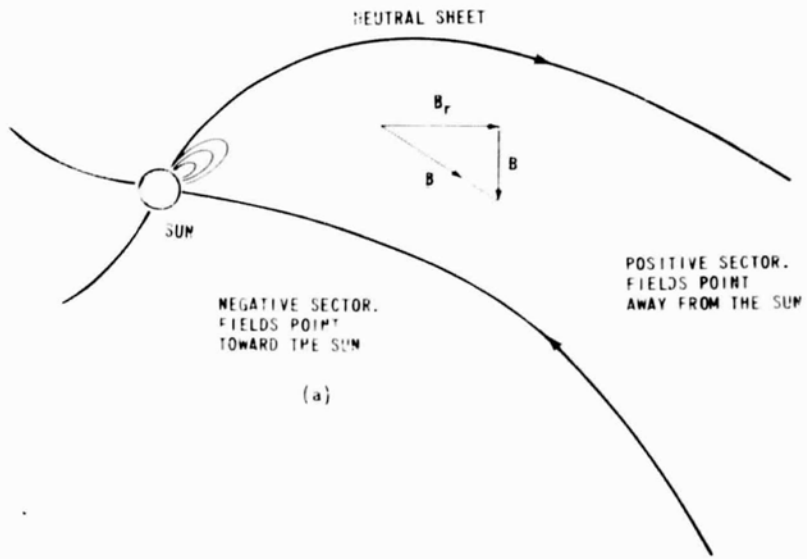

VIEWED PERPENDICULAR TO THE PLANE OF THE ECLIPTIC

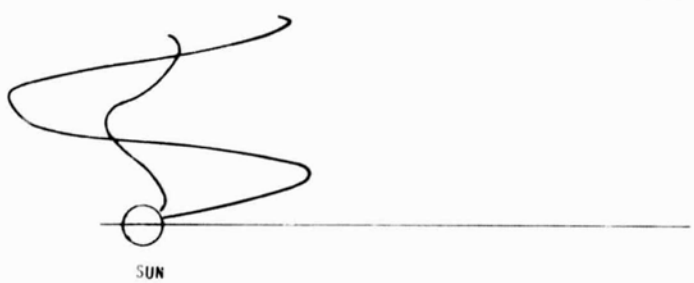

(b)

LOOKING DOWN INTO THE PLANE OF THE ECLIPTIC

FIGURE IC4 - TOPOLOGY OF THE SOLAR MAGNETIC FIELD

Ecliptic magnetic fields in the region .7 AU $\leq$ r $\leq$ 1.5 AU may be estimated using

$$B_r = B_o \left(\frac{a}{r}\right)^2$$

$$B_\theta = B_o \frac{a\Omega}{v} \frac{a}{r}$$

The components B_r and B_θ are shown in Figure IC-3

where

a = 1 AU

$B_o = 3\ \gamma = 3 \times 10^{-5}$ gauss

v = solar wind velocity

Ω = solar rotation speed.

(e) SOLAR WIND INTERACTION WITH THE GEOMAGNETIC FIELD

As the solar wind blows past the earth, the charged particles are deflected by the geomagnetic field and a hollow called the magnetosphere is formed in the plasma. Because the bulk velocity of the plasma is larger than the speed of small disturbances in it, the flow is "hypersonic" or "hyper-Alfvenic," and a detached bow shock occurs. The region between the bow shock and the magnetosphere is called the transition region. It is characterized by large temporal and spatial variations in fluid velocity, density, and the magnitude and direction of the magnetic field. It is here that the cold, highly directed solar wind is converted into a hot, turbulent plasma (see Figure IC5).

As the solar wind flows around the earth, thermal and magnetic pressures eventually overcome the earth's magnetic field pressure and the tail or wake of the magnetosphere forms. Extending far downstream, it may be detected as far as one thousand earth radii from the earth [Frank and Van Allen, 1964; King and Newman, 1967].

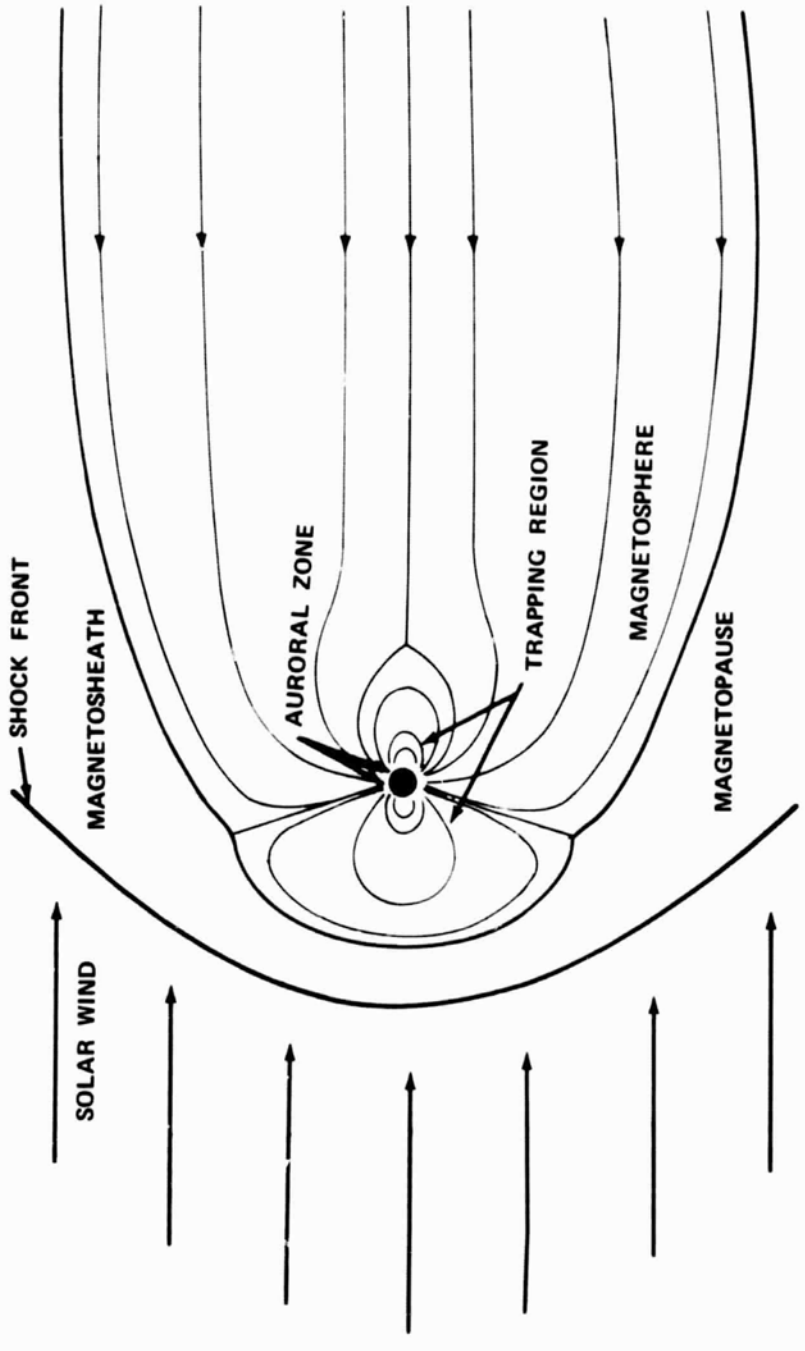

FIGURE IC5 - SCHEMATIC DIAGRAM OF INTERACTION OF SOLAR WIND WITH THE MAGNETOSPHERE

The distance from the earth to the stagnation point is obtained by assuming the dynamic pressure of the solar wind to be equal at that point to the pressure of the geomagnetic field. Since the field is compressed by the solar wind, its value at the subsolar point is frequently estimated to be twice the value of a dipole magnetic field at the same radius [Mead and Beard, 1964]. Thus

$$R_{Subsolar} = \left(\frac{M^2}{4\pi\rho v^2} \right)^{1/6}$$

where R is the geocentric distance of the subso ar stagnation point; ρ gm cm^{-3} is the mass density of the solar wind, v cm sec^{-1} is its mean velocity. $M = 8.06 \times 10^{25}$ gauss cm^3 is the earth's dipole moment.

(f) SOLAR STORMS

The occurrence of flares on the sun gives rise to large scale variations in the solar wind, known as storms. These storms are transmitted through the magnetosphere to ground level, where they can be sensed by magnetometers. These storms are also responsible in some way for the presence of auroras and of the Van Allen belt particles [King and Newman, 1967].

During storms, the magnetic field and the solar wind velocity attain values as high as 40γ and 800 km sec^{-1} respectively.

There is also evidence indicating that time variations in the solar wind cause a dynamic response of the entire interaction structure. Such variations have been seen as multiple crossings by the space vehicle of either the bow shock or the surface of the magnetosphere [Snyder et al., 1963].

(g) TERMINATION OF THE SOLAR WIND

As the solar wind expands through the solar system, the density and dynamic pressure continually decrease, and eventually, when the pressure falls to the point where it can be balanced by the pressure of the galactic magnetic field or interstellar particles, the solar wind will terminate. An interaction region of some kind is expected to exist, and it is believed that solar wind particles are able to leak through this region into intergalactic space. Estimates based on a 1-4 γ galactic field yield a termination radius of 12-160 AU. However, numerical values of the physical parameters are not known well enough to establish the termination distance to within an order of magnitude [Axford et al., 1963].

(IC) SOLAR WIND, INTERPLANETARY GAS AND MAGNETIC FIELDS - REFERENCES

Axford, W. I., A. J. Dessler, and B. Gottlieb, "Termination of the solar wind and solar magnetic fields," Astrophys. J., 137, 1268-1278, 1963.

Brandt, J. C. and P. Hodge, Solar System Astrophysics, McGraw Hill, New York, 1964.

Frank, L. A. and J. A. Van Allen, "A Survey of magnetospheric boundary phenomena," pp. 161-187, in Research in Geophysics, Vol. 1, H. Odishaw ed., M.I.T. Press, Cambridge, Mass., 1964.

Hundhausen, A. J., J. R. Asbridge, S. J. Bame, H. E. Gilbert, and I. B. Strong, "Vela3 satellite observations of solar wind ions: A preliminary report," J. Geophys. Res., 72, 87-100, 1967.

King, J. W., and W. S. Newman, eds., Solar-Terrestrial Physics, Academic Press, New York and London, 1967.

Mead, G. D. and D. B. Beard, "Shape of the geomagnetic field solar wind boundary," J. Geophys. Res., 69, 1169-1180, 1964.

Macken, R. and M. Neugebauer, eds., The Solar Wind, Pergamon Press, New York, 1966.

Montgomery, M. D., S. J. Bame, and A. J. Hundhausen, "Solar wind electrons: Vela 4 measurements," J. Geophys. Res., 73, 4999-5003, 1968.

Ness, N. F., and J. M. Wilcox, "Sector structure of the quiet interplanetary field," Science, 148, 1592-1594, 1965.

Patterson, T. N. L., F. S. Johnson, and W. B. Hanson, "The distribution of interplanetary hydrogen," Planet Space Sci., 11, 767-778, 1963.

Snyder, C. W., M. Neugebauer, and U. R. Rao, "The solar wind velocity and its correlation with cosmic ray variations and with solar and geomagnetic activity," J. Geophys. Res., 68, 6361-6370, 1963.

Wilcox, J. M. and N. F. Ness, "Quasi-stationary corotating structure in the interplanetary medium," J. Geophys. Res., 70, 5793-5805, 1965.

(ID) SOLAR COSMIC RADIATION

(a) INTRODUCTION

Interplanetary space contains energetic charged particles from two main sources; the sun and the galaxy. This section deals with the high energy particles that the sun occasionally injects into the interplanetary medium, besides its continuous emission of low energy (∿KeV) particles in the solar wind. The association of solar high energy particle [SHEP] events with solar flares, and their accompaniment by type IV radio noise bursts [Maxwell, 1965], suggests acceleration of particles in the magnetic fields of the chromosphere [Wentzel, 1964].

(b) COMPOSITION, ENERGY RANGE, FLUX AND TOTAL ENERGY

Table ID. presents the relative numerical abundance of elements in the sun, in the solar cosmic radiation, and in the galactic cosmic radiation [Aller, 1963; Biswas and Fichtel 1964; Müller, 1967; Webber, 1967].

The observed energy spectrum of energetic solar particles ranges from a few MeV to ∿1BeV, with integrated fluxes [see par. (ID)(c)] of 10^6-10^7 protons cm^{-2} sec^{-1}. The total energy associated with the corpuscular component of a large solar event may amount to $\sim 10^{32}$ erg.

(c) INTENSITY AND SPECTRA OF COSMIC RAYS

The conventional measure of the total instantaneous intensity of solar or galactic cosmic radiation is the *flux density* of particles, N(t) particles cm^{-2} sec^{-1}. This may refer to a particular element, or to a collection of elements, but includes particles of all energies. The *time integrated flux*, particles cm^{-2}, is the cumulative flux of particles, observed over the lifespan of a solar event.

Spectra of cosmic rays refer to the instantaneous or cumulative flux of particles over a specific range of energies. Thus, *differential energy spectra*, j(T),

Table ID.1

Relative abundances of nuclei normalized to a base of 1.0 for oxygen

Element	Sun	Solar Cosmic Rays	Galactic Cosmic Rays
$_1H$	120.0	111.0	300.0
$_2He$	100.0	107.0±14.0	48.0
$_3Li$	<<0.001	.....	0.3
$_4B$,$_5B$	<<0.001	<0.02	0.8
$_6C$	.06	0.59±0.07	1.8
$_7N$	0.1	0.19±0.04	≤0.8
$_8O$	1.0	1.0	1.0
$_9F$	<<0.001	<0.03	≤0.1
$_{10}Ne$	?	0.013±0.02	0.30
$_{11}Na$	0.002	.....	0.19
$_{12}Mg$	0.027	0.043±0.011	0.32
$_{13}Al$	0.002	.....	0.06
$_{14}Si$	0.035	0.033±0.011	0.12
$_{15}P$-$_{21}Sc$	0.032	0.057±0.017	0.13
$_{22}Ti$-$_{28}Ni$	0.006	≤0.02	0.28

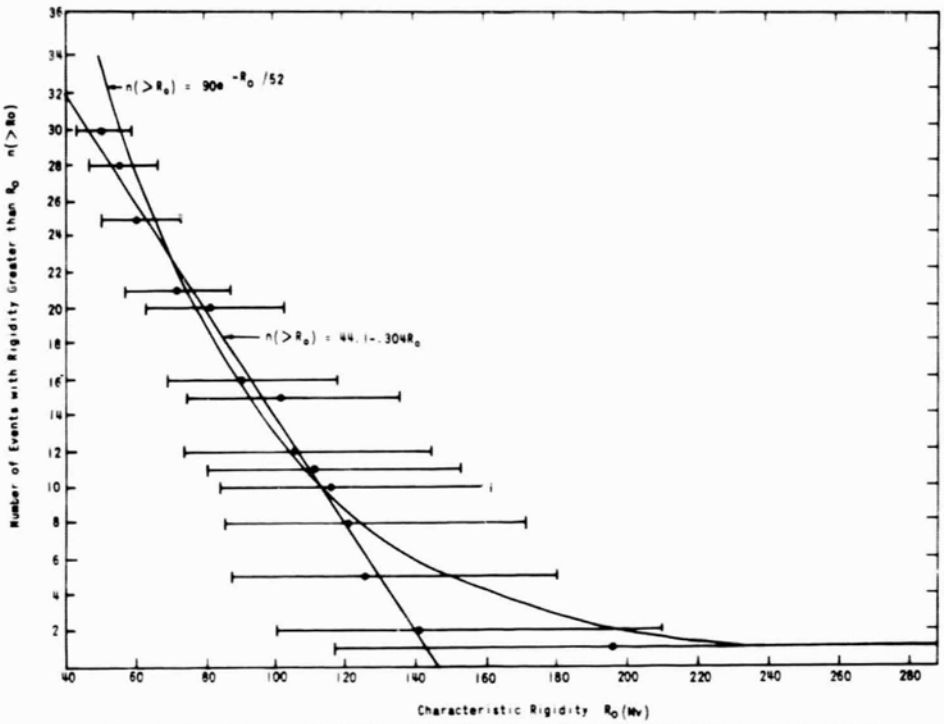

FIGURE ID1 - DISTRIBUTION OF CHARACTERISTIC RIGIDITY (FROM HILBERG, 1965)

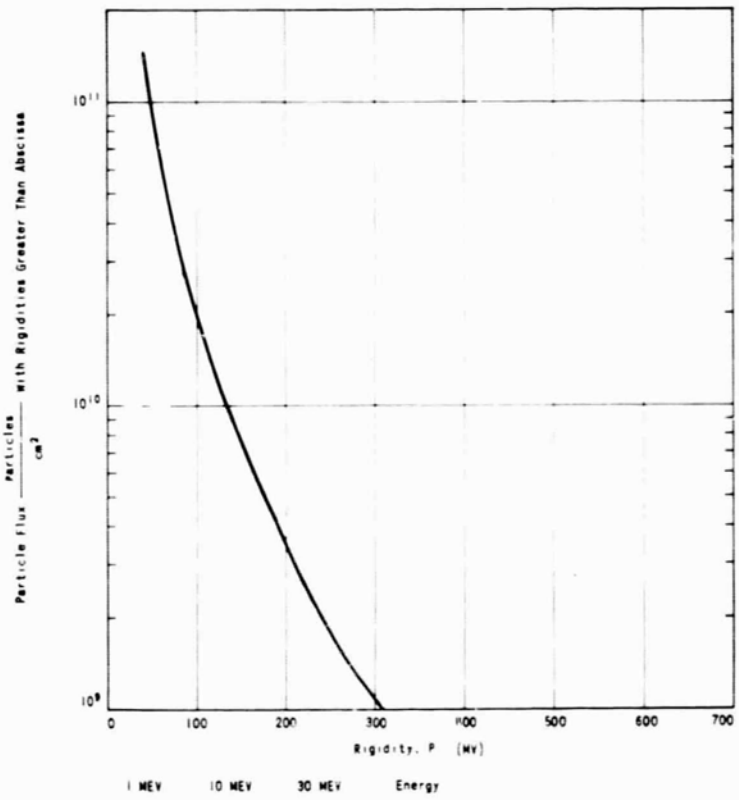

FIGURE ID2 - NEPSAP MODEL SOLAR COSMIC RAY EVENT (FROM NASA SE015-001-1, 1965)

are usually given in particles $cm^{-2}sec^{-1}MeV^{-1}$, when instantaneous values are referred to. The corresponding *differential rigidity spectra*, j(P), are in units of particles $cm^{-2}sec^{-1}$ MV^{-1}. *Integral energy or rigidity spectra*, J(>T) resp. J(>P), denote the flux of particles above a certain minimum energy or rigidity, that is

$$J(>T) \equiv \int_T^\infty j(T')dT' \quad J(>P) = \int_P^\infty j(P')dP'$$

Obviously J(>0) = N(t).

The relation between rigidity and kinetic energy is given by

$$P = \frac{1}{eZ}\left|T^2 + 2Tm_oc^2\right|^{1/2} = \frac{pc}{eZ} \text{ Million Volts}$$

Here T MeV is the kinetic energy of a particle, m_oc^2 MeV its rest energy, eZ its charge in units of the electron charge, P MV its rigidity; p MeV/c is its (relativistic) momentum.

(d) VARIATIONS WITH SOLAR DISTANCE

In the absence of experimental data, the dependence of flux density on distance from the sun, R, may be tentatively inferred from the structure of the average interplanetary field, which appears to be parallel to a plane inclined 10-20° to the ecliptic [Ness et al., 1964]. This suggests containment of solar particles near the ecliptic, which leads to a particle flux density $\propto 1/R$.

(e) TIME DEVELOPMENT OF SOLAR EVENTS

Observations of $\sim$50 major events lead to the following representation of the typical time dependence of the flux density, J(t), in a solar event

$$J(t) = \begin{cases} J_p \exp[-(t_p - t)/t_r] & t < t_p \\ J_p \exp[(t_p - t)/t_d] & t > t_p \end{cases}$$

where:

t_p = time of peak flux

t_r = rise time of flux rate

t_d = decay time of flux rate

J_p = peak flux

t_r and t_d are functions of energy; some representative values of these qualities are given in Table ID.2 [Hilberg, 1965].

Table ID.2

Rise times and decay times for representative solar cosmic ray events

Events	Size	t_r (E>30MeV) (hours)	t_r (E>100MeV) (hours)	t_d (>30MeV) (hours)	t_d (>100MeV) (hours)
2/23/56	large	3	3	30	16
7/10/59	large	30	18	40	20
7/14/59	large	16	12	18	12
7/16/59	large	12	4	30	18
11/12/60	large	10	8	18	14
11/15/60	large	8	4	16	10
8/22/58	medium	10	3	20	8
9/3/60	medium	12	6	32	26
4/28/60	small	3	2	8	5

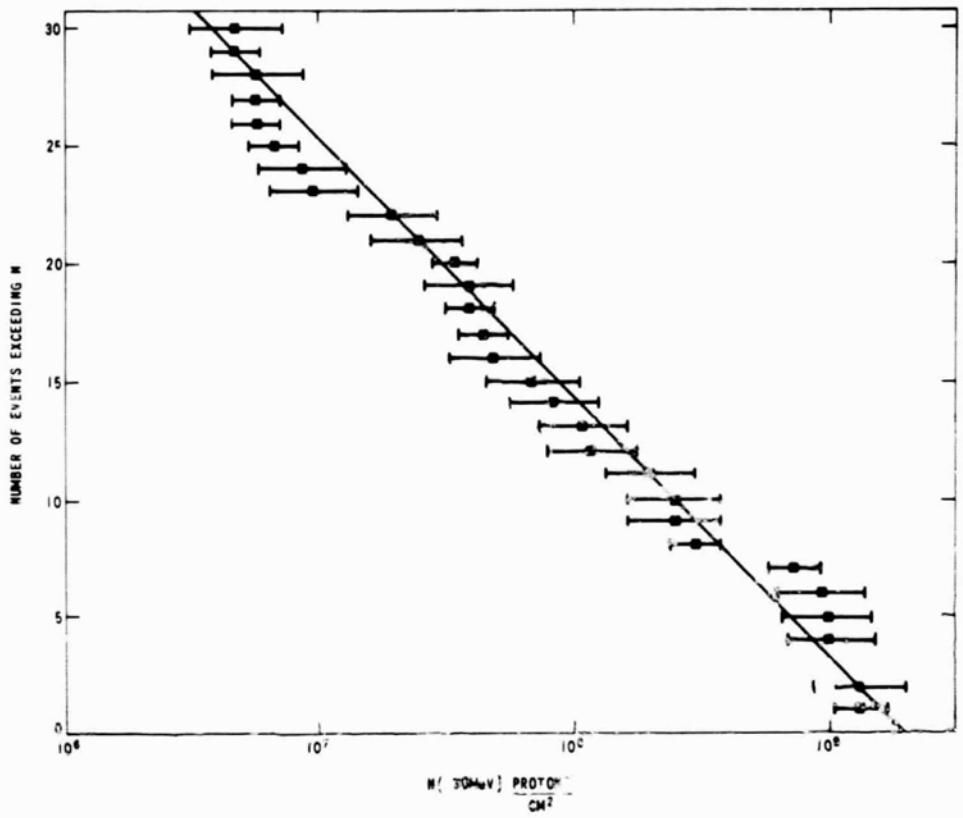

FIGURE ID3 - INTEGRAL FLUX DISTRIBUTION
(FROM HILBERG, 1965)

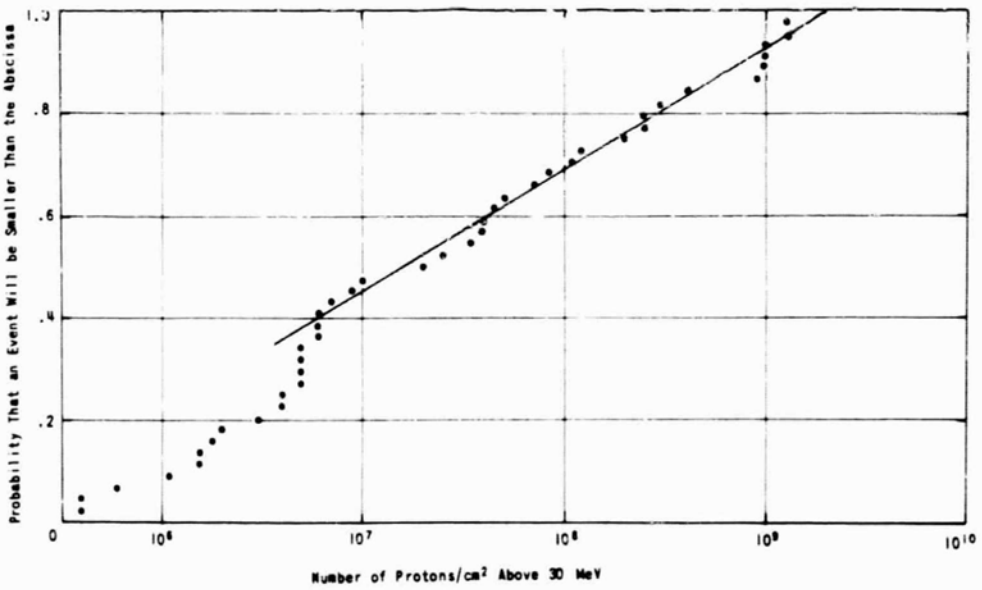

FIGURE ID4 - SIZE DISTRIBUTION OF SOLAR PARTICLE EVENTS OF THE 19TH SOLAR CYCLE IN TERMS OF LOG N (>30 MEV) VS PROBABILITY THAN AN EVENT WILL BE LESS THAN THE ABSCISSA

(FROM HILBERG, 1966)

(f) MOMENTUM SPECTRUM

The spectral shape of observed events is best described in terms of the rigidity [Freier and Webber, 1963]:

$$J(R) = J_o e^{(-R/R_o)}$$

$$N(R) = N_o e^{-(P/P_o)}$$

where J and R refer to instantaneous values of flux and rigidity, whereas N and P refer to values integrated over the duration of the event. R_o, P_o are characteristic rigidities; J_o, N_o are constants. The distribution of observed values of characteristic rigidity is presented in Figure ID1 [Hilberg, 1965]. An average time integrated spectrum for a large event is shown in Figure ID2 [NASA CE 015-001-1, 1965].

(g) STATISTICS OF SOLAR EVENTS

Figure ID3 [Hilberg, 1965] presents the observed size distribution of ∿50 major events, recorded in the maximum of the 19th solar cycle, in terms of the integrated flux of protons with energies exceeding 30 MeV. Figures ID4 and ID5, based on these results, give two possible forms for the probabilistic size distribution of events [Hilberg, 1966; Modisette, 1965]. It should be noted that the points representing the largest observed events do not fit the curves too well. This reflects the fact that ∿70% of the total energy, emitted in the form of corpuscular radiation in all recorded events, was released in only seven of these. Of these seven events, with $N_p(E>30MeV) \geq 10^9$ protons cm^{-2}, five occurred in two clusters. Clustering of large events appears to be common [Gunther, 1967], as well as the non-uniform distribution of particle emitting regions on the sun [Guss, 1964].

Apart from these reservations, the occurrence of events is considered random in time. Figure ID6 presents the probability of events of a given size occurring during missions of different durations.

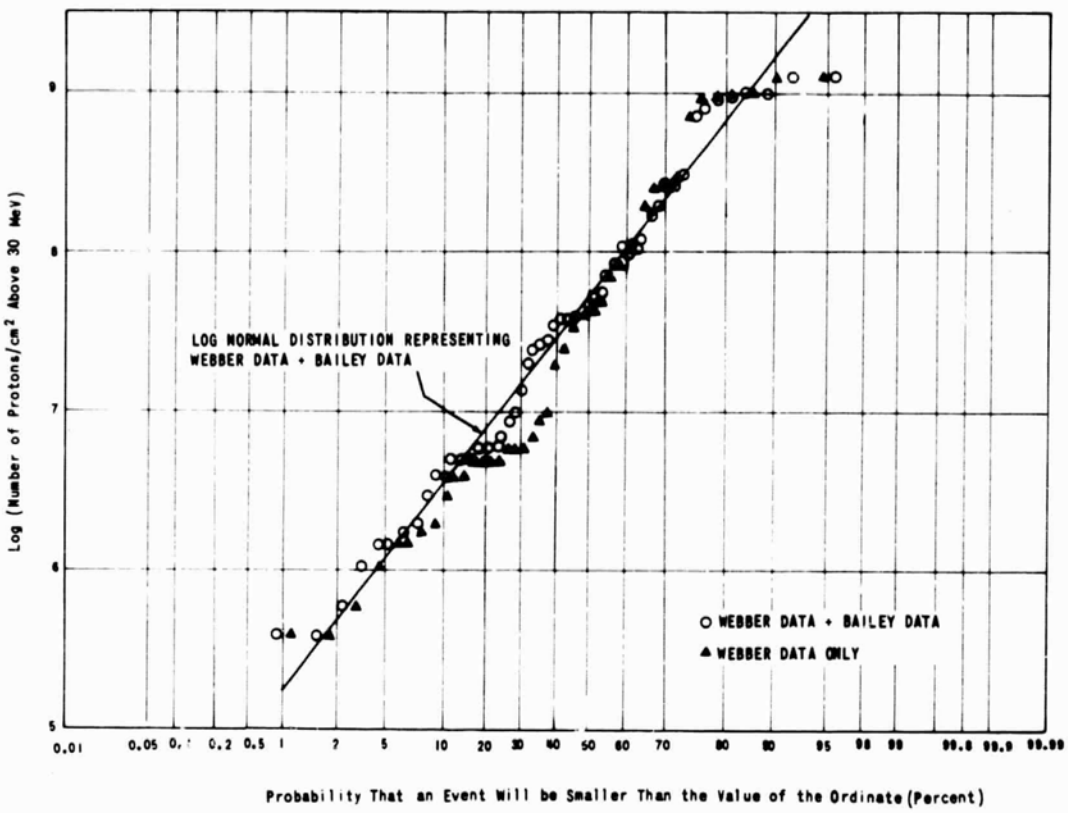

FIGURE ID5 - SIZE DISTRIBUTION OF SOLAR PARTICLE EVENTS OF 19TH SOLAR CYCLE ON NORMAL PROBABILITY PAPER
(FROM MODISETTE, 1965)

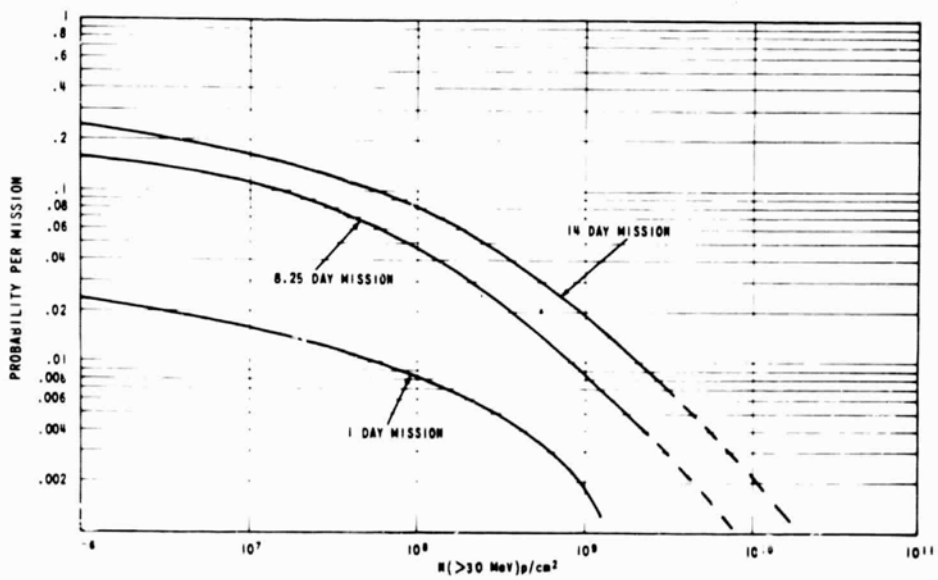

FIGURE ID6 - PROBABILITY PER MISSION OF AN OCCURRENCE OF A SOLAR COSMIC RAY EVENT HAVING AN INTENSITY GREATER THAN N PARTICLES/CM OF ENERGY GREATER THAN 30 MeV
(FROM NASA SE015-001-1, 1965)

(h) DOSAGE AND SHIELDING

Whereas mass shielding from galactic cosmic rays is relatively ineffective [see Figure IE2], this method is of use in reducing the dose from solar corpuscular radiation inside a spacecraft. Representative values of radiation doses are given in Table ID.3, reflecting their dependence on characteristic rigidity and the amount of shielding provided.

Table ID.3

Radiation dose inside a spherical aluminum shell (in units of 10^{-9} rads) per unit integrated flux of protons (E>0MeV)

Thickness (gm cm^{-2})	Characteristic rigidity (MV)			
	50	100	150	200
1	5.5	40.0	67.0	83.0
2	1.6	19.0	39.0	54.0
5	0.21	6.1	17.0	27.0
10	0.03	2.3	8.0	15.0
20	0.003	0.6	3.4	7.3

(ID) SOLAR COSMIC RADIATION - REFERENCES

Freier, P. S. and W. R. Webber, "Exponential rigidity spectrums for solar-flare cosmic rays," J. Geophys. Res., 68, 1605-1629, 1963.

Gunther, P., "Statistical characteristics of solar proton events," Bellcomm, Inc., TM-67-1033-2, 1967.

Guss, D. E., "Distribution in heliographic longitude of flares which produce energetic solar particles," Phys. Rev. Let. 13, 363-364, 1964.

Hilberg, R. H., "Solar Cosmic Ray Events," Bellcomm, Inc., TR-65-340-2, 1965.

Hilberg, R. H., private communication, 1966.

Maxwell, A., "The variable solar radio spectrum," pp. 342-397 in The Solar Spectrum, C. de Jaeger ed., D. Reidel, Dordrecht, 1965.

Modisette, J. L., T. M. Vinso and A. C. Hardy, "Model solar proton environments for manned spacecraft design," NASA TM D-2746, 1965.

Müller, E. A., "The composition of the solar atmosphere," pp. 33-67 in Solar Physics, J. Xanthakis ed., Interscience, London-New York-Sidney, 1967.

NASA-SE015-001-1, "Natural Environment and Physical Standard for the Apollo Program," April 1965.

Ness, N. W., C. L. Scearce and J. B. Seek, "Initial results of the Imp I magnetic field experiment," J. Geophys. Res., 69, 3531-3569, 1964.

Webber, W. R., "The spectrum and charge composition of the primary cosmic radiation," pp. 181-264 in Cosmic Rays II, K. Sitte ed., Vol. XLVI/2 of the Encyclopedia of Physics, Springer, Berlin-Heidelberg-New York, 1967.

Wentzel, D. G., "The origin of solar flares and the acceleration of charged particles," pp. 397-406 in AAS-NASA Symposium on the Physics of Solar Flares, W. N. Hess ed., NASA SP-50, 1964.

(IE) GALACTIC COSMIC RADIATION

(a) FLUX AND ENERGY SPECTRUM

Energetic charged particles originating outside the solar system provide a flux on the order of 2 particles cm^{-2} sec^{-1} in the vicinity of the earth, with the bulk of radiation in the range of $\sim$0.5 - $\sim$5.0 GeV kinetic energy/nucleon. The interplanetary magnetic field, which is strongly affected by solar activity, inhibits the penetration of charged particles to the inner planets, particularly in the low energy range. Figure IE1, presenting proton spectra at solar minimum and solar maximum, illustrates the modulation of galactic cosmic radiation with solar cycle, and displays the latter's marked effect on the low energy part of the spectrum [Teegarden, 1967; Fichtel, et al., 1964; Balasubrahmanyan and McDonald, 1964; Webber, 1967].

(b) COMPOSITION

The chemical composition of galactic cosmic radiation, shown in Table ID.1 (see Sec. ID) demonstrates the overwhelming preponderance of light ions, such as protons and alpha particles [see also Webber, 1967].

(c) DOSAGE AND SHIELDING

In view of the very high energies of galactic cosmic rays, mass shielding is not effective in reducing doses. Figure IE2 illustrates this for solar maximum.

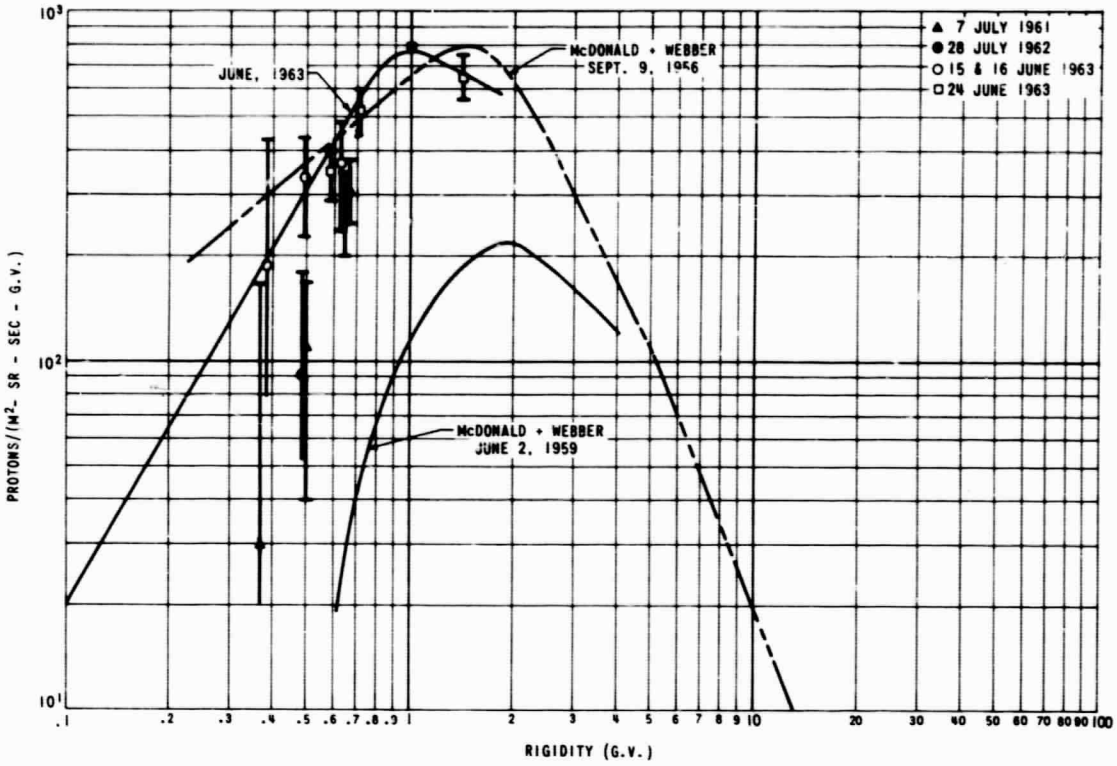

FIGURE IE1 - GALACTIC COSMIC RAY PROTON DIFFERENTIAL ENERGY SPECTRA AT SOLAR MINIMUM AND MAXIMUM

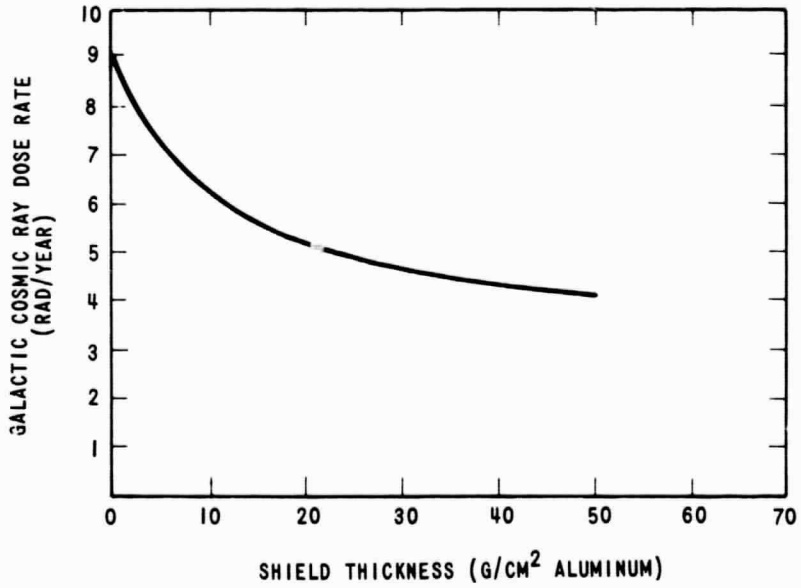

FIGURE IE2 - DOSES RESULTING FROM GALACTIC COSMIC RAYS AS A FUNCTION OF SHIELD THICKNESS

(IE) GALACTIC COSMIC RADIATION - REFERENCES

Balasubrahmanyan, V. K. and F. B. McDonald, "Solar modulation effects on primary cosmic radiation near solar maximum," J. Geophys. Res., 69, 3289-3292, 1964.

Fichtel, C. E., D. E. Guss, D. A. Kniffen, and K. A. Neelakantan, "Modulation of low-energy galactic cosmic-ray hydrogen and helium," J. Geophys. Res., 69, 3293-3295, 1964.

Teegarden, B. J., "A study of low energy galactic cosmic rays from 1961 to 1965," NASA GSFC, X-611-67-8, 1967.

Webber, W. R., "The spectrum and charge composition of the primary cosmic radiation," pp. 181-264 in Cosmic Rays II, K. Sitte ed., Vol. XLVII/2 of Encyclopedia of Physics, Springer, Berlin-Heidelberg-New York, 1967.

(IF) METEOROID ENVIRONMENT

(a) INTRODUCTION

Interplanetary space contains a large number of solid objects called meteoroids, ranging in mass from about 10^{-15}kg to many tons. They move in solar orbits and are believed to be debris given off by comets (cometary meteoroids) and by asteroids (asteroidal meteoroids). Most meteoroids of about 10^{-3}kg or smaller are believed to be of cometary origin, with a material density of about 5×10^{2}kg m^{-3}; objects having a mass greater than 10^{-3}kg contain proportionately greater amounts of asteroidal debris, having a density of about 3.5×10^{3}kg m^{-3}. There is a small mass cutoff size for particles in heliocentric orbits, inasmuch as very small particles, on the order of 10^{-15}kg or smaller, are blown away by radiation pressure [cf Robertson, 1936].

Sections (b) through (g) are a brief discussion of the distribution and some properties of meteoroids summarized in Figure IF1. Section (h) is a brief discussion of the penetration mechanics appropriate for the estimation of meteoroid impact damage to spacecraft.

(b) COMETARY METEOROIDS

These meteoroids are believed to be of cometary origin and their distribution as a function of mass and distance from the sun can be approximated by the formula

$$n(M,R) = AM^{-\alpha} R^{-\beta} \qquad \text{(IF/1)}$$

where $n(M,R)$ is the cumulative number of meteoroids per cubic meter of space having a mass of M kg or greater at a distance of R AU from the sun. A, α and β are constants, defined below in Equations (IF/2), (IF/3) and (IF/4).

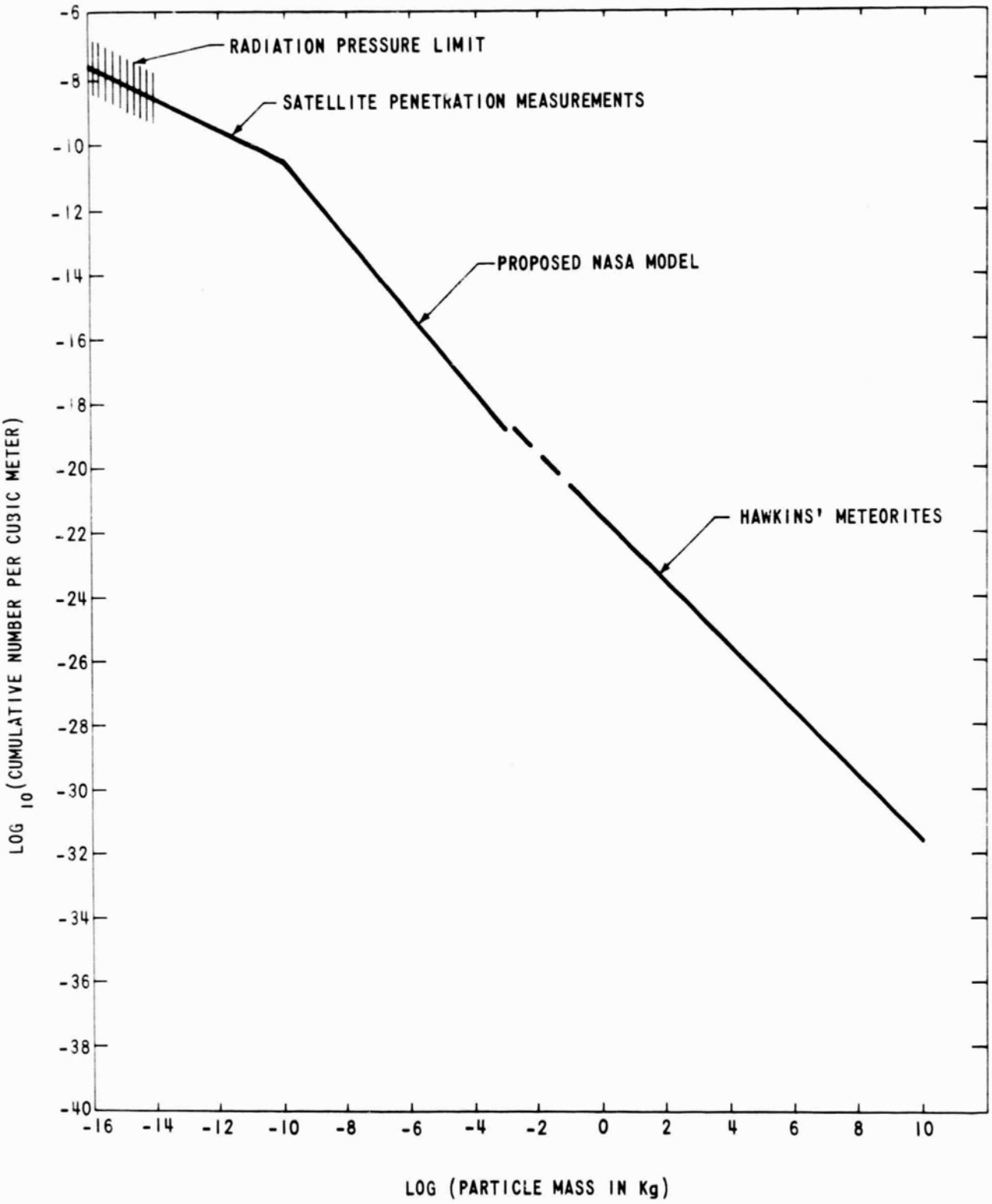

FIGURE IF1 - MASS DISTRIBUTION OF METEOROIDS. CUMULATIVE NUMBER OF PARTICLES PER CUBIC METER OF SPACE HAVING A MASS mKg OR GREATER AT A DISTANCE FROM THE SUN OF 1 AU

The following is a good approximation of existing information:

$$n(M,R) = 8.4\times10^{-22}M^{-1}R^{-\beta}\text{meter}^{-3},\ M>5\times10^{-12}\text{kg} \quad \text{(IF/2)}$$

$$n(M,R) = 6.2\times10^{-16}M^{-.48}R^{-\beta}\text{meter}^{-3},\ M<5\times10^{-12}\text{kg} \quad \text{(IF/3)}$$

Equation (IF/2) is based on the NASA model environment [NASA, SE 015-001-1, 1965]. Equation (IF/3) is based on recent results from satellite penetration measurements [Jennison et al., 1967]. A correction of 30% has been applied to the data [Dohnanyi, 1966] to compensate for the earth's gravitational focusing near earth.

An average earth entry velocity of 20 km sec^{-1} and a material density of 500 kg meter^{-3} have been assumed here as representative of meteoroids intersecting the earth's orbit, that is at R = 1 AU. Penetration criteria employed [Cour-Palais, in preparation] are similar to earlier work by Summers [1959].

The quantity β in Eqs. IF/1, 2 and 3 is uncertain. It may be taken as

$$\beta = 1.5 \quad \text{(IF/4)}$$

with an uncertainty of about $x2^{\pm1}$. While $\beta = 0$ has been employed by Elsasser [1955], a value for β higher than 1.5 may be reasonable for very small particles ($M\leq10^{-10}$kg), and a value of 1.5 or lower may be reasonable for larger particles [Southworth, 1967].

The uncertainty in n(M,R=1) because of uncertainties in A and α (Eq. IF/1) is of the order of x3; the uncertainty in β (Eq. IF/4) is therefore not very serious when R is of the order of 1 AU.

(c) ASTEROIDAL METEOROIDS

These meteoroids originate in the asteroidal belt, at a distance of 2.2 AU to 3.5 AU from the sun. The contribution of these objects to the environment near

1 AU from the sun is negligible [Jacchia, Verniani and Briggs, 1965] but their distribution in the asteroidal belt has been estimated [Dohnanyi, in preparation; cf also Dohnanyi, 1967]. The result is, in the same notation as Equations (IF/2) and (IF/3)

$$n(M) = 3.6\times10^{-19} \times M^{-.84} \text{ meter}^{-3}, 2.2<R<3.5 \quad \text{(IF/5)}$$

$$n(M) = \text{negligible, outside } 2.2<R<3.5 \quad .$$

A material density of 3.5×10^{3} kg meter^{-3}, corresponding to stony meteorites, has been assumed.

Comparison of Eq. (IF/5) with Eqs. (IF/2) and (IF/3) reveals that, for masses greater than about 10^{-11} kg, the asteroidal particles are more abundant than are cometary ones in the asteroidal belt.

Asteroidal particles have an average velocity, relative to each other, of about 5 ± 5 km sec^{-1} and move in direct orbits at low inclinations and small eccentricities. Their orbital velocities, relative to the sun, are about 18 km/sec.

(d) METEORITES

Meteorites are sufficiently large objects to survive entry through the earth's atmosphere. Hawkins [1963] estimated their influx rate into earth's atmosphere

$$F(M) = 5.9\times10^{-18} M^{-1} \text{ meter}^{-2} \text{ sec}^{-1}, M>.1\text{kg} \quad \text{(IF/6)}$$

where F is the cumulative influx (into earth's atmosphere) per meter^2 per sec of objects having a mass of M kg or greater.

Very little is known about the velocity distribution of meteorites. If we assume that the average meteorite has a geocentric velocity similar to that of photographic meteoroids (17 km/sec), Eq. (IF/6) yields the following mass distributions per cubic meter*

*A factor of .7 [Dohnanyi, 1966] has also been applied to correct for the earth's gravitational focusing effect.

$$n(M) = 2.43 \times 10^{-22} \; M^{-1} \; \text{meter}^{-3} \quad M > .1 \text{kg} \qquad \text{(IF/7)}$$

where the symbols are the same as in Eq. (IF/1).

(e) METEOR SHOWERS

Concentrations of cometary meteoroids into small volumes of space moving into similar orbits are encountered by the earth from time to time. When this happens, the resulting increase in the flux of meteors is called a shower. A survey of the increase in number of meteors during the various showers has been prepared by Burbank et al., [1965] to which the reader is referred for details; Lovell [1954] is a good reference for "shower" orbits and other properties.

(f) CALCULATION OF PARTICLE FLUXES

Detailed calculation of particle fluxes encountered by a spacecraft can be obtained from the defining relation

$$F(M,R) = \int_0^\infty n(M,v,R) \, v \, dv$$

where $F(M,R)\,\text{meter}^{-2}\,\text{sec}^{-1}$ is the cumulative flux of particles per square meter per second, having a mass of M kg, or greater, encountered by a spacecraft at a distance R from the sun. $n(M,v,R)dv$ is the cumulative number of particles having a mass of M kg or greater and having a velocity in the range v to v+dv meter sec^{-1} relative to the spacecraft at a distance R from the sun.

Since $n(M,v,R)\,dv$ is not generally known (for the velocity distribution of photographic meteors, cf Dohnanyi, 1966), the following approximation is suggested:

$$F(M,R) = n(m,R)\bar{V} \qquad \text{(IF/9)}$$

where n(M,R) is defined in Eq. (IF/1) and $\bar{V}$ is the mean encounter velocity in meters/sec. For asteroidal objects, $\bar{V}$ is the difference between the circular orbital velocity of an asteroidal object and the vector velocity of the spacecraft. For cometary meteoroids a mean encounter velocity $\bar{V}$ of 20 km sec^{-1} may be assumed; this results in somewhat overestimating the flux at R>1.

(g) METEOROID FLUXES AT PLANETARY SURFACES

Because of a protective atmosphere, only large objects and extremely small ones can survive and touch the planetary surface. Large objects, of the order of kilograms and greater, make a "fiery" entry through the atmosphere and loose a substantial portion of their initial mass because of ablation.

Because of their high surface-area-to-volume ratio, very small objects, of the order of 10^{-10}kg or smaller, radiate away the heat imparted by air friction fast enough to prevent complete ablation. These particles are rapidly slowed down by air friction and reach terminal velocities. Mercury is the only known planet without sufficient atmosphere to prevent objects of the size of a kg or smaller from reaching the surface with meteoric velocities.

(h) PENETRATION MECHANICS

Impact of a target by a projectile moving near the speed of sound, about km sec^{-1}, in the target material, or much faster, is called *high velocity impact* or *hypervelocity impact*, respectively. In considering the penetration of a projectile, three types of target structures are of interest.

In a *semi-infinite target* impacted by a sufficiently energetic projectile, a crater is formed at the impact site by melting and vaporization of the target material. On the basis of limited experimentation with spherical projectiles moving at speeds up to 7 km/sec a quantitative relation between the size of the resulting roughly hemispherical crater and the

projectile parameters has been proposed [Summers, 1959]. In the AMES penetration formula the depth of penetration, p, is expressed in terms of the density of target material, ρ_t, the speed of sound in the target, c, and the projectile's density ρ_p, its diameter d, and its velocity v. Thus

$$p/d = 2.28(\rho_p/\rho_t)^{2/3} (v/c)^{2/3} \quad . \qquad \text{(IF/10)}$$

Another useful form of this relation is given by

$$p = 3.56(\rho_p/\rho_t)^{1/3} (1/2\ Mv^2/E_t)^{1/3} \qquad \text{(IF/11)}$$

where M is the projectile's mass, and E_t the target material's modulus of elasticity.

For a *thin sheet target*, the thickness barely stopping a given projectile has to be considered. Experiments indicate that this required thickness, T, is proportional to the penetration depth into a semi-infinite target of the same material, with the constant of proportionality depending on the material. Thus for Aluminum, with a constant of proportionality of 1.8 [Bruce, 1965],

$$T = 6.41(\rho_p/\rho_t)^{1/3} (1/2\ Mv^2/E_t)^{1/3} \qquad \text{(IF/12)}$$

Multiple sheet construction provides the most effective protection from hypervelocity projectiles. In a bumper configuration, or double sheet structure, the first sheet serves to break the impact whereas the back-up sheet catches the debris. Only special cases of the problem of impact on a double sheet structure have been solved [Maiden et al., 1965; Christman et al., 1963; also Proceedings of Hypervelocity Impact Symposia 1961, 1963, 1965] gives the protective thickness of the back-up sheet t_b cm, required against a projectile with a diameter d cm as

$$t_b = .624\ d^{1.056}$$

This relation is valid for aluminum structures only, subject to the conditions

$$V>10 \text{ km/sec} \quad , \quad t_s/d>.1 \qquad \text{(IF/13)}$$

where v is the projectile velocity, t_s is the thickness of the outer (bumper) sheet, and where the spacing between the bumper sheet and back-up sheet is 5.08 cm (i.e., 2 inches). Eq. (IF/12) is adequate for greater double sheet separations, but should be scaled inversely with the square of the separation distance for smaller separations.

(IF) METEOROID ENVIRONMENT - REFERENCES

Bruce, G. P., in Proceedings, Fifth Symposium on Hypervelocity Impact, Tampa, Fla., 1965, US Army/US Navy/ USAF. Washington, D. C., 1965.

Burbank, P. B., B. G. Cour-Palais and W. E. McAllum, "A meteoroid environment for near-earth cislunar and near-lunar operations," NASA TN D-2747.

Christman, D. R., J. W. Gehring, C. J. Maiden and A. B. Wenzel, "Study of the pheonomena of hypervelocity impact," G. M. Defense Research Laboratories, TR 63-216, 1963.

Dohnanyi, J. S., "Collisional model of asteroids and their debris," IAU Symposium on the Physics and Dynamics of Meteors, Tatranska Lomnica, Czechoslovakia, 1967.

Elsasser, H. Z., "Fraunhoferkorona and Zodiakallicht," Z. f. Astrophys., 37, 114-124, 1955.

Hawkins, G. S., "Impacts on the earth and moon," Nature, 197, 781, 1963.

Jacchia, L. G., F. Verniani and R. E. Briggs, "An analysis of the atmospheric trajectories of 413 precisely reduced photographic meteors," Smithsonian Astron. Obs. Spec. Report #175, 1965.

Jennison, R. C., J. A. M. McDonnel, and I. Rodgers, "The Ariel II micrometeorite penetration measurements," Proc. Roy. Soc., 300, 251-269.

Kuiper, G. P., Y. Fujita, T. Gehrels, I. Groeneweld, J. Kent, G. Van Biesbroeck and C. J. Van Houten, "Survey of asteroids," Astrophys. J. Suppl., Ser. 3, 289-427, 1958.

Lovell, A. C. B., Meteor Astronomy, Oxford Univ. Press, 1954.

Maiden, C. J., A. R. McMillan, R. E. Sennet and J. W. Gehring, "Experimental investigations of simulated meteoroid damage to various spacecraft structures," G. M. Defense Research Laboratories, TR 65-48, 1965.

NASA, SE 015-001-1, "Natural environment and physical standards for the Apollo program," April, 1965.

Proceedings Fifth Symposium on Hypervelocity Impact, Denver, Colorado, 1961, US Army/US Navy/USAF, Washington, D. C., 1961.

Proceedings Sixth Symposium on Hypervelocity Impact, Cleveland, Ohio, 1963, US Army/US Navy/USAF, Washington, D. C., 1965.

Proceedings Seventh Symposium on Hypervelocity Impact, Tampa, Florida, 1965, US Army/US Navy/USAF, Washington, D. C., 1965.

Robertson, H. P., "Dynamical effects of radiation in the solar system," Monthly Not. Roy. Astron. Soc., 97, 423-438, 1936.

Southworth, R. B., "Space density of radio meteors," Smithson. Astron. Obs., Spec. Rep. #239, 1967.

Summers, J. L., "Investigation of high-speed impact regions of impact and impact at oblique angles," NASA TN D-94, 1959.

(II) MARS

(IIA) GENERAL PHYSICAL PROPERTIES OF MARS

(a) INTRODUCTION

Mars moves in an elliptic orbit with an eccentricity of ~ 0.09 and a period of ~ 1.881 earth years. Because of this eccentricity the synodic period of Mars varies from its mean of ~ 780 days by as much as 20 days; its closest distance from earth varies over the synodic recursion cycle of $\sim$ 15-17 years by ~ 0.3 AU from ~ 0.38 AU at perihelic opposition to ~ 0.68 AU at aphelic opposition. Relevant physical parameters of Mars are given in Table IIA.1 [Michaux, 1967; NASA SE 015-001-1, 1965; Melbourne et al., 1968]. Precise data on state vectors of Mars and of the other planets are contained in JPL Development Ephemeris Tape Number 19 [Devine, 1967].

Table IIA.1

Physical parameters of Mars

Ratio of Mars' mass to earth's mass	0.1074469
Gravitational parameter	$4.282844 \times 10^{19} cm^3 sec^{-2}$
Equatorial diameter	$[6.7868 \pm 0.008] \times 10^8 cm$
Rotation period (sidereal)	$8.86427 \times 10^4 sec$ =24 hrs. 37 min. 22.7 sec.
Mean distance from the sun	1.5236915 AU $=2.2794104 \times 10^{13} cm$
Eccentricity (1970)	0.093377
Mean orbital velocity	24.13 km sec^{-1}
Inclination of orbit to ecliptic(1970)	1°50' 59.5"

(b) GEOMETRIC AND PHOTOMETRIC RELATIONSHIPS RELATED TO PLANETARY OBSERVATIONS

The basic geometrical relationships governing remote observations of a planet as a whole are illustrated in Figure IIA1. The planet-observer direction and the planet-sun direction lie in and define the plane of vision; the angle between these two directions is defined as the phase angle. In the following earth will be substituted for observer, without loss of generality.

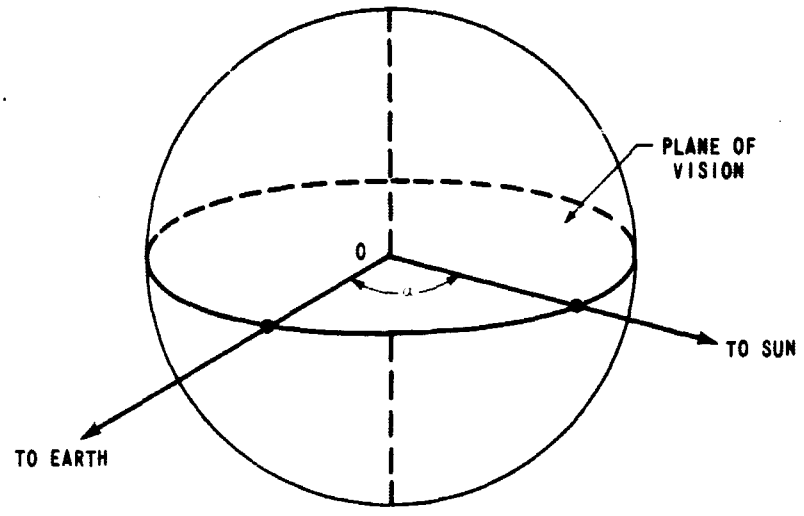

FIGURE IIA1 - GEOMETRICAL RELATIONSHIP FOR THE PHOTOMETRIC AND POLARIMETRIC DESCRIPTION. α, THE PHASE ANGLE LIES IN THE PLANE OF VISION

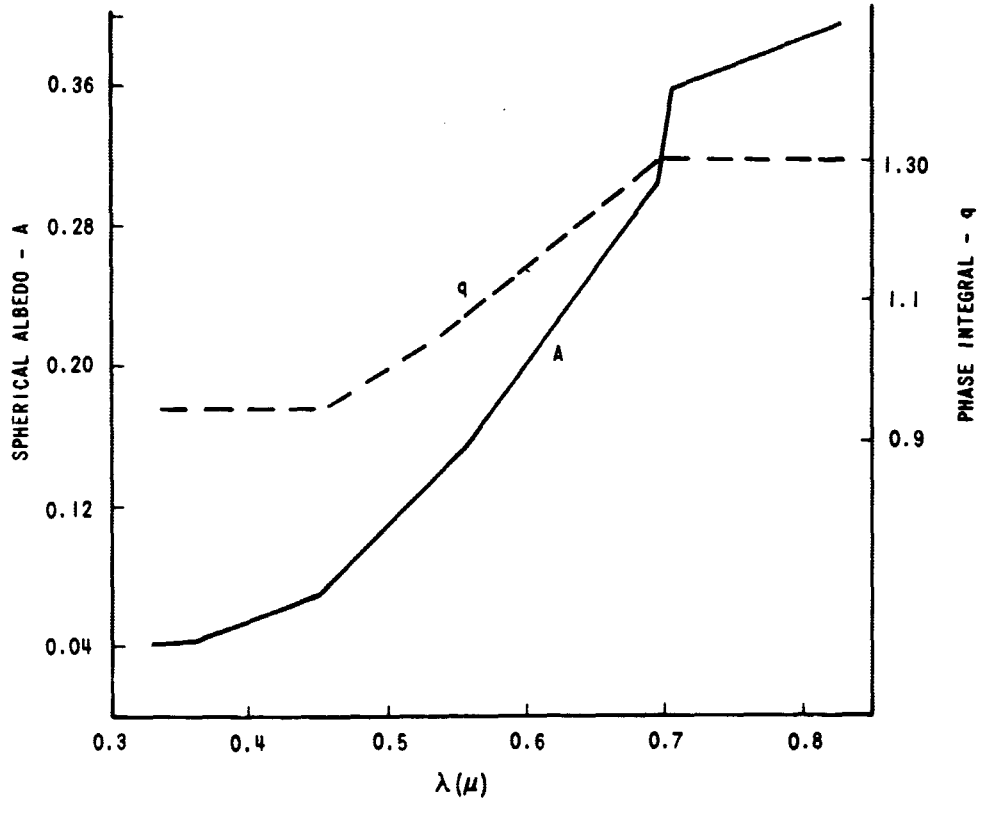

FIGURE IIA2 - SPECTRAL VARIATION OF PHASE INTEGRAL q AND SPHERICAL ALBEDO A (AFTER DE VAUCOULEURS)

Consider a limited region of the solar spectrum where parameters depending on wavelengths can be considered approximately constant. The illumination within this range, E lumen m^{-2}, or alternatively the irradiance, I watt cm^{-2}, at earth due to solar radiation reflected from the planet, is a function of the phase angle α, the planet-sun distance R, and the planet-earth distance Δ. E is inversely proportional to R^2 and Δ^2. It is convenient to reduce E (α, R, Δ), measured at arbitrary R and Δ, to a value E (α, R_o, Δ_o) for the illumination at fixed distances Ro and Δo:

$$E(\alpha, R_o, \Delta_o) = E(\alpha, R, \Delta) \frac{R^2\Delta^2}{R_o^2\Delta_o^2} \qquad \text{(IIA-1)}$$

Conventionally 1 AU is chosen for both Ro and Δo.

The phase function of the planet, $\phi(\alpha)$, describes the phase angle dependence of the illumination and is defined:

$$\phi(\alpha) = \frac{E(\alpha, R_o, \Delta_o)}{E(o, R_o, \Delta_o)} \qquad \text{(IIA-2)}$$

Let r be the planetary radius, and E_s the solar illumination at a distance Ro. Then the solar luminous flux incident on the planet, at distance R from the sun, is

$$\pi r^2 \frac{R_o^2}{R^2} E_s$$

The total flux reflected by the planet in all directions is equal to the flux intercepted by a spherical surface at a distance Δ_o from the planet, and amounts to

$$2\pi\Delta_o^2 \frac{R_o^2}{R^2} \int_o^\pi E(R_o, \Delta_o, \alpha) \sin\alpha \, d\alpha$$

The geometrical albedo, p, is defined as

$$p \equiv \frac{2E(O,R_o,\Delta_o)\Delta_o^2}{E_s r^2} \qquad \text{(IIA-3)}$$

and the phase integral, q, is defined as

$$q \equiv 2 \int_0^{\pi} \phi(\alpha) \sin\alpha \, d\alpha \qquad \text{(IIA-4)}$$

Then the spherical or Bond albedo, A, defined as the ratio of total reflected to total incident luminous flux, within the range of wavelengths considered, is given by

$$A = \frac{2E(0,R_o,\Delta_o)}{E_s r^2} \int_0^{\pi} \phi(\alpha) d\alpha \qquad \text{(IIA-5)}$$

$$\equiv pq$$

In general p, q, and A vary with wavelength. The ratio of the total amount of solar radiation, reflected over the whole spectrum, to the total incident radiation is given by the radiometric albedo, A*. Let $E_s(\lambda)$, $p(\lambda)$, and $q(\lambda)$ be the spectral variations of the solar radiation, the geometric albedo and the phase integral. Define

$$p^* \equiv \int_0^{\infty} p(\lambda) E_s(\lambda) d\lambda \Big/ \int_0^{\infty} E_s(\lambda) d\lambda$$

$$q^* \equiv \int_0^{\infty} q(\lambda) E_s(\lambda) d\lambda \Big/ \int E_s(\lambda) d\lambda$$

Then the radiometric albedo is given by

$$A^* = p^* q^* \qquad \text{(IIA-6)}$$

A Lambert surface is a perfect reflector of light at all wavelengths, so that by definition, $A \equiv A_o = 1$. The amount reflected in a particular direction is proportional to the projected area in that direction. If planetary surfaces were considered Lambert spheres

$$p(\lambda) = p_o^* = 2/3 \qquad q(\lambda) = q_o^* = 3/2$$

No real planets show this behavior.

(c) PHOTOMETRIC PROPERTIES OF MARS

The photometric parameters, as defined in Section (IIA) (b), referring to the integrated light from the entire visible hemisphere of Mars, are given in Table IIA.2 [de Vaucouleurs, 1964]. p, q, A, in this table refer to light integrated over all visible wavelengths; the wavelength dependence of p and q is shown in Figure IIA2. The values of the radiometric parameters, p*, q*, and A*, depend on extrapolation of the spectral response in both the infrared and ultraviolet, and have, therefore, large uncertainties.

Table IIA.2

Photometric Properties of Mars

p	0.149 ± 0.005
q	1.07 ± 0.05
A	0.159 ± 0.008
p*	0.235
q*	1.24
A*	0.295

The phase function of Mars, $\phi(\alpha)$, is shown in Figure IIA3.

The quantities presented so far are averages, and thus do not indicate any brightness structure of the planet. Actually Mars displays a distribution of bright and dark features that is not uniform in longitude or in latitude over the planet's surface, and seasonal variations also affect the planet's brightness. The longitudinal effect, which arises from the varying proportion of bright areas in the visible hemisphere due to the rotation of Mars, changes the apparent brightness of the entire visible disk by as much as $\pm 10\%$.

Extensive observations of the relative brightness of various Martian features, have yielded contour maps of relative brightness [de Vaucouleurs, 1967]. Such a map is reproduced in Figure IIA4. These maps are based on observations, conducted over an extended period of time, and therefore carried out with varying geometry of each observed feature. No corrections for geometric and seasonal effects were applied; the data represent, consequently, averages over various parameters. The data in Figure IIA4 should be construed as representing normal viewing at zero phase angle, since the underlying observations are centered on that geometry.

Conversion of relative brightness to absolute brightness (candles cm^{-2}) depending on the distance between Mars and the sun,

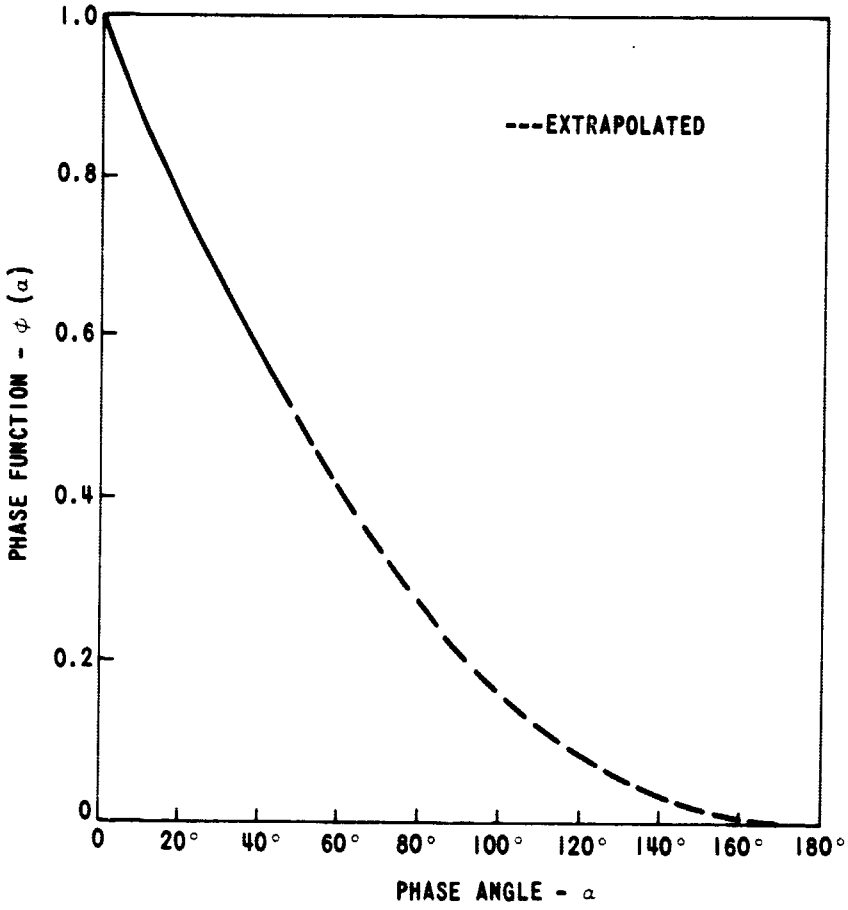

FIGURE IIA3 - VISUAL PHASE FUNCTION OF MARS

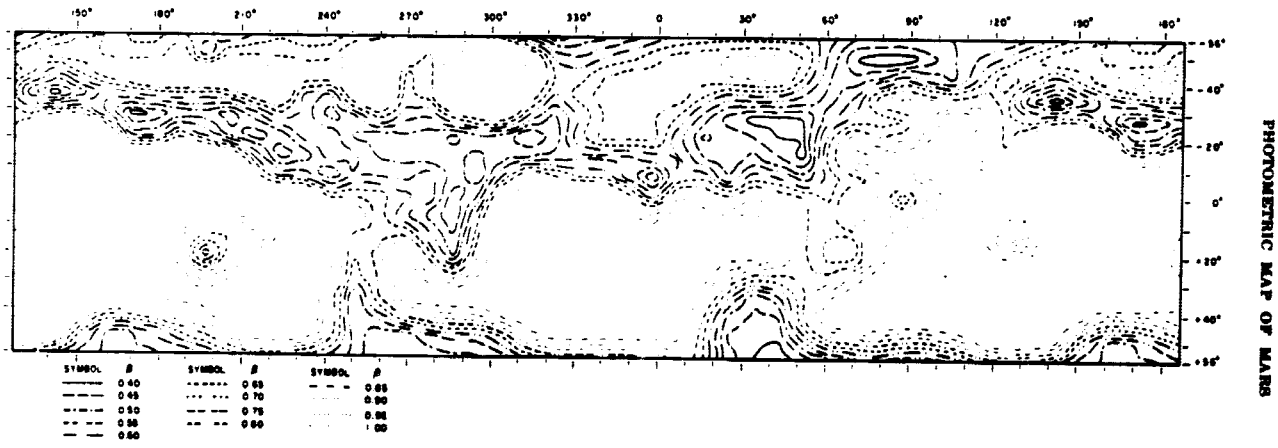

FIGURE IIA4 - CONTOUR MAP OF EQUAL RELATIVE BRIGHTNESS β FOR THE PLANET MARS. THE MAP WAS MADE AT A RESOLUTION OF ABOUT 600 KM (APPROX. 10°)

is provided in Table IIA.3 for specific distances, and unit relative brightness.

Table IIA.3

Conversion of relative brightness on Mars to absolute brightness

Distance	Absolute Brightness (candles cm^{-2})
Aphelion	0.20
Mean	0.235
Perihelion	0.28

Figure IIA.4 does not include the polar caps because of their drastic seasonal variations. The maximum observed brightness of the polar cap area has a relative value of 1.8.

(d) POLARIMETRY

The degree of polarization, P, of the radiation reflect- by a region of the planet, including its atmosphere, is defined as

$$P = \frac{I_{\perp} - I_{||}}{I_{\perp} + I_{||}}$$

Here $I_{\perp}$ and $I_{||}$ are the intensities of observed radiation polarized perpendicularly and parallel to the plane of vision [see Section IIA(b)]. Theoretically $-1 \leq P \leq 1$, but in practice P for the planets varies typically from fractions of a percent to a few percent. The variation of the observed polarization is primarily a function of wavelength and phase angle, and depends slightly on the brightness of the region, and on the season of the Martian year [Dollfus, 1964]. Figure IIA5 shows a typical polarization curve of a light area on Mars, plotted for the accessible phase angles [ibid.].

All natural materials display a characteristic polarization. To use knowledge of the latter and its variations as a potential source of information on the nature of the Martian environment, attempts have been made to separate the contributions to total observed polarization of the atmosphere of Mars and its surface [Dollfus, 1964].

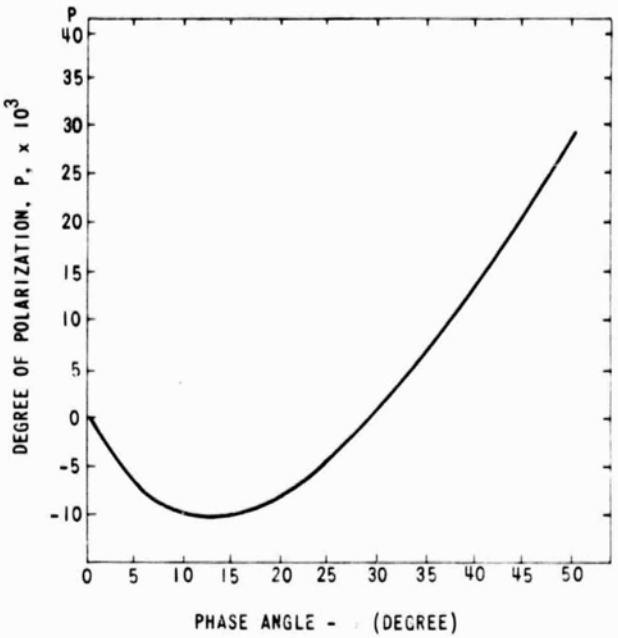

FIGURE IIA5 - AVERAGE POLARIZATION CURVE OF LIGHT REGIONS ON MARS (AFTER DOLLFUS, 1964)

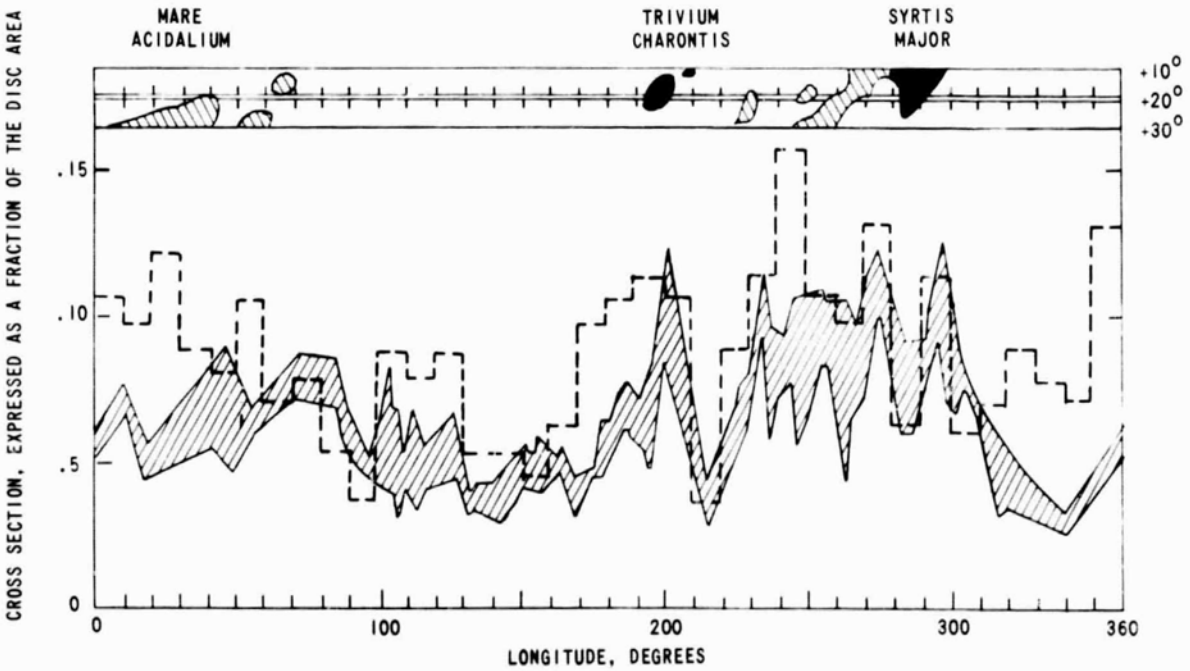

FIGURE IIA6 - VARIATION OF THE RADAR CROSS SECTION OF MARS AT 70 CM (SHADED REGION) AND AT 12.5 CM WAVELENGTH (DOTTED LINE), DURING THE 1965 OPPOSITION, AS A FUNCTION OF THE CENTRAL MERIDIAN OF THE VISIBLE DISC. THE STRIP MAP AT THE TOP OF THE FIGURE SHOWS THE PRINCIPAL OPTICAL FEATURES OF MARS NEAR THE SUB-RADAR LATITUDE OF 20°N (AFTER PETTENGILL AND EVANS, 1967)

(e) RADAR REFLECTIVITY AND SCATTERING BY MARS

The radar back-scatter cross-section, σ, is given by

$$\sigma = \pi r^2 g \rho$$

where r is the planetary radius; ρ, the average reflection coefficient, is the ratio of total scattered power to total incident power; g, the directivity, depends on the surface geometry. For a smooth, perfectly reflecting sphere, g=1; g is close to 1 for a sphere with a gently undulating surface [Hagfors, 1964]; for a Lambert surface g = 8/3.

Measurement of the c.w. received echo power, P_r, and knowledge of the transmitted power, P_t, the antenna gain, G, the distance of the planet from earth, d, and the wavelength, λ, determine σ, by means of the relation

$$\sigma = \frac{(4\pi)^3 \, d^4}{G^2 \lambda^2} \frac{P_r}{P_t}$$

From the measured value of σ, ζ is obtained, using $g \sim 1$, as appropriate for Mars.

For a material of low electrical conductivity, and with the magnetic susceptibility of free space, the dielectric constant, ε, is related to the reflectivity at normal incidence, ζ_1, by means of

$$\varepsilon = \left(\frac{1+\rho_1^{1/2}}{1-\rho_1^{1/2}} \right)$$

To a good approximation $\rho_1 = \rho$.

Mean values of the cross section, measured at various wavelengths and expressed as a fraction of the area of the disc, $\sigma/\pi r^2$ are quoted in Table IIA.4. Cross sections of this magnitude are consistent with a dielectric constant of between 3 and 3.5.

Table IIA.4
The Radar Back-scatter Cross-section of Mars

Frequency	σ	Reference
S-band, 12.5 cm	0.085	[Goldstein, 1966]
L-band, 43 cm	0.07	[Kotel'nikov et al, 1964]
L-band, 70 cm	0.07	[Dyce et al, 1967]

The dielectric constant and its variations provide an important clue to the nature of the planet's surface.

Differentiation of the Martian surface causes the radar cross section to vary with the position on the disc of the sub-radar point. The cross section at 12.5 cm and 70 cm wavelength is plotted in Figure IIA6 as a function of the longitude of the sub-radar point [Pettengill and Evans, 1967]. The latitude of the sub-radar point was 20°N at the time of the measurements. A strip map appears across the top of the figure showing the principal optical features of Mars at this latitude.

The rotation of Mars imparts Doppler frequency shifts to the back-scattered signal. The width of the peak in the frequency spectrum is a measure of the r.m.s. surface slope of topographic structure on a scale greater than the wavelengtn. The r.m.s. surface slope on Mars appears to be ~6°, measured at 12.5 and 70 cm wavelengths [Goldstein and Gilmore, 1963; Dyce et al., 1967], compared to 8° on the moon.

(f) GROSS THERMAL PROPERTIES

The temperature of Mars has been measured remotely at the earth in both the infrared and the microwave regions of the electromagnetic spectrum. These measurements employ methods of radiometry, based on Planck's radiation law.

The infra-red temperature at midday on the Martian equator is 298°K for a light area or 306°K for a dark area [Sinton and Strong, 1960]. The range of the diurnal temperature variation on the equator is estimated to be 140°K [Goody, 1967].

The average microwave brightness temperature of the Martian disc at opposition is 190° ± 12°K over a range of wavelengths from 1mm to 21 cm [Dent et al., 1965; Klein, 1967].

If the surface emissivity is 0.89, as determined from the radar reflectivity, the actual average temperature is 214°K ± 14°K.

The phase variation of the disc microwave brightness temperature is less than 5°K (at least over the range of phase angles observable from earth, -25° → +40°). [Dent et al., 1965].

(g) MAGNETIC FIELD AND RADIATION BELTS

At closest approach to Mars (a radial distance from the center of the planet of 13,200 km.) Mariner IV detected no evidence of a Martian magnetic field or of Martian radiation belts [various authors, 1965]. As a result, in scaling from the magnetosphere of the Earth, the magnetic moment of Mars is smaller than 3×10^{22} gauss cm^3, which implies an equatorial surface magnetic field of less than $\sim 10^{-3}$ gauss, compared to $\sim$0.5 gauss on earth.

(h) SATELLITES

Two small satellites, Phobos and Deimos, revolve around Mars in nearly circular orbits, very slightly inclined to the planets equatorial plane. Physical and orbital data referring to the satellites are given in Table IIA.5 [Melbourne et al., 1968; Michaux, 1967].

TABLE IIA.5

Known physical and orbital parameters of Martian satellites

Satellite	a	P	e	i	m_v	R
Phobos	∿9	0.319	0.0170	0.95	12.1	∿8
Deimos	∿23	1.262	0.0031	1.73	13.3	∿4

a = distance from Mars' center in km x 10^3

i = inclination to Laplacian plane in °

P = orbital period in sidereal days

m_v = visual magnitude at opposition

e = eccentricity

R = estimated radius in km

The following facts are noteworthy regarding Mars' satellites:

(i) The precession of Mars' satellites provides a measure of Mars' dynamic flattening (= ratio of the difference between equatorial and polar radii to the equatorial radius), $f_d = .00525$, versus a value $f_o = .0105$ for the optical flattening the source of this discrepancy is yet unresolved.

(ii) Due to Phobos' short period of revolution around Mars, equal to $\sim$1/3 Martian day, it rises in the west with respect to an observer fixed on the planet.

(iii) An apparent secular acceleration of Phobos towards Mars has been deduced from observations of the former's orbit. The reality of this effect is still disputed and its potential cause is unresolved..

(IIA) GENERAL PHYSICAL PROPERTIES OF MARS - REFERENCES

Dent, W. A., M. J. Klein and H. D. Aller, "Measurements of Mars at λ 3.75 cm from February to June, 1965," Astroph. J., 142, 1685-1688, 1965.

de Vaucouleurs, G., "Geometric and photometric parameters of the terrestrial planets," Icarus 3, 187-235, 1964.

de Vaucouleurs, G., "A low resolution map of Mars," Icarus, 7, 310-349, 1967.

Devine, C. J., "JPL development ephemeris number 19," J.P.L. Tech. Rep. No. 32-1181, 1967.

Dollfus, A., "Study of the planets by means of the polarization of their light," NASA TT F-188, Washington, D. C., 1964.

Dyce, R. B., G. H. Pettengill and A. D. Sanchez, "Radar observations of Mars and Jupiter at 70 cm," Astron. J., 72, 771-777, 1967.

Goldstein, R., "J.P.L. Radar observations of Mars," Proceedings of the Caltech - J.P.L. Lunar and Planetary Conference, J.P.L. TM 33-266, 239, 1966.

Goldstein, R. M. and W. F. Gillmore, "Radar observations of Mars," Science, 141, 1171-1172, 1963.

Goody, R. M., Personal communication, 1967.

Hagfors, T., "Backscattering from an undulating surface with applications to radar returns from the moon," J. Geophys. Res., 69, 3779-3784, 1964.

Klein, M. J., personal communication, 1967.

Motel'nikov, V. A. et al., "Radar studies of the planet Mars in the Soviet Union," in translation, Sov. Phys. Doklady 8, 760-763, 1964.

Melbourne, W. G., J. D. Mulholland, W. L. Sjogren and F. M. Sturms, Jr., "Constants and related information for astrodynamic calculations, 1968," J.P.L. Tech. Rep. 32-1306, 1968.

Michaux, C. M., Handbook of the Physical Properties of the Planet Mars, NASA SP-3030, 1967.

Pettengill, G. H. and J. V. Evans, "3.8 cm radar observations of the surface and atmosphere of Venus and Mars," to be published.

Sinton, W. M. and J. Strong, "Radiometric observations of Mars," Ap. J. 131, 459-469, 1960.

(IIB) SURFACE PROPERTIES OF MARS

(a) GENERAL APPEARANCE

The Martian surface has a sufficiently permanent topography that regions may be easily identified, and can be divided into three distinct types by color:

white areas or polar caps

bright areas or continents

dark areas.

Some regions, notable Solis Lacus, Nepenthes and Casius, undergo continual change, and all parts of the planet are subject to alteration of the pattern between dark and light areas.

Numerous maps of the surface of Mars have been prepared, based on telescopic observations [for example North American, 1962].

(b) POLAR CAPS

The polar caps are bright, white deposits located near the north and south poles. The southern polar cap is centered on latitude -83°, longitude 30° [de Vaucouleurs, 1954]. The northern polar cap is centered close to the north pole. The edges of the polar caps advance in local Martian autumn and recede in local Martian spring. The median latitudes of the caps, averaged over many years, are given as a function of the heliocentric longitude of Mars (or equivalently, time) in Figure IIB1 [Antoniadi, 1930]. The caps are bordered by a discontinuous dark fringe which is apparent in local spring [Dollfus, 1946; Dollfus, 1947]. While the caps are receding, their borders are broken by dark inlets, and islands of white are left outside the general region of caps in the same places each year. During the period in which they form, the caps are obscured by clouds.

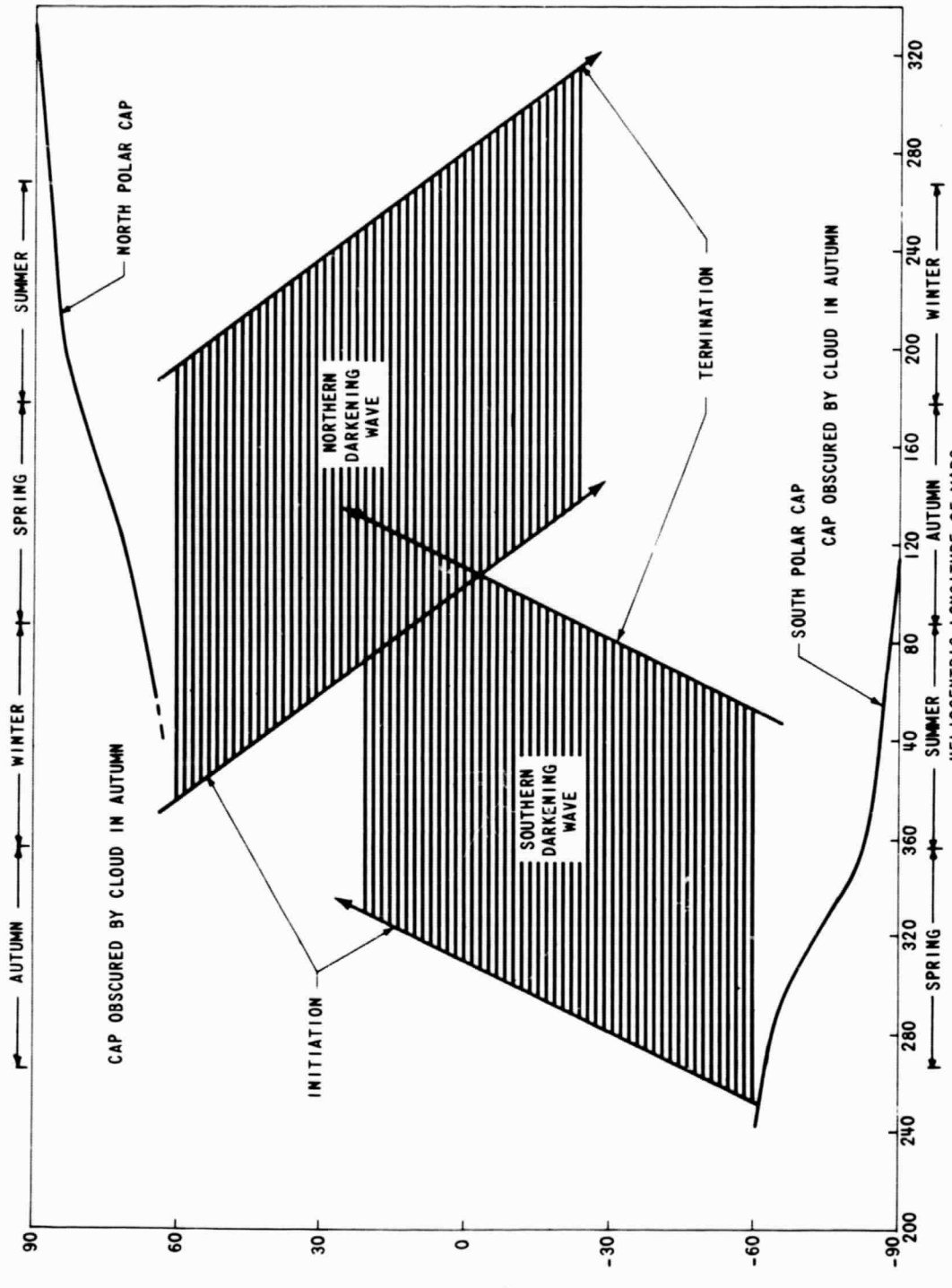

FIGURE IIBI - LATITUDE BOUNDARIES OF THE POLAR CAPS AND THE DARKENING WAVE ON MARS AS A FUNCTION OF THE HELIOCENTRIC LONGITUDE OF THE PLANET (OR EQUIVALENTLY, TIME). THE SHADED AREA INDICATES, FOR A GIVEN LATITUDE, THE TIME DURING WHICH DARKENING IS APPARENT. THE GREATEST DARKENING OCCURS MIDWAY BETWEEN INITIATION AND TERMINATION OF THE WAVE

It is believed that the polar caps are composed of either solid water or solid carbon dioxide, but there is no conclusive evidence in favor of either hypothesis.

(c) BRIGHT AREAS

These regions, which have a generally orange color, occupy about two thirds of the planet's surface. There is a slight variation in color among different bright regions. Mariner IV photographs show that those bright areas observed, ∿1% of the surface of Mars, are relatively rough, with a high density of large craters, rills and other features [Leighton, 1967]. Optical polarization measurements and the existence of dust storms indicate that the bright areas are covered with a fine grained material.

(d) DARK AREAS

The dark areas are of three types: small spots, short linear features, and extended regions. The dark areas are largely concentrated in the southern hemisphere, particularly near the equator. They are generally grey, but brown, blue and green are seen in individual small regions. Mariner IV photographs show a lower frequency of craters in the dark than in the bright areas.

The dark areas are affected by waves of darkening which propagate from each pole in local spring, and which proceed across the equator to about 22° latitude of the opposite hemisphere. The latitudes of the boundaries of the two waves are given as a function of the heliocentric longitude of Mars (or equivalently, time) in Figure IIB1 [Focas, 1961].

(e) THERMAL PROPERTIES

The gross pattern of temperature distribution on the surface of Mars and the seasonal variations of this pattern can be inferred from Figure IIB2 [after Gifford, 1952]. The isotherm maps in this Figure were constructed from the reduction of ∿1300 radiometric measurements in the infrared, by several

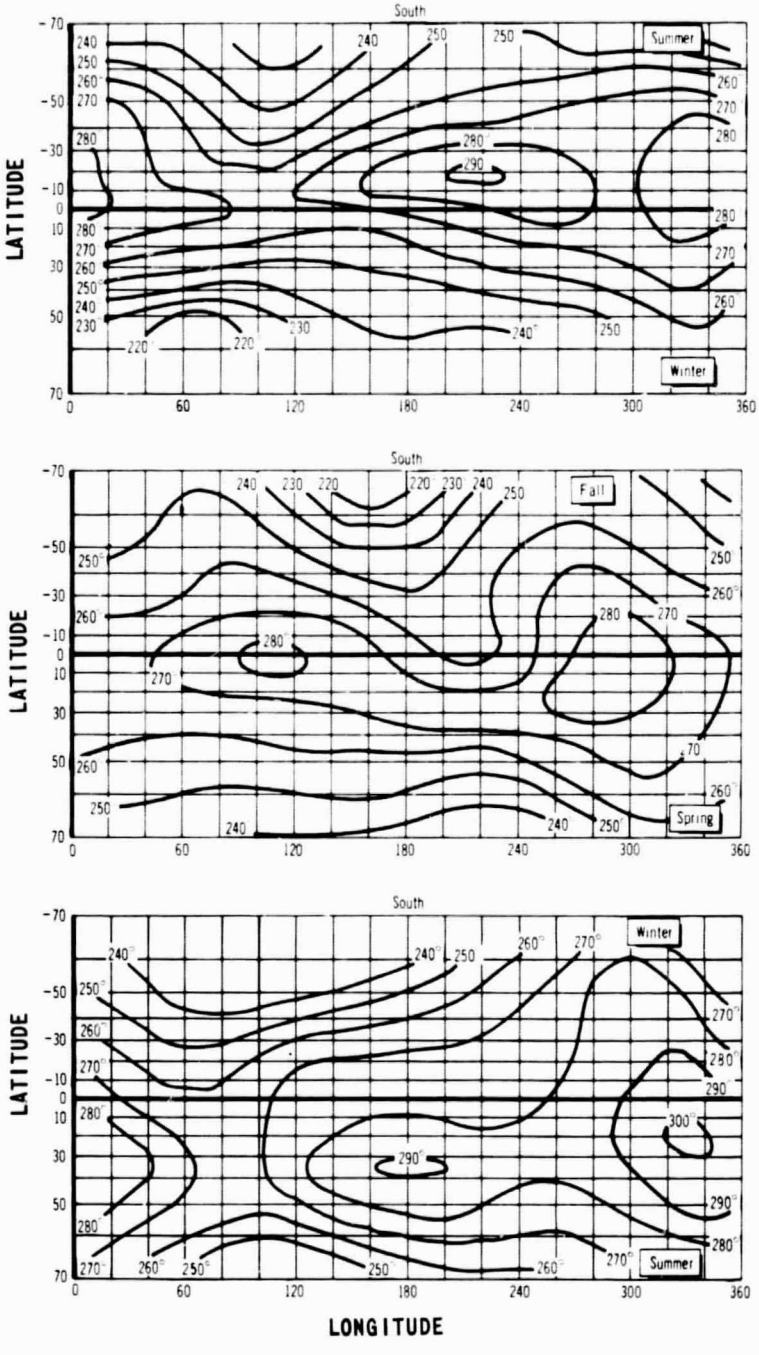

FIGURE IIB2 - AVERAGE MARTIAN ISOTHERMS.
(AFTER GIFFORD, 1952)

observers between 1926 and 1943. Because of a ∿20% uncertainty in surface emissivity, and the latter's possible spatial variations, the real temperatures and isothermal contours may differ from those given in Figure IIB2. Yet, within these uncertainties, amounting to ∿10°K in temperature, and corresponding uncertainties in the exact location of contours, Figure IIB2 is the best summary of empirical knowledge on the subject.

A limited number of accurate infrared temperature drift curves over the sunlit surface of Mars [Sinton and Strong, 1960] form the basis for models of the diurnal variation of surface temperature, illustrated in Figure IIB3 [Leighton and Murray, 1966]. These models take into account thermal conduction in the Martian surface layer, assuming this to be a semi-infinite homogeneous solid, characterized by a thermal parameter $(k\rho c)^{1/2}$. $(k\rho c)^{1/2}$, known as thermal inertia, is a proportionality factor linking the surface heat flux to temperature variations [Carslaw and Yaeger, 1959]. It depends on the material properties of the solid, namely its heat conductivity k cal cm^{-1} sec^{-1} $°K^{-1}$, its density ρ gm cm^{-3}, and its specific heat c cal gm^{-1} $°K^{-1}$. The models of diurnal temperature variation are also subject to the uncertainties mentioned above.

The observed microwave temperature variation of the Martian disc [see Section IIA] is compatible with the infrared temperatures within the thermal model.

(f) TOPOGRAPHY

Radar Doppler shift observations, in the decimeter range, indicate a relatively smooth surface on Mars, with an r.m.s. slope of ∿5° on the meter scale [Goldstein and Gilmore, 1963; Dyce et al., 1967]. Mariner IV photography suggests an r.m.s. slope of ∿3° on a scale of > 3 km [Leighton et al., 1967]. Radar echo delay measurements indicate that Mars is also much smoother than earth on a continental scale [Counselman et al., 1968].

Both types of radar observations suggest elevation differences on the order of 12 km [Sagan and Pollack, 1968; Counselman et al., 1968]. Figure IIB4 shows an elevation profile of the Martian surface along a line of latitude at 21°N [Pettengill, 1967]. No clear correlation has been established between surface elevation and the location of visible bright and dark areas [Pettengill, 1967; Counselman et al., 1968].

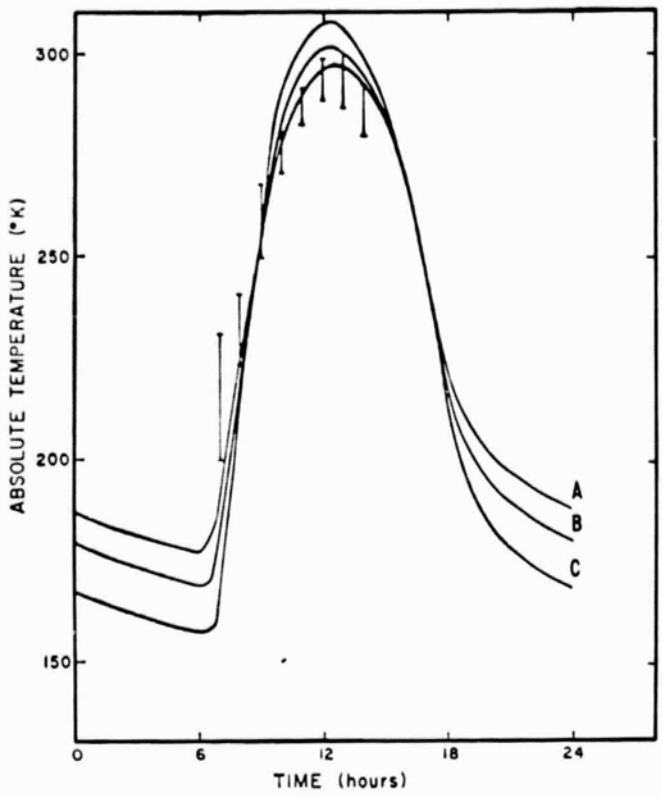

FIGURE IIB3 -
DIURNAL VARIATION OF SURFACE TEMPERATURE IN THE EQUATORIAL REGION OF MARS. VERTICAL BARS-SINTON AND STRONG'S OBSERVATIONS. ASSUMED VALUES OF $(K\rho C)^{\frac{1}{2}}$: CURVE A-0.0055, CURVE B-0.0042, CURVE C-0.003

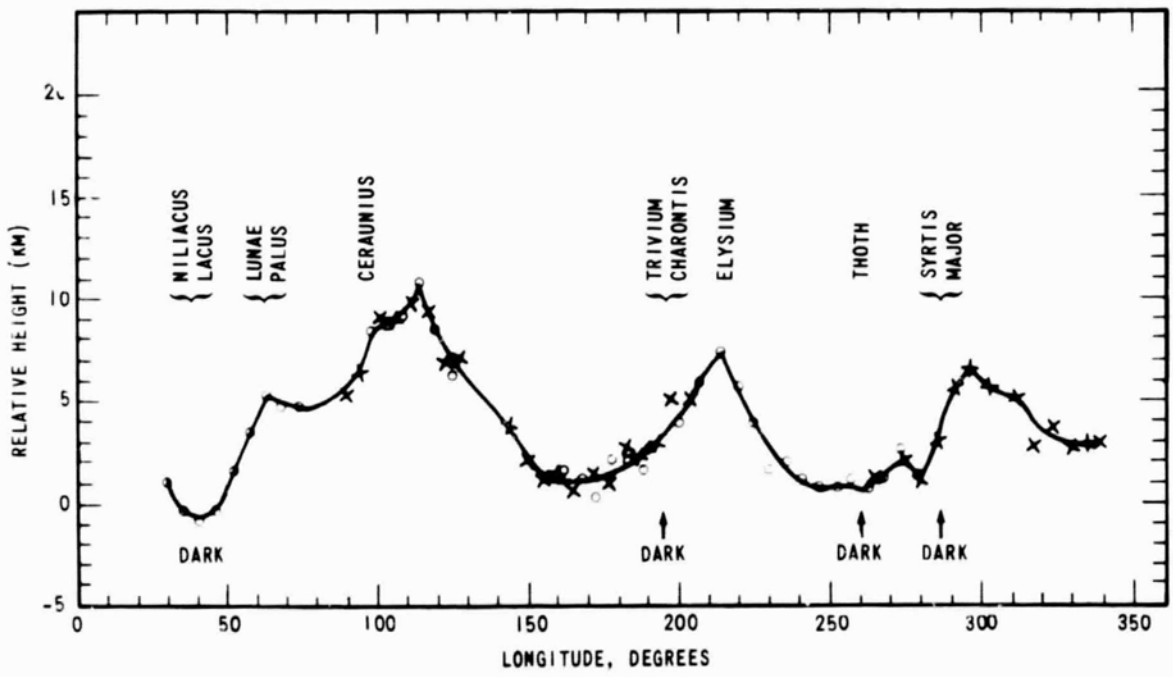

FIGURE IIB4 - MARTIAN HEIGHT PROFILE AT 21°N LATITUDE OBTAINED FROM VERTICAL INCIDENCE RADAR RANGING AT 3.8 CM WAVELENGTH. SOME SURFACE FEATURES AND OPTICALLY DARK REGIONS AT 21°N ARE LISTED (AFTER PETTENGILL, 1967)

(g) SOIL MECHANICS

In the absence of direct empirical evidence, models of mechanical properties of the Martian surface soil are based on the similarity of the optical characteristics of Mars' surface to those of terrestrial materials, and on analogy to lunar surface properties. Subject to the limitations of this method, the Martian surface layer can be regarded as fine grained material of very low cohesion and medium porosity. Grain sizes are estimated to be in the range of $\sim$0.1-$\sim$10.0μ, with the bulk of particle sizes near 2-4μ; the porosity is estimated at $\sim$50%, and the density at 1.2-1.5 gm cm^{-3}; the probable mean angle of friction is 30-35° [Scott, 1968; Vaughan and Weidner, 1967].

(IIB) SURFACE PROPERTIES OF MARS - REFERENCES

Antoniadi, E. M., La Planète Mars, Hermann et C^ie, Paris, 1930.

Carslaw, H. S. and J. C. Jaeger, Conduction of Heat in Solids, 2nd ed., Oxford Univ. Press, London, 1959.

Counselman, C. C., G. H. Pettengill and I. I. Shapiro, "Topography on Mars", Trans. Am. Geophys. U., 49, 271, 1968.

de Vaucouleurs, G., Physics of the Planet Mars, Faber and Faber, London, 1954.

Dollfus, A., "La frange sombre polaire de la planète Mars en 1943-1944", L'Astronomie, 60, 132-134, 1946.

Dollfus, A., Erratum, L'Astronomie, 61, 63, 1947.

Dyce, R. B., G. H. Pettengill and A. D. Sanchez, "Radar observations of Mars and Jupiter at 70 cm", Astron. J., 72, 771-777, 1967.

Focas, J. H., "Etude photomètrique et polarimètrique des phènoménes saisonniers de la planète Mars", Annales d'Astrophysique, 24, 309-325, 1961.

Gifford, F. Jr., "Surface temperatures of the planet Mars", pp. 218-249 in The Study of Planetary Atmospheres, Lowell Obs. Rep., 1952.

Goldstein, R. M., and W. F. Gilmore, "Radar observations of Mars", Science, 141, 1171-1172, 1963.

Leighton, R. B., a paper presented at the I.A.U. meeting, Prague, August 1967.

Leighton, R. B. and B. C. Murray, "Behavior of carbon dioxide and other volatiles on Mars", Science, 153, 136-144, 1966.

Leighton, R. B., B. C. Murray, J. D. Allen and R. K. Sloan, "Mariner IV pictures of Mars", App. H., pp. 145-154, J.P.L. Tech. Rep. 32-884, 1967.

North American Aviation, Inc., "The planet Mars", Space and Information Systems Division, Pub. 540-L Rev. 3-62, 1962.

Pettengill, G. H., paper presented at 13th General Assembly, Intern. Astron. Union, Prague, 1967.

Sagan, C. and J. B. Pollack, "Elevation differences on Mars", J. Geophys. Res., 73, 1373-1387, 1968.

Scott, R. F., private communication, 1968.

Sinton, W. M., and J. Strong, "Radiometric observations of Mars", Ap. J., 131, 459-569, 1960.

Vaughan, O. H. and D. K. Weidner, eds., "Environment of Mars: an interpretation of atmospheric and surface characteristics", NASA TMX-53668, 1967.

(IIC) ATMOSPHERIC PROPERTIES OF MARS

(a) COMPOSITION

Present knowledge of the composition of the Martian atmosphere is mainly derived from the study of Martian absorption spectra with both earth-based and balloon-borne telescopes. A limited number of constituents have been identified in this way [Spencer, 1966; Michaux, 1967]. No in situ chemical analysis of the Martian atmosphere has been performed to date.

However, the results of the Mariner IV RF Occultation experiment [Kliore et al., 1965; Fjeldbo et al., 1966a] are consistent with spectroscopic studies, in confirming CO_2 as a principal constituent of the atmosphere below ∿30 km, amounting probably to no less than 50%, and possibly up to 100% of the content of the Martian atmosphere. Argon and Nitrogen, two other likely major constituents, lack spectroscopic features to permit identification by astronomical methods. Their presence in sizable quantities can only be surmised on various grounds, and is not inconsistent with the Mariner IV data.

Astronomical studies of minor constituents have so far only succeeded in detecting minute quantities of water vapor, and in obtaining upper limits to the abundance of other likely gases such as CO, O and O_2. These limiting abundances are too small to affect the results of the RF occultation experiment.

Above ∿90 km the presence of a sizable electron concentration was observed in the Mariner IV RF occultation experiment. The problem of the composition of the corresponding positive ion layer is still unresolved.

Table IIC.1 summarizes present information on the composition of the neutral atmosphere of Mars.

Table IIC.1

Composition of the Martian atmosphere

Gas	Abundance		%	Remarks
	gm cm^{-2}	cm-atm		
CO_2	$\gtrsim$10.0	$\gtrsim$ 5×10^3	50-100	
N_2	$\lesssim$ 3.5	$\lesssim 27 \times 10^3$	0-20	not observed
A	$\lesssim$10.0	$\lesssim$ 5×10^3	0-50	not observed
H_2O (vapor)	< 0.004	< 5	<0.04	
CO	< 0.012	<10	<0.012	spectroscopic upper limits
O_2	< 0.035	<25	<0.35	

(b) TEMPERATURE PROFILE

A crude but fairly direct measure of the temperature in the lower Martian atmosphere is provided by earth-based infrared radiometry of the planetary surface [Sinton and Strong, 1960; Michaux, 1967]. Determination of the atmospheric scale height from the refractivity profile below 30 km in the Mariner IV experiment [Kliore et al., 1965] yielded a more refined estimate of the temperature profile below that altitude, at the points of immersion into occultation and emersion from it. The electron scale height in the ionosphere above 125 km provides an estimate of temperature in the upper atmosphere; this estimate depends, however, on the assumed composition of positive ions. The temperature profile in the altitude gap between 30 and 125 km is obtained from a combination of theoretical considerations [Fjeldbo et al.,

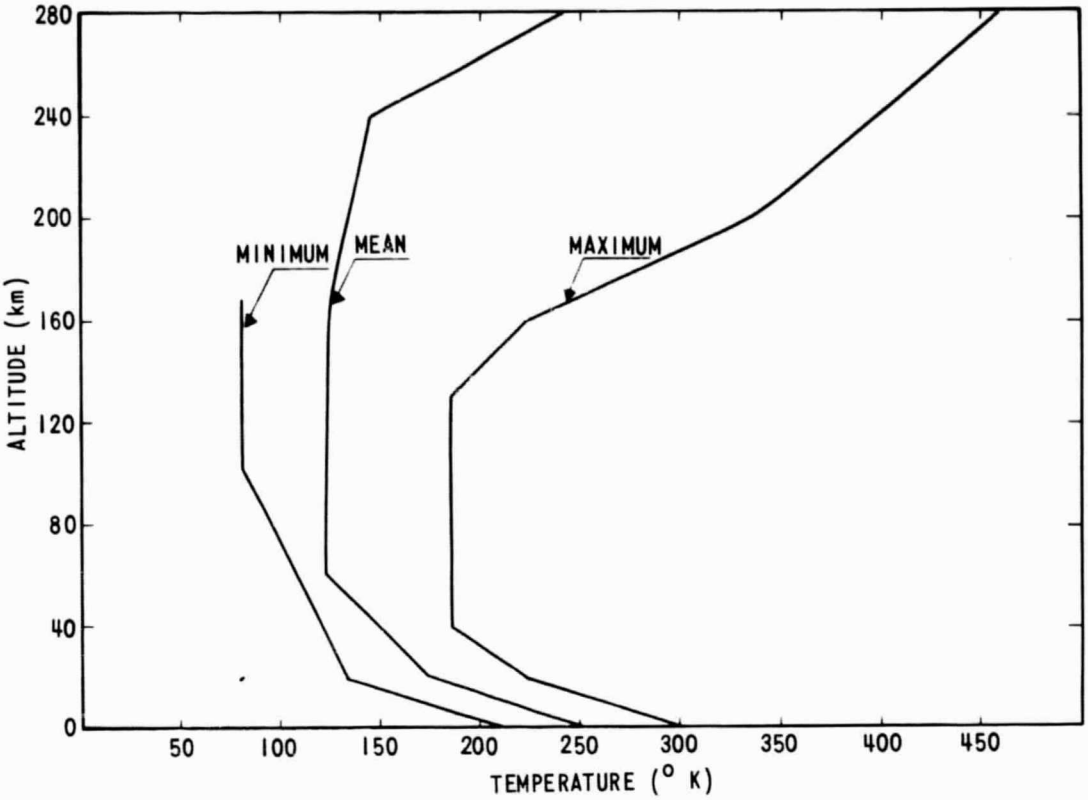

FIGURE IIC1 - ATMOSPHERIC TEMPERATURE PROFILE OF MARS (FROM NASA SP-8010)

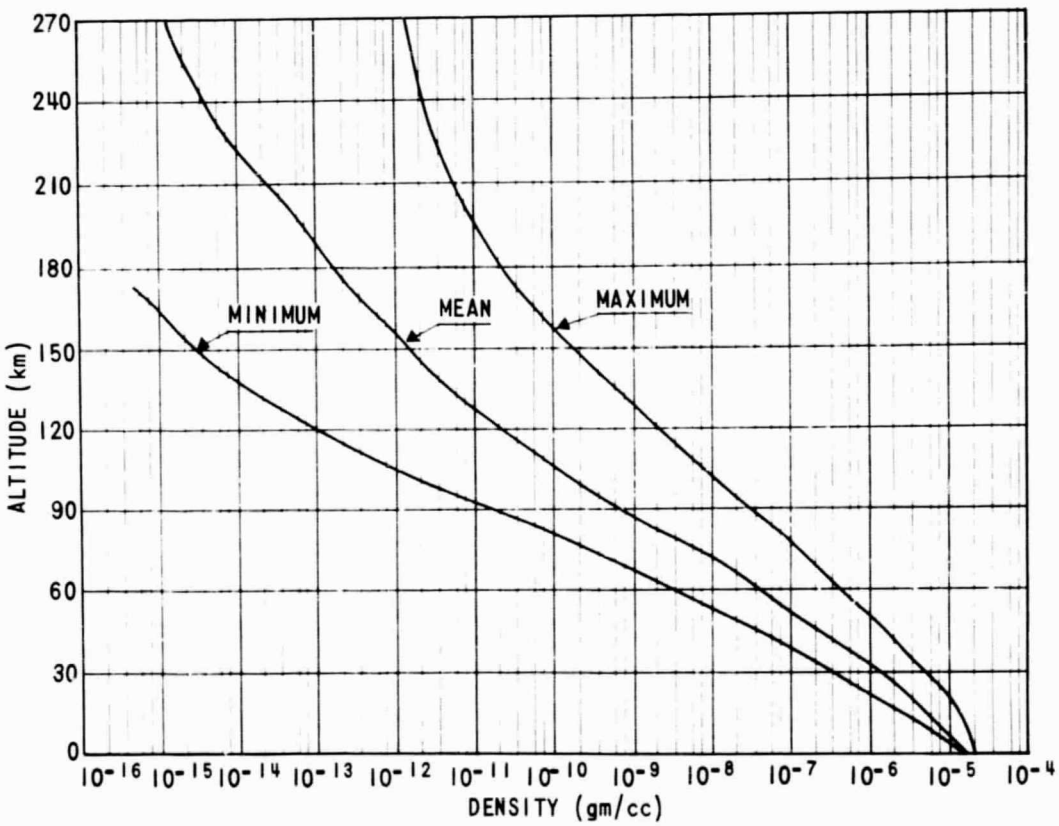

FIGURE IIC2 - ATMOSPHERIC DENSITY PROFILE OF MARS (FROM NASA SP-8010)

1966a; 1966b; Michaux, 1967] and best estimates of the observed values at the boundaries. A similar procedure is adopted to obtain the temperature profile above ionospheric peak.

For lack of sufficient empirical data no unique average temperature profile of the Martian atmosphere can be determined at present. But on the basis of the available data model atmospheres have been constructed by NASA [NASA, SP-8010, 1968]. The model atmospheres, spanning a reasonable range of values of relevant atmospheric parameters, are intended to serve as engineering standards. Table IIC.2 summarizes the NASA 1967 model atmosphere parameters for Mars. Figure IIC1 shows the temperature profiles adopted for the three NASA 1967 model atmospheres.

Table IIC.2

Summary of NASA 1967 Mars Model Atmosphere parameters

Parameters \ Model	Maximum	Mean	Minimum
Surface pressure, mb	15	7	5
CO_2, % by mass	50	80	100
CO_2 % by volume	38.9	71.8	100
N_2, % by mass	50	20	0
N_2, % by volume	61.1	28.2	0
Surface temperature, °K	300	250	210

(c) PRESSURE AND DENSITY PROFILES

Some realistic estimates of surface pressure (or density) on Mars have been obtained in the past from interpretation of earth-based spectroscopic observations [Chamberlain and Hunten, 1965]. Mariner IV results have, in general, corroborated

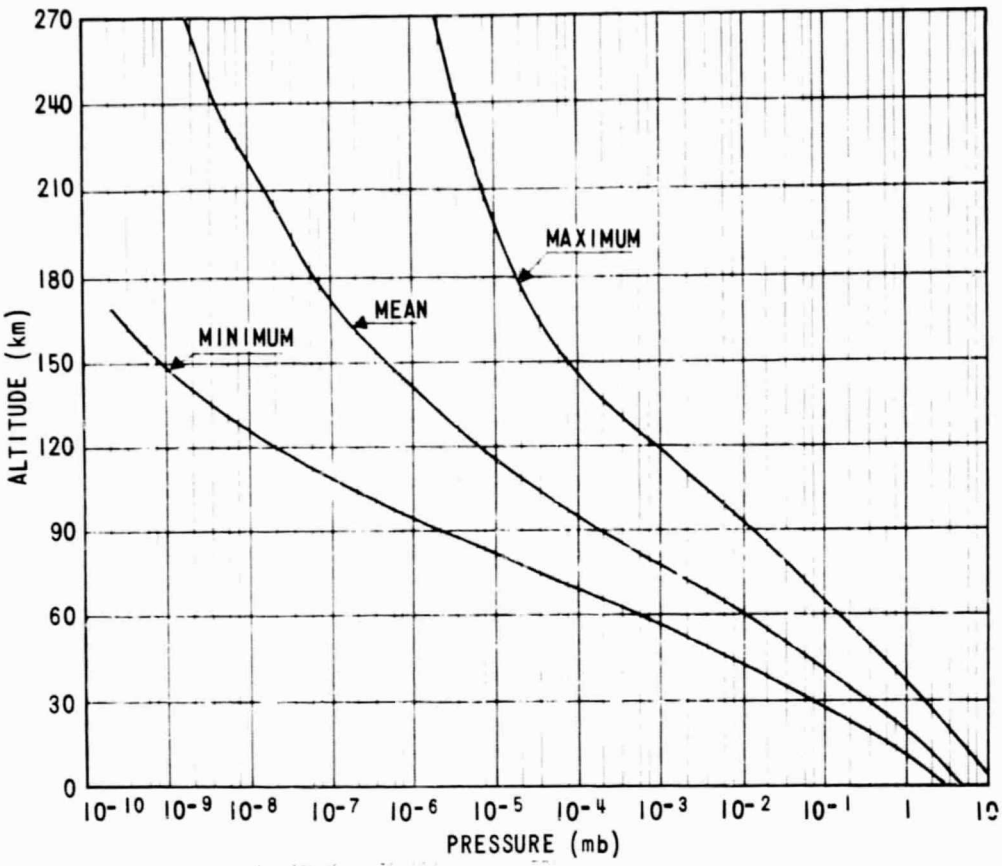

FIGURE IIC3 - ATMOSPHERIC PRESSURE PROFILE (FROM NASA SP-0010)

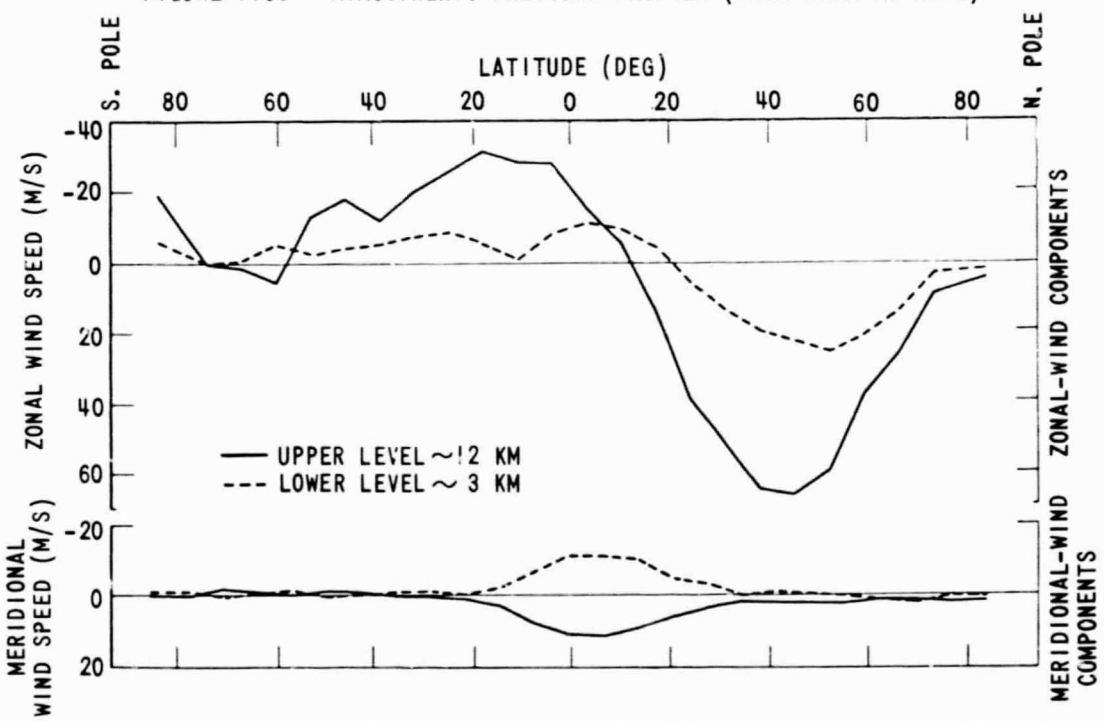

FIGURE IIC4 - MEAN ZONAL AND MERIDIONAL WIND PROFILES FOR MARS. POSITIVE ZONAL WINDS ARE FROM THE WEST; POSITIVE MERIDIONAL WINDS ARE FROM THE SOUTH. (AFTER LEOVY AND MINTZ, 1966)

the lower of these estimates. Knowledge of the atmospheric temperature profile, and some assumptions on the chemical composition of the Martian atmosphere and its variations with altitude permit the construction of temperature and pressure profiles, based on the hydrostatic equation:

$$dp = -g\rho dz$$

where p is the pressure, ρ is the density, and z is height above the surface. The density is obtained from the equation of state for an ideal gas:

$$p = \frac{\rho}{M} RT$$

where R is the universal gas constant, and T the absolute temperature.

Figures IIC2 and IIC3 present the density and pressure profiles of the three model atmospheres; the numerical values of the relevant parameters are tabulated in Tables IIC.3 through IIC.5 [NASA SP-8010, 1967].

It should be noted that the models presented here do not take complete account of diurnal, seasonal and solar cycle variations. The effects of these become important at high altitudes: at 1000 km above the surface the atmospheric density may vary by one order of magnitude between day and night, and by three orders of magnitude between solar maximum and minimum [NASA CR-61185].

(d) IONOSPHERE

The peak electron density in the daytime ionosphere observed in the Mariner IV experiment was $\sim 10^5$ electrons cm^{-3} at $\sim$125 km [Fjeldbo et al., 1966a; Fjeldbo et al., 1966b]. The upper limit of the nighttime electron density was found to be less than 10^3 electrons cm^{-3}.

TABLE IIC.3

NASA 1967 MINIMUM MARS MODEL ATMOSPHERE*

Geometric Altitude (km)	Temp (K)	Pressure (mb)	Density (gm/cc)	Speed of sound (m/sec)	Molecular Weight	Density Scale Height (km)	Number Density (Per cc)	Mean Free Path (m)	Viscosity (kg/m sec)
0	210.0	5.00+0	1.26-5	230	44.0	14.14	1.72+17	8.36-6	1.06-5
5	185.0	3.03+0	8.65-6	217	44.0	12.50	1.18+17	1.22-5	0.91-5
10	160.1	1.71+0	5.63-6	203	44.0	10.85	7.71+16	1.87-5	0.76-5
15	139.4	8.76-1	3.33-6	190	44.0	7.43	4.55+16	3.17-5	0.65-5
20	136.1	4.29-1	1.67-6	188	44.0	7.18	2.28+16	6.31-5	0.64-5
25	132.9	2.07-1	8.26-7	186	44.0	7.03	1.13+16	1.28-4	0.62-5
30	129.6	9.85-2	4.02-7	184	44.0	6.88	5.51+15	2.62-4	0.61-5
35	126.4	4.61-2	1.93-7	182	44.0	6.72	2.64+15	5.46-4	0.59-5
40	123.1	2.11-2	9.09-8	179	44.0	6.57	1.24+15	1.16-3	0.58-5
45	119.9	9.54-3	4.21-8	177	44.0	6.42	5.76+14	2.50-3	0.56-5
50	116.7	4.22-3	1.91-8	175	44.0	6.27	2.62+14	5.50-3	0.55-5
55	113.5	1.83-3	8.53-9	173	44.0	6.11	1.17+14	1.23-2	0.54-5
60	110.3	7.76-4	3.72-9	170	44.0	5.96	5.10+13	2.83-2	0.52-5
65	107.1	3.22-4	1.59-9	168	44.0	5.80	2.18+13	6.62-2	0.51-5
70	104.0	1.30-4	6.64-10	166	44.0	5.65	9.09+12	1.59-1	0.50-5
75	100.8	5.19-5	2.68-10	164	43.3	5.47	3.73+12	3.87-1	0.48-5
80	97.7	2.04-5	1.07-10	163	42.6	5.41	1.51+12	9.52-1	0.47-5
85	94.5	7.94-6	4.23-11	163	41.8	5.35	6.09+11	2.37+0	0.47-5
90	91.4	3.05-6	1.65-11	160	41.1	5.28	2.42+11	5.96+0	0.46-5
95	88.1	1.19-6	6.18-12	163	38.2	5.17	9.75+10	1.48+1	0.45-5
100	85.0	4.81-7	2.39-12	167	35.2	5.37	4.10+10	3.52+1	0.44-5
110	85.0	9.53-8	4.00-13	181	29.7	6.03	8.12+9	1.78+2	0.44-5
120	85.0	2.37-8	8.87-14	192	26.4	7.01	2.02+9	7.13+2	0.44-5
130	85.0	6.97-9	2.29-14	205	23.2	7.83	5.94+8	2.43+3	0.44-5
140	85.0	2.41-9	6.85-15	221	20.1	8.80	2.05+8	7.02+3	0.44-5
150	85.0	9.75-10	2.34-15	240	17.0	9.94	8.31+7	1.73+4	0.44-5
160	85.0	4.32-10	1.02-15	242	16.7	12.24	3.68+7	3.91+4	0.44-5
170	85.0	1.94-10	4.54-16	243	16.5	12.43	1.65+7	8.71+4	0.44-5
180	85.0	8.83-11	2.04-16	245	16.3	12.63	7.53+6	1.92+5	0.44-5
190	85.0	4.07-11	9.31-17	246	-16.2	12.83	3.47+6	4.16+5	0.44-5

*A one-or two-digit number (preceded by a plus or minus sign) following an entry indicates the power of ten by which that entry should be multiplied.

TABLE IIC.4

NASA 1967 MEAN MARS MODEL ATMOSPHERE*

Geometric Altitude (km)	Temp (K)	Pressure (mb)	Density (gm/cc)	Speed of sound (m/sec)	Molecular Weight	Density Scale Height (km)	Number Density (Per cc)	Mean Free Path (m)	Viscosity (kg/m sec)
0	250.0	7.00+0	1.33-5	265	39.5	17.77	2.03+17	7.39-6	1.31-5
5	231.3	4.84+0	9.93-6	256	39.5	16.49	1.51+17	9.9 -6	1.22-5
10	212.6	3.24+0	7.24-6	246	39.5	15.21	1.10+17	1.36-5	1.13-5
15	194.0	2.10+0	5.14-6	236	39.5	13.92	7.83+16	1.91-5	1.04-5
20	175.4	1.30+0	3.52-6	225	39.5	12.62	5.37+16	2.79-5	0.91-5
25	168.8	7.81-1	2.20-6	221	39.5	10.36	5.55+16	4.47-5	0.87-5
30	162.5	4.60-1	1.34-6	217	39.5	10.00	2.05+16	7.31-5	0.84-5
35	156.2	2.66-1	8.08-7	213	39.5	9.65	1.23+16	1.22-4	0.80-5
40	150.0	1.50-1	4.76-7	209	39.5	9.29	7.26+15	2.06-4	0.77-5
45	143.7	8.32-2	2.75-7	204	39.5	8.92	4.19+15	3.57-4	0.74-5
50	137.5	4.49-2	1.55-7	200	39.5	8.56	2.37+15	6.33-4	0.71-5
55	131.3	2.36-2	8.55-8	196	39.5	8.20	1.30+15	1.15-3	0.68-5
60	125.1	1.21-2	4.58-8	191	39.5	7.83	6.99+14	2.15-3	0.65-5
65	125.0	6.07-3	2.31-8	191	39.5	7.29	3.52+14	4.26-3	0.65-5
70	125.0	3.06-3	1.16-8	191	39.5	7.31	1.77+14	8.45-3	0.65-5
75	125.0	1.55-3	5.87-9	191	39.5	7.33	8.95+13	1.67-2	0.65-5
80	125.0	7.84-4	2.94-9	192	39.0	7.13	4.54+13	3.30-2	0.65-5
85	125.0	4.05-4	1.47-9	195	37.8	7.36	2.35+13	6.38-2	0.65-5
90	125.0	2.14-4	7.54-10	199	36.6	7.59	1.24+13	1.21-1	0.65-5
95	125.0	1.16-4	3.94-10	202	35.4	7.84	6.71+12	2.23-1	0.65-5
100	125.0	6.40-5	2.11-10	205	34.2	8.11	3.71+12	4.04-1	0.65-5
110	125.0	2.08-5	6.39-11	213	31.9	8.68	1.21+12	1.24+0	0.65-5
120	125.0	7.40-6	2.10-11	221	29.5	9.33	4.29+11	3.50+0	0.65-5
130	125.0	2.84-6	7.54-12	228	27.6	10.08	1.64+11	9.12+0	0.65-5
140	125.0	1.16-6	2.88-12	237	25.8	10.76	6.74+10	2.22+1	0.65-5
150	125.0	5.10-7	1.17-12	246	23.9	11.52	2.96+10	5.07+1	0.65-5
160	125.0	2.39-7	5.07-13	256	22.0	12.37	1.39+10	1.08+2	0.65-5
170	136.3	1.22-7	2.25-13	273	21.0	13.11	6.46+9	2.32+2	0.70-5
180	147.9	6.75-8	1.10-13	291	20.0	14.76	3.30+9	4.54+2	0.76-5
190	157.8	3.99-8	5.97-14	303	19.7	17.14	1.83+9	8.19+2	0.81-5
200	167.6	2.46-8	3.41-14	314	19.3	18.54	1.06+9	1.41+3	0.87-5
220	187.1	1.04-8	1.25-14	337	18.6	21.46	4.04+8	3.71+3	0.99-5
240	206.4	4.99-9	5.23-15	360	18.0	24.55	1.75+8	8.55+3	1.11-5
260	225.5	2.63-9	2.43-15	382	17.3	27.80	8.46+7	1.77+4	1.19-5
280	244.4	1.50-9	1.23-15	404	16.7	31.23	4.46+7	3.36+4	1.28-5
300	263.1	9.18-10	6.73-16	426	16.0	34.84	2.53+7	5.93+4	1.37-5
320	281.5	5.93-10	3.90-16	448	15.4	38.62	1.53+7	9.82+4	1.47-5
340	299.8	4.02-10	2.38-16	471	14.8	42.59	9.72+6	1.54+5	1.57-5
360	317.9	2.84-10	1.52-16	494	14.1	46.74	6.48+6	2.31+5	1.64-5
380	335.7	2.08-10	1.01-16	518	13.5	51.06	4.50+6	3.33+5	1.72-5

*A one-or two-digit number (preceded by a plus or minus sign) following an entry indicates the power of ten by which that entry should be multiplied.

TABLE IIC.5

NASA 1967 MAXIMUM MARS MODEL ATMOSPHERE*

Geometric Altitude (km)	Temp (K)	Pressure (mb)	Density (gm/cc)	Speed of Sound (m/sec)	Molecular Weight	Density Scale Height (km)	Number Density (Per cc)	Mean Free Path (m)	Viscosity (kg/m sec)
0	300.0	1.50+1	2.06-5	313	34.2	25.91	3.62+17	4.34-6	1.69-5
5	280.7	1.15+1	1.69-5	304	34.2	24.31	2.97+17	5.29-6	1.58-5
10	261.5	8.66+0	1.36-5	294	34.2	22.71	2.40+17	6.54-6	1.47-5
15	242.3	6.39+0	1.09-5	283	34.2	21.11	1.91+17	8.22-6	1.37-5
20	223.2	4.60+0	8.48-6	272	34.2	19.51	1.49+17	1.05-5	1.27-5
25	210.4	3.23+0	6.32-6	265	34.2	15.46	1.11+17	1.41-5	1.21-5
30	202.5	2.24+0	4.55-6	260	34.2	14.92	8.00+16	1.96-5	1.17-5
35	194.6	1.53+0	3.23-6	255	34.2	14.37	5.69+16	2.76-5	1.12-5
40	186.6	1.03+0	2.27-6	250	34.2	13.83	3.99+16	3.94-5	1.07-5
45	178.8	6.81-1	1.57-6	245	34.2	13.28	2.76+16	5.69-5	1.03-5
50	170.9	4.43-1	1.07-6	240	34.2	12.74	1.88+16	8.36-5	0.98-5
60	160.0	1.78-1	4.57-7	232	34.2	10.74	8.05+15	1.95-4	0.92-5
70	160.0	7.03-2	1.81-7	232	34.2	10.80	3.18+15	4.94-4	0.92-5
80	160.0	2.80-2	7.15-8	233	34.0	10.84	1.27+15	1.24-3	0.92-5
90	160.0	1.13-2	2.85-8	234	33.5	10.98	5.12+14	3.06-3	0.92-5
100	160.0	4.66-3	1.16-8	236	33.0	11.19	2.11+14	7.44-3	0.92-5
120	160.0	8.47-4	2.01-9	242	31.5	11.74	3.83+13	4.10-2	0.92-5
140	161.5	1.69-4	3.79-10	249	30.0	11.16	7.60+12	2.07-1	0.93-5
160	224.1	4.84-5	7.19-11	304	27.7	14.52	1.57+12	1.00+0	1.28-5
180	286.0	2.06-5	2.19-11	356	25.3	19.49	5.21+11	3.01+0	1.61-5
200	336.0	1.10-5	9.12-12	401	23.3	25.66	2.36+11	6.64+0	1.84-5
220	375.5	6.65-6	4.59-12	439	21.5	33.96	1.28+11	1.22+1	2.00-5
240	403.5	4.35-6	2.63-12	468	20.3	38.08	7.81+10	2.01+1	2.11-5
260	431.3	3.01-6	1.60-12	498	19.1	42.41	5.05+10	3.11+1	2.21-5
280	458.7	2.18-6	1.02-12	530	17.8	46.93	3.45+10	4.56+1	2.32-5
300	485.9	1.65-6	6.79-13	564	16.6	51.58	2.46+10	6.38+1	2.42-5
320	512.7	1.29-6	4.69-13	600	15.4	56.32	1.83+10	8.59+1	2.52-5
340	538.0	1.05-6	3.41-13	632	14.6	69.70	1.41+10	1.12+2	2.61-5
360	561.8	8.62-7	2.58-13	658	14.0	74.76	1.11+10	1.41+2	2.70-5
380	585.3	7.24-7	1.99-13	685	13.4	79.93	8.96+9	1.75+2	2.79-5
400	608.6	6.17-7	1.56-13	714	12.8	85.18	7.35+9	2.14+2	2.87-5
500	707.4	3.34-7	5.99-14	844	10.6	129.20	3.42+9	4.60+2	
600	781.2	2.15-7	3.01-14	957	9.1	184.80	2.00+9	7.87+2	
700	827.0	1.53-7	1.82-14	1038	8.2	213.38	1.34+9	1.17+3	
800	870.5	1.16-7	1.17-14	1127	7.3	242.55	9.67+8	1.62+3	
900	907.9	9.31-8	8.02-15	1218	6.5	330.08	7.43+8	2.11+3	
1000	924.1	7.72-8	6.00-15	1282	6.0	360.70	6.05+8	2.60+3	

*A one-or two-digit number (preceded by a plus or minus sign) following an entry indicates the power of ten by which that entry should be multiplied.

(e) CLOUDS AND HAZE

Three main types of clouds have been observed in the Martian atmosphere:

1) White Clouds - large moving systems in equatorial or temperate zones, or thick shrouds over the winter pole, enduring for several months.

2) Blue Clouds - similar to white clouds, but reflect only blue and ultra-violet light. Circumstantial evidence indicates that blue clouds are located at high altitudes, between ∿15 and possibly 100 km.

3) Yellow Clouds - show great variability, in both size and mobility. Occasionally observed on a planetary scale; in most cases, however, smaller formations with sizes starting from the resolution limit of ∿100 km.

4) Blue Haze - obscuration of surface features when viewed at wavelengths shorter than ∿4500 Å. Occasionally haze clears, and surface detail becomes visible in the blue as well. No explanation of the blue haze and its clearing is universally accepted at present.

(f) WIND

Estimated wind velocities on Mars and models of prevailing circulation patterns are derived in three distinct ways:

(a) construction of a general circulation pattern in the atmosphere, based on the requirement of thermodynamic equilibrium;

(b) inference of average and local wind speeds from observed weather phenomena, such as cloud motions;

(c) estimate of threshold wind velocities necessary to generate and sustain the observed dust clouds.

Of these methods, the first one appears most reliable. Results obtained from a general circulation model [Leovy and Mintz, 1966] form the basis for NASA design criteria [NASA SP-8010, 1967]. These list the strongest mean winds - over all longitudes - as westerlies with a velocity of 66 m sec^{-1} at 12 km altitude in the winter hemisphere; easterly winds predominate in the summer hemisphere, reaching a mean of 29 m sec^{-1} at the above altitude near the equator. Figure IIC4 [Leovy and Mintz, 1966] illustrates these results. The above analysis includes maximum wind speeds of 162 m sec^{-1} at 12 km and 38 m sec at the planet's surface.

The wind velocities quoted above are to be interpreted only as large scale mean motions, and their numerical values may be subject to modification.

Observations of cloud drifts yielded $\sim$25 m sec^{-1} as an estimate for the average convective velocity. On the assumption of a 1-3 mb depression at the storm center, local wind speeds of 140 m sec^{-1} were predicted as likely to be encountered in a weather system [Ohring, Tang, Mariano, 1965].

From reasonable assumptions about surface roughness and grain size, these authors estimate that the threshold wind speed necessary for generation of dust clouds lies between 14 and 55 m sec^{-1}.

All quoted estimates were obtained using techniques and approximations tested on applications in the earth's atmosphere. Consequently, they should be interpreted with due caution.

(IIC) ATMOSPHERIC PROPERTIES OF MARS - REFERENCES

Chamberlain, J. W. and D. M. Hunten, "Pressure and CO_2 Content of the Martian atmosphere: A critical discussion," Rev. Geophys., 3, 299, 1965.

Fjeldbo, G., W. C. Fjeldbo, and Von R. Eshleman, "Models for the atmosphere of Mars based on the Mariner 4 occultation experiment," J. Geophys. Res., 71, 2307, 1966a.

Fjeldbo, G., W. C. Fjeldbo and Von R. Eshleman, "Atmosphere of Mars: Mariner IV models compared", Science, 153, 1518, 1966b.

Kliore, A., Cain. D. L., Levy, G. S., Eshleman, V. R., Fjeldbo, G. and F. D. Drake, "Occultation experiment results of the first direct measurement of Mars' atmosphere and ionosphere", Science, 149, 1243, 1965.

Leovy, C. B. and Y. Mintz, "A numerical general circulation experiment for the atmosphere of Mars", Memorandum RM-5110-NASA, The Rand Corp., 1966.

Michaux, C. M., Handbook of the Physical Properties of the Planet Mars, NASA SP-3030, 1967.

NASA SP-8010, "Models of Mars atmosphere (1967)", NASA, 1968.

NASA CR-61185, "Mars atmosphere definition final report: Voyager Spacecraft", 1968.

Ohring, G., Tang W. and J. Mariano, "Planetary meteorology", NASA CR-280, 1965.

Sinton, W. M. and J. Strong, "Radiometric observations of Mars", Astrophys. J., 131, 459-469, 1960.

Spencer, D. F., "Our present knowledge of the Martian atmosphere", pp. 532-541 in AIAA/AAS Stepping Stones to Mars Meeting, AIAA, New York, 1966.

(III) VENUS

(IIIA) GENERAL PHYSICAL PROPERTIES OF VENUS

(a) INTRODUCTION

Venus moves in a nearly circular orbit, with an eccentricity of ∿0.0068 and a period of ∿0.615 earth years. The synodic period of Venus varies from ∿580 to ∿588 days, with a mean of ∿584 days; its closest distance from earth varies from ∿0.265 to 0.289 A.U. In distinction from the rotation of all other planets that of Venus is retrograde. Relevant physical parameters of Venus are given in Table IIIA.1 [Allen, 1963; De Vaucouleurs, 1964; Melbourne et al., 1968b, NASA SE 015-001-1, 1965]. Precise data on state vectors of Venus are contained in JPL Development Ephemeris Tape Number 19 [Devine, 1967].

Table IIIA.1

Physical parameters of Venus

Ratio of Venus' mass to earth's mass	).8150004
Gravitational parameter	3.248601×10^{20} cm^3 sec^{-2}
Equatorial diameter, optical	$(1.2240 \pm 0.0015) \times 10^9$ cm
Equatorial diameter, radar	$(1.2104 \pm 0.0006) \times 10^9$ cm
Rotation period (sidereal)	242.6±1 days
Mean distance from the sun	0.7233316 A.U. = 1.082089×10^{13} cm
Eccentricity (1970)	0.0067873
Mean orbital velocity	35.02 km sec^{-1}
Inclination of orbit to ecliptic (1970)	3°23'39.6"

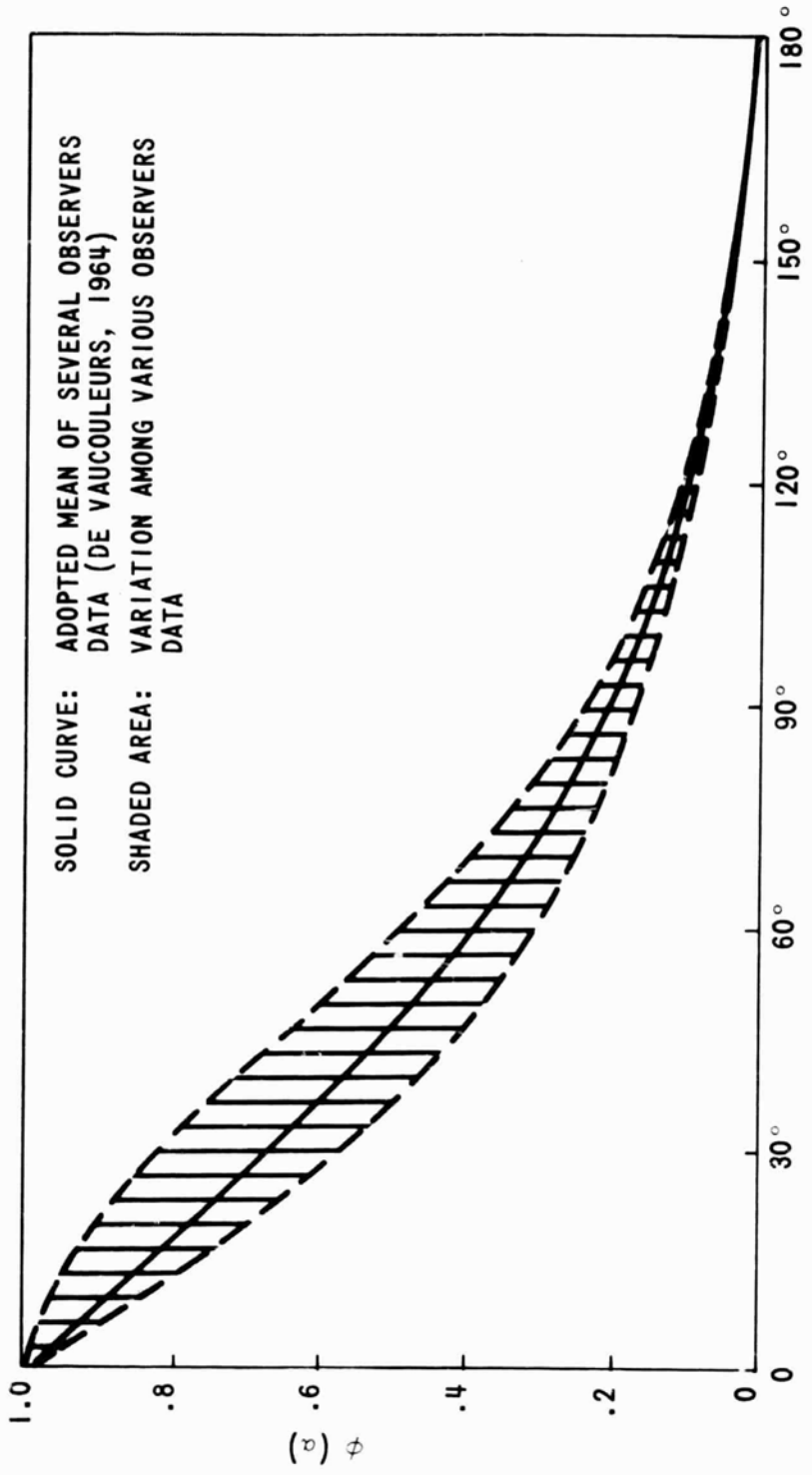

FIGURE IIIA1 - VISUAL PHASE FUNCTION OF VENUS

(b) GEOMETRIC AND PHOTOMETRIC RELATIONSHIPS

These relationships are defined for Venus in the same way as for Mars [see Section (IIA) (b)].

(c) PHOTOMETRIC PROPERTIES OF VENUS

The available photometric data on Venus are limited to those obtained from the light integrated over the whole planetary disk. The orbit of Venus lies inside the orbit of the earth, and so the phase function $\phi(\alpha)$ is available over all phase angles. $\phi(\alpha)$, measured in the visible spectrum, is plotted in Figure IIIA1 [de Vaucouleurs, 1964]. $\phi(\alpha)$ has also been measured in the ultraviolet [Knuckles et al., 1968].

The values of the geometric albedo P, the phase integral g, and the spherical albedo A, for visible light--standardized to the "V" photometric system with effective wavelength $\lambda = 0.55\mu$--are [de Vaucouleurs, 1964]:

$$p = 0.650$$

$$g = 1.087$$

$$A = 0.70$$

(d) POLARIMETRY

The degree of polarization, P, is defined for Venus as for Mars [Section (IIA) (d)]. In Figure IIA2 and IIA3 P is plotted as a function of phase angle for various spectral bands in the visible and in the infrared. Figure IIA2 refers to the whole disk, whereas Figure IIA3 refers to a region near the equator, which is likely to be typical [Dollfus, 1966].

(e) RADAR REFLECTIVITY AND SCATTERING

Due to the perpetual cloud cover of Venus and its optically opaque atmosphere, radar observations are an essential source of information on the properties of the planet's body and surface. Analysis of the radar reflectivity of Venus has yielded: (i) the average dielectric constant of the surface; (ii) atmospheric absorption; (iii) variability of surface

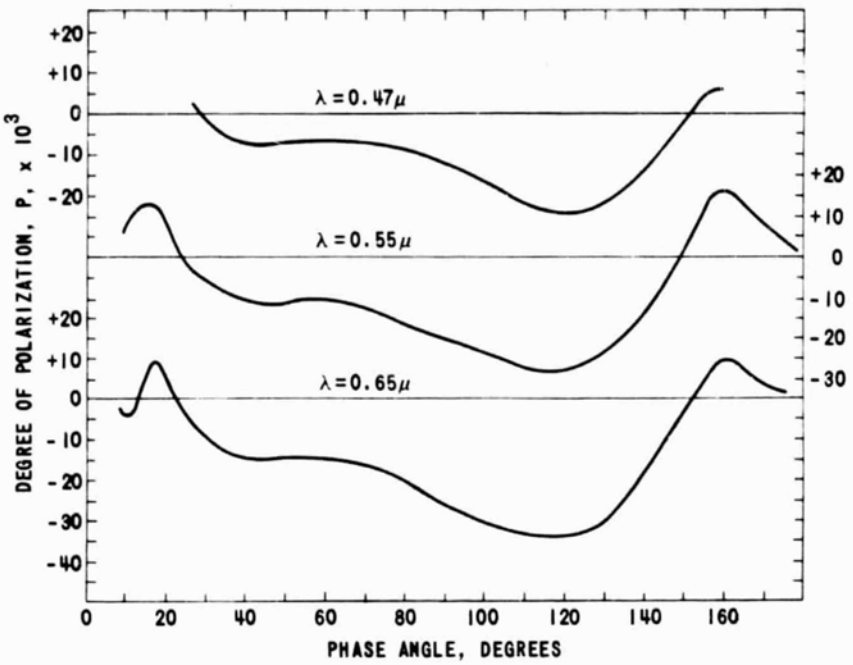

FIGURE IIIA2 - VISUAL POLARIZATION CURVES OF VENUS .47μ - UPPER LEFT SCALE, .55μ - RIGHT SCALE, .65μ - LOWER LEFT SCALE. OBSERVATIONS REFER TO A REGION NEAR THE EQUATOR, MIDWAY BETWEEN LIMB AND TERMINATOR (AFTER DOLLFUS, 1966)

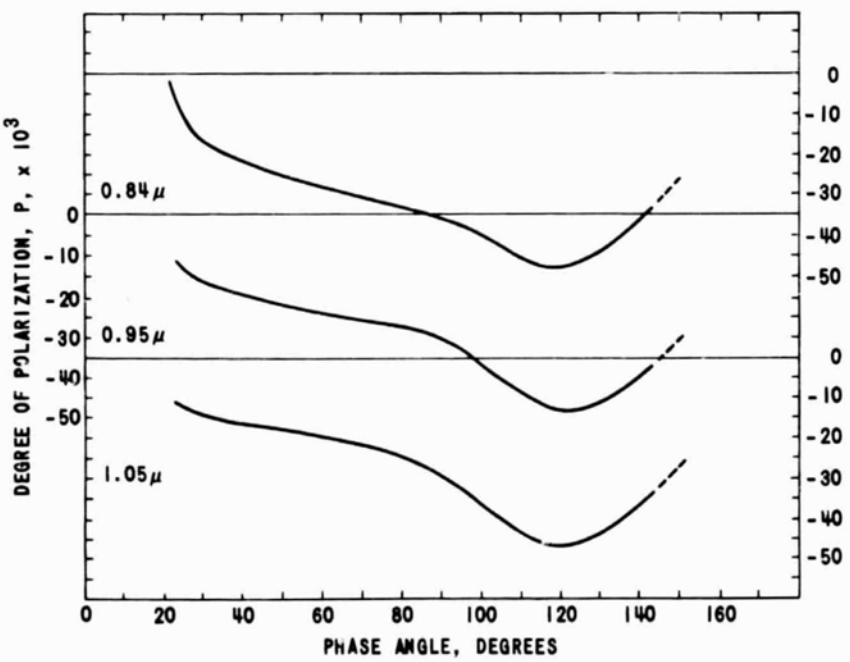

FIGURE IIIA3 - POLARIZATION CURVES OF VENUS IN THE INFRARED 0.8μ - UPPER RIGHT SCALE; 0.95μ - LEFT SCALE, 1.05μ - LOWER RIGHT SCALE. (AFTER DOLLFUS, 1966)

roughness and presence of surface features; (iv) the average surface slope; (v) the radius of Venus; (vi) the rotation parameters of the planet.

The average dielectric constant of Venus, ε, is obtained from its radar cross section σ_r [see Section (IIA) (e)]. σ_r of Venus, as a function of wavelength, λ, is shown in Figure IIIA4 [Evans, 1968]. The variation of σ_r from $\sim$0.071 at 3.8 cm to a constant value of $\sim$0.15 above $\sim$20 cm is ascribed to atmospheric absorption, which is thought to decrease with increasing λ, and to be negligible above $\sim$20 cm. The observed variability of σ at a given λ - observed at all wavelengths - is attributed to changing roughness and reflectivity, as the sub-radar terrain varies from observation to observation. If cross sectional data below 20 cm are discounted because of the uncertain contribution of atmospheric absorption, a dielectric constant $\varepsilon \sim 5$ is derived, under the assumption that the geometric factor is g=1 [Pettengill et al., 1962].

Information on average *surface slope* is derived in radar observations from the angular power spectrum, which analyzes the power of the radar return echo as a function of angle of incidence of the radar wave on the planet. The angular power spectrum is obtained either from the frequency spectrum of continuous-wave radar echos [Carpenter, 1964; Muhleman, 1964] or from the time delay power spectrum of pulsed radar echos [Beckman and Kemperer, 1965]. These methods indicate that Venus is smoother than the moon on a large scale, but that local slopes are steeper. More details on surface properties will be found in Section (IIIB).

Combination of radar and astronomical data on the orbital motion of earth, the moon, Venus and Mercury, and radar time-delay measurements [Ash et al., 1967] have yielded a highly accurate value for the radius of the solid body of Venus [Ash et al., 1968; Melbourne et al., 1968a]. The radius of Venus, obtained in this manner, is found to be $\sim 6050 \pm 5$ km.

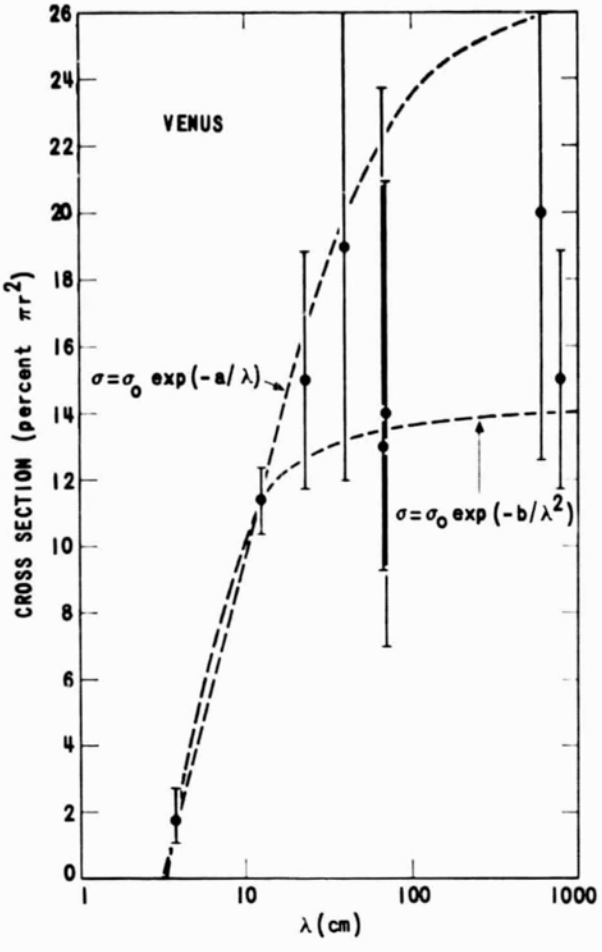

FIGURE IIIA4 -

THE RADAR CROSS SECTION OF VENUS VS WAVELENGTH. ALSO SHOWN ARE TWO CURVES COMPUTED FOR SIMPLE MODELS OF THE ABSORBING BEHAVIOR OF THE CYTHEREAN ATMOSPHERE. BOTH CURVES HAVE BEEN FORCED TO PASS THROUGH THE POINTS OBTAINED AT λ = 3.8 AND λ = 12.5 CM. (AFTER EVANS, 1968).

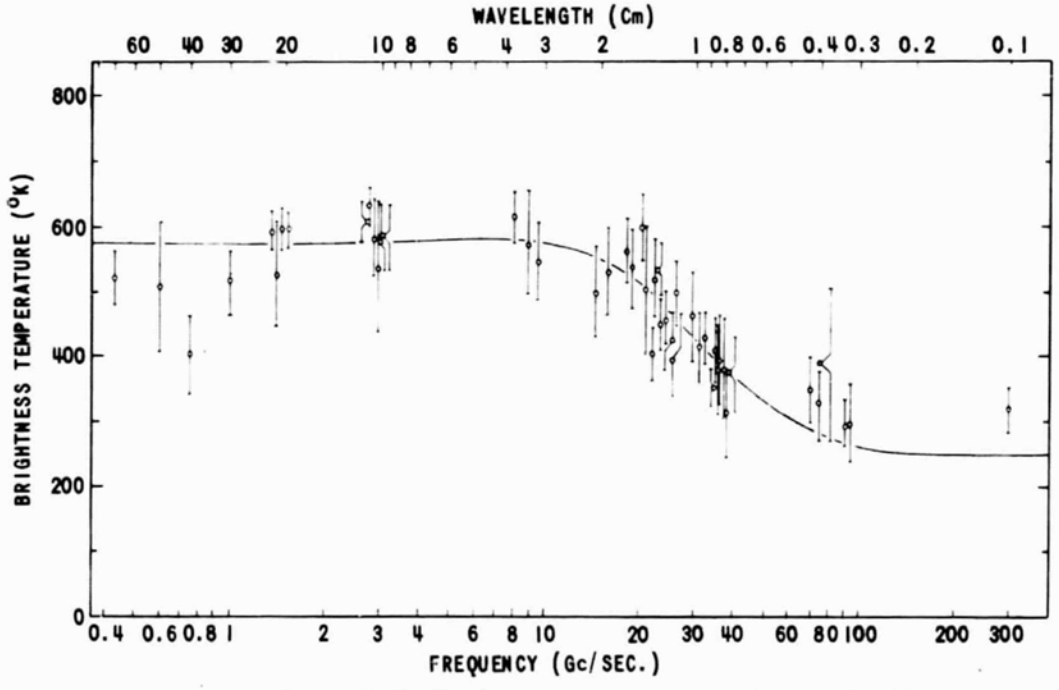

FIGURE IIIA5 - THE OBSERVED MICROWAVE BRIGHTNESS TEMPERATURE OF VENUS (AFTER HO ET AL., 1966)

By analyzing the Doppler spread of radar echos from Venus, and by long term observation of the motion of surface features, the rotation period of Venus has been determined, as well as the direction of its rotation axis, e.g. [Shapiro, 1967]. The values of these parameters given in this reference are

Period = 243.09±0.18 days, retrograde

North Pole R. A. = 275±1.8°

Declination = 65.8±1.2°

These values are in substantial agreement with other recent determinations.

(f) GROSS THERMAL PROPERTIES

The infrared temperature of Venus, measured between 8-12μ, is approximately 234°K [Sinton and Strong, 1963], and is apparently independent of phase [Murray et al., 1963]. This uniform temperature is generally believed to refer to the top of the Venusian cloud layer.

The average microwave brightness temperature is a strong function of wavelength, which is shown in Figure IIIA5. Similar to the wavelength variation of the radar cross section, the brightness temperature increases with increasing wavelength, and reaches an approximately constant value in the decimeter region [Ho et al., 1966]. This suggests that the brightness temperature of ∿600°K at longer wavelengths is attributable to emission from the surface, believed to be at a true temperature of ∿700°K; at shorter wavelengths cooler atmospheric layers account for the lower observed brightness temperature.

As with the average brightness temperature, a marked wavelength dependence is observed in the phase effect of the microwave temperature, which is illustrated in Table IIIA.1. Here ΔT°K denotes the amplitude of the variation from the mean temperature T_o°K and "θ_o" is the phase lag angle, measured from superior conjunction. The brightness temperature at a given phase is expresses as

$$T_B = T_o + \Delta T \cos(\dot{\theta} - \theta_o)$$

Table IIIA.2

Microwave phase effect of Venus

λ(cm)	T_o°K	ΔT°K	θ
0.34	-299	-11±2	0±5
0.8	427	41	2
0.86	380	27	0
3.15	621	73±6	11.7±22
3.75	646	60	
10.00	622	41±12	21±9
10.60		<15	
11.3		∿25	
21.2	597	<12	

(g) MAGNETIC FIELD AND RADIATION BELTS

At closest approach to Venus, at a radial distance of ∿10,150 km from the planet's center, Mariner V detected no evidence of a Venusian magnetic field or of radiation belts [Bridge et al., 1967; Van Allen et al., 1967]. As a result, on scaling from the magnetosphere of the earth [see Section (IC) (e)], the magnetic moment of Venus is estimated to be smaller than $\sim 1 \times 10^{23}$ gauss cm^3, versus $\sim 8.07 \times 10^{25}$ gauss cm^3 on earth.

(IIIA) GENERAL PHYSICAL PROPERTIES OF VENUS - REFERENCES

Allen, C. W., Astrophysical Quantities, 2nd. ed., University of London, The Athlone Press, London, 1963.

Ash, M. E., I. I. Shapiro and W. B. Smith, "Astronomical constant and planetary ephemerides deduced from radar and optical observations," Astron. J., 72, 338-350, 1967.

Ash, M. E., D. B. Campbell, R. B. Dyce, R. P. Ingalls, R. Jurgens, G. H. Pettengill, I. I. Shapiro, M. A. Slade and T. W. Thompson, "The case for the radar radius of Venus," Science, 160, 985-987, 1968.

Beckman, P. and W. R. Klemperer, "Interpretation of the angular dependence of back-scattering from the moon and Venus," J. Res. NBS, 69D, 1669-1677, 1965.

Bridge, H. S., P. J. Coleman, L. Davis, Jr. D. E. Jones, A. J. Lazarus, E. J. Smith, and C. W. Snyder, "Mariner V: plasma and magnetic field observed near Venus," Science, 158, 1669-1673.

Carpenter, R. L. "Studies of Venus by C W radar," Astron. J., 69, 2-11, 1964.

De Vaucouleurs, G., "Geometric and photometric parameters of the terrestrial planets," Icarus, 3, 187-235, 1964.

Devine, C. J., "JPL development ephemeris number 19," J.P.L. Tech. Rep. No. 32-1181, 1967.

Dollfus, A., "Contribution au colloque Caltech--J.P.L. sur la lune et les planets: Venus," pp. 187-202, Proc. of the Caltech-J.P.L. Lunar and Planetary Conference, J.P.L. TM 33-266, 1966.

Evans J. V., "Variations in the radar cross section of Venus," Astron. J., 73, 125-134, 1968.

Ho, W., I. A. Kaufman and P. Thaddeus, "Laboratory measurement of microwave absorption in models of the atmosphere of Venus," J. Geophys. Res., 71, 5091, 1966.

Knuckles, C. F., M. F. Sinton and W. M. Sinton," UBV photometry of Venus," Lowell Observ. Bull., 115, 153-156, 1961.

Melbourne, W. G., D. O. Muhleman, D. A. O'Handley, "Radar determination of the radius of Venus," Science, 160, 987-988, 1968a.

Melbourne, W. G., J. D. Mulholland, W. L. Sjogren and F. M. Sturms, Jr. "Constants and related information for astrodynamical calculations, 1968," J.P.L. Tech. Rep. 32-1306, 1968b.

Muhleman, D. O., "Radar scattering from Venus and the moon," Astron. J., 69, 34-41, 1964.

Murray, B. C., R. L. Wildey and J. A. Westphal, "Infrared photometric mapping of Venus through the 8 to 14 micron atmospheric window," J. Geophys. Res., 68, 4813-4818, 1963.

NASA, SE 015-001-1, "Natural environment and physical standards for the Apollo program," April, 1965.

Pettengill, G. H., H. W. Briscoe, J. V. Evans, E. Gehrels, G. M. Hyde, L. G. Kraft, R. Price and W. B. Smith, "A radar investigation of Venus," Astron. J., 67, 181-190, 1962.

Shapiro, I. I., "Resonance rotation of Venus," Science, 157, 423-425, 1967.

Sinton, W. M. and J. Strong, "Radiometric observations of Venus," Astron. J., 131, 475-483, 1960.

Van Allen, J. A., S. M. Krimigis, L. A. Frank and T. P. Armstrong, "Venus: an upper limit on intrinsic magnetic dipole moment based on absence of a radiation belt," Science, 158, 1673-1675, 1967.

(IIIB) SURFACE PROPERTIES OF VENUS

(a) INTRODUCTION

The solid body of Venus appears to be completely enveloped in an opaque layer of clouds that obstruct observation of the planet's surface at optical and nearby wavelengths. Microwave radiation, at cm and longer wavelengths, penetrates to the surface. but observations in this spectral region are of poor spatial resolution. At best an effective resolution of a sizeable fraction of the planet's disk is attained with passive interferometric methods, compared to the optical solution of Martian surface detail on a scale of $\sim$ 50 km. Such fine resoultion has been recently approached by radar interferometric studies of Venus, but results of the latter pertain to reflecting properties of the planetary surface in the microwave region, whose interpretation is somewhat ambiguous.

(b) TOPOGRAPHY

In view of the introductory remarks, topographical information on the surface of Venus is limited to certain statistical characteristics deduced from radio observations, such as average surface slope or roughness, while information on surface differentiation and surface features is available only with respect to radar scattering properties.

Mean surface roughness or mean surface slope is deduced from the observed power reflected to the radar receiver, by introducing the so-called back-scattering function, $P(\phi)$. $P(\phi)$ expresses the relative amount of back-scattered power as a function of the mean angle of incidence, ϕ, on the reflecting surface. The shape of $P(\phi)$ is sensitive to the mean surface slope or roughness, on the scale of the applied wavelength.

Two alternative methods can be used to obtain $P(\phi)$ from the immediate observational results. The rotation of Venus imparts to the reflected CW radar signal a Doppler broadened power spectrum $P_s(f)$, with a center-to-limb bandwidth f_o, where f denotes frequency. By means of the transformation

$$P(\phi) \propto \cos \phi \int_{f_o \sin \phi}^{f_o} \frac{dp_s(f)/df}{(f^2 - f_o^2 \sin^2 \phi)^{1/2}} \, df$$

$P(\phi)$ is obtained from the observed $P_s(f)$. Typical shapes of $P_s(f)$ and $P(\phi)$ of Venus are shown in Figures IIIB1 and IIIB2 [Carpenter, 1966]; for comparison the latter figure contains a curve of $P(\phi)$ for the moon.

In pulsed radar echo delay measurements one obtains $P(\phi)$ directly from the delay power spectrum $P(\tau)$, since ϕ and τ are related by

$$\phi = \cos^{-1}\left(1 - \frac{c\tau}{2r}\right)$$

where τ is the delay, c the velocity of light, and r the planetary radius. Figure IIIB3 [Pettengill et al, 1967] shows Venus echo power versus delay; it contains also a lunar comparison curve.

Schematically the back-scattering function can be regarded to result from two types of reflection: quasi-specular reflection, predominant at small ϕ, which provides a clue to the r.m.s. slope on a scale large compared to the wavelength applied, and diffuse reflection, important at large ϕ, and indicative of roughness on a smaller scale. The slope of $P(\phi)$ of Venus at small ϕ in both Figures IIIB2 and IIIB3 is steeper than that of the corresponding lunar curves, suggesting a smoother surface for Venus; the r.m.s. slope inferred from $P(\phi)$ is $\sim 5°$ for Venus, versus $\sim 8°$ for the moon [Carpenter, 1964].

Besides the information on small-scale roughness provided by the diffuse component of $P(\phi)$, additional knowledge is gained from the depolarization of the reflected signal. Reflection by a smooth surface reverses the polarization of the incident signal, whereas the presence of small scale irregularities (compared to the wavelength), or of multiple scattering destroys this simple relationship. Evidence from all above sources points to a fraction of $\sim 1/10$ of the Venusian surface being rough on a scale small compared to decimeter wavelengths [Carpenter, 1966].

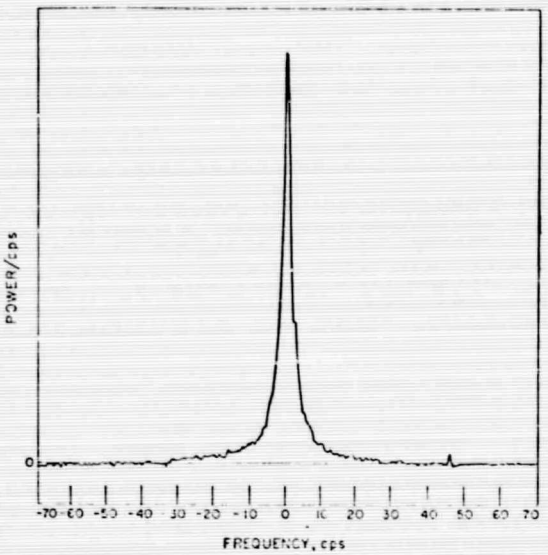

FIGURE IIIB1 - CW RADAR SPECTRUM OF VENUS FOR JULY 19, 1964. THE SPIKE AT +46 CPS IS A FREQUENCY CALIBRATION MARK. (FROM CARPENTER, 1966).

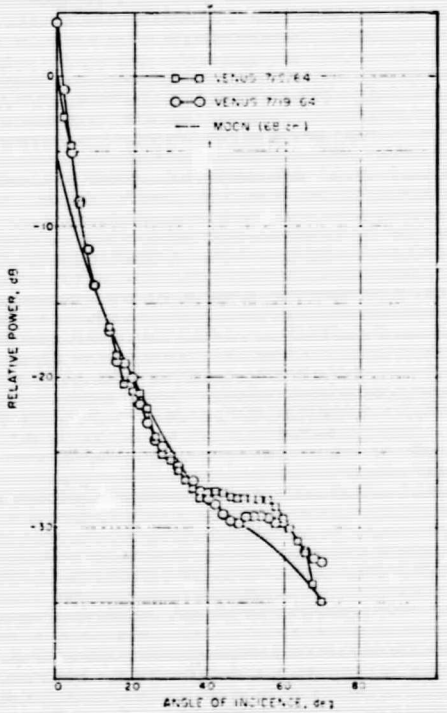

FIGURE IIIB2 - P (ϕ), BACKSCATTERING FUNCTION OF VENUS, COMPUTED FROM SPECTRA AS SHOWN IN FIGURE IIIB1. THE SMOOTH CURVE IS FOR THE MOON ALL THREE CURVES HAVE BEEN SHIFTED TO MATCH AT 10°.

Mean characteristic properties of Venusian *surface relief on a larger scale* are inferred from the striking periodicity of the radar cross section, σ_r, at 7.8 m [James et al., 1967]. The characteristic period over which σ_r oscillates between extremes of 0.03 and 0.5 appears to lend itself to an interpretation in terms of a gently sloped corrugated planetary surface with peak altitudes similar to those of terrestrial mountain peaks, and peak to peak separation of ∿1000 km. Such a structure is not incompatible with radar echo delay measurements of the radius of Venus [Ash et al., 1968].

Strong evidence for the presence of distinct and permanent *surface features* is drawn from anomalous radar echos returned by localized regions on Venus. These have been observed independently by a number of investigators at different wavelengths [Goldstein, 1965; Carpenter, 1966; Rogers et al., 1968]; the coordinate system used is that defined by Carpenter [1966].

Table IIIB.1

Location of Radar Features on Venus

Feature	Location from Lincoln Lab Observations °lat.	°long.	Probable JPL identification	Location from JPL Observations °lat.	°long.
H I	-26±3	-1±2	Go α	-29±2	0±?
H II	+24±2	-81±2	Go β	±23±4	-78+6
H III	+31±2	-78±2	None		
H IV	-7+3	-65±3	Ca C	-6.8±5.8	-68.9±1.3
H A	+23±2	-68±2	Ca D_2	-22.7+1.7	-70.0±0.7
H B	-12±3	-81±3	Ca B_1	-11.9±4.4	-75.8±0.6
H C	-13±2	-36±3	None		
H D	+10±4	-39±4	None		

H - Haystack

Go - Goldstein

Ca - Carpenter

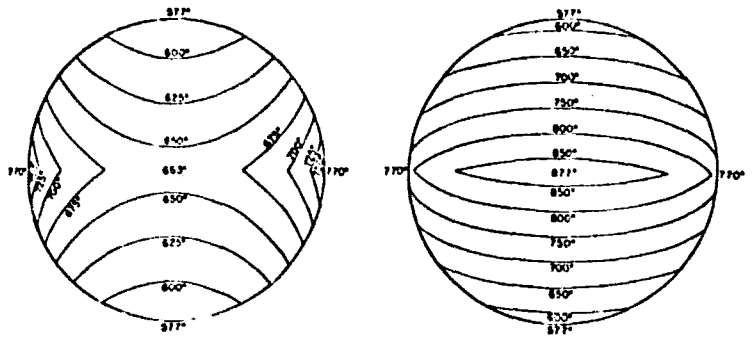

FIGURE IIIB4 - TYPICAL MODEL MAP OF ISOTHERMS ON VENUS. LEFT FIGURE - DARK SIDE; RIGHT FIGURE - SUNLIT SIDE (AFTER POLLACK AND SAGAN, 1965b).

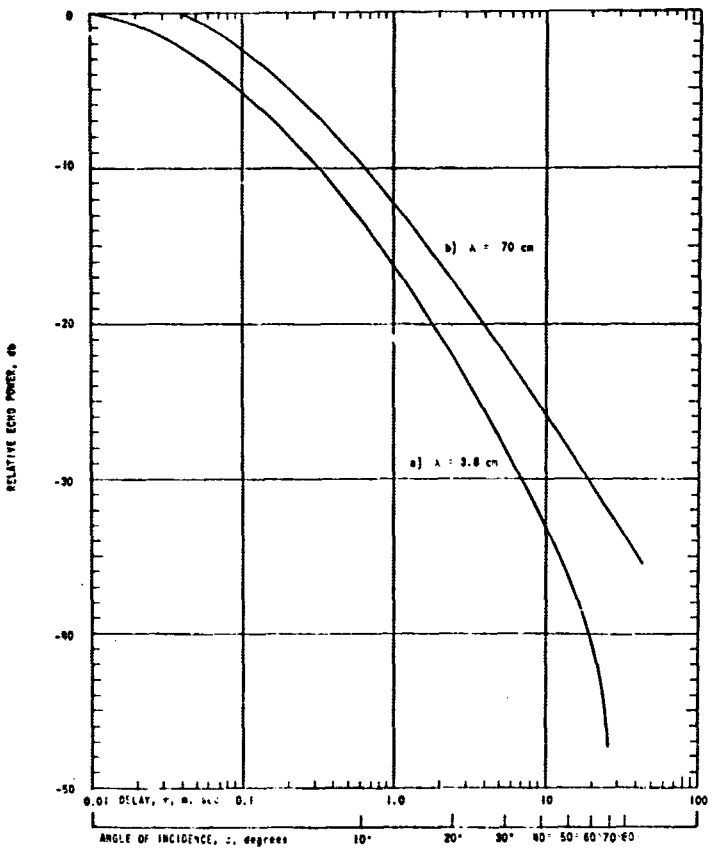

FIGURE IIIB3 - THE MEAN RADAR ANGULAR POWER SPECTRUM OF VENUS AT 3.8 CM AND 70 CM WAVELENGTHS. THE ABCISSA IS LABELLED IN TERMS OF BOTH TIME DELAY AND ANGLE OF INCIDENCE. THE NORMALIZATION OF EACH CURVE IS ARBITRARY (PETTENGILL ET AL., 1967)

(c) SURFACE COMPOSITION AND TEXTURE

For want of other reliable empirical data, the best indicator of Venus surface composition and texture is the dielectric constant, ε, deduced from the observed radar reflectivity of the planet [See Sec. (IIA)(e)]. Though no universal agreement exists with respect to the value of ε -- estimates ranging from as low as 2.2 to as high as 7.1 [Francis, 1965] -- a value of 4-5 appears most realistic, when atmospheric attenuation and surface roughness effects are correctly accounted for [Evans, 1968]. If the surface of Venus is solid, such values of ε suggest a surface consisting of compacted rocky material, less porous than lunar surface material [Evans et al., 1965]. Extensive bodies of water appear to be ruled out, in view of the likely value of ε as well as for other reasons [See Sec. (IIIC)(a)], but oceans of hydrocarbons are not excluded on the strength of their reflecting properties alone.

Though attempts have been made to closely circumscribe the composition and texture of Venusian surface material [Mueller, 1964; Pollack and Sagan, 1965], the conclusions drawn in these references do not rest on firm empirical evidence. The most likely composition of the surface of Venus appears, therefore, to be a combination of dry compact silicates and carbonates.

(d) THERMAL PROPERTIES

In view of the repeated radiometric observations of Venus in the microwave region [See Sec. (IIIA)(f)], and on account of the recent results from the Mariner V flyby and the Venera 4 descent, it appears virtually certain that the average Venus surface temperature is $\sim$600-650°K, or slightly higher.

The distribution of temperature over the surface of venus is not yet clearly resolved. The evidence from the microwave phase effect is controversial, and it is not yet clear, how much of the observed effect should be ascribed to the atmosphere [Hansen and Matsushima, 1967]. Radio interferometric studies of Venus support the presence of considerable dependence of temperature on longitude and latitude [Clark and Kuzmin, 1965], but need to be repeated in order to resolve remaining ambiguities.

Typical maps of Venus surface temperatures are presented in Figure IIIB4 [after Pollack and Sagan, 1965b], but have to be regarded with proper caution, before further empirical evidence attests their validity.

(IIIB) SURFACE PROPERTIES OF VENUS-REFERENCES

Ash, M. E., D. N. Campbell, R. B. Dyce, R. P. Ingalls, R. Jurgens, G. H. Pettengill, I. I. Shapiro, M. A. Slade and T. W. Thompson, "The case for the radar radins of Venus", Science, 160, 985-987, 1968.

Carpenter, R. L., "Studies of Venus by CW radar", Astron. J., 69, 2-11, 1964.

Carpenter, R. L., "Study of Venus by CW radar - 1964 results", Astron. J., 71, 142-152, 1966.

Clark, B. G. and A. D. Kuzmin, "Measurement of the polarization and brightness distribution of Venus at 10.6 cm wavelength', Astrophys. J., 143, 996-1000, 1965.

Evans, J. V., "Variations in the radar cross section of Venus", Astron. J., 73, 125-134, 1968.

Evans, J. V., R. A. Brockelman, J. C. Henry, G. M. Hyde, L. G. Kraft, W. A. Reid and W. W. Smith, "Radio echo observations of Venus and Mercury at 23 cm wavelength", Astron. J., 70, 486-501, 1965.

Goldstein, R. M., "Preliminary Venus radar results", Radio Science, 69D, 1623-1625, 1965.

Hansen, J. E. and S. Matsushima, "The atmosphere and surface temperature of Venus. A dust insulation model", Astrophys. J., 150, 1139-1157, 1967.

James, J. C., R. P. Ingalls and L. P. Rainville, "Radar echos from Venus at 38 Mc/sec", Astron. J., 72, 1067-1050, 1967.

Mueller, R. F., "A chemical model for the lower atmosphere of Venus", Icarus, 3, 285-298, 1964.

Pettengill, G. H., R. B. Dyce and D. B. Campbell, "Radar Measurements at 70 cm of Venus and Mercury", Astron. J., 72, 330-337, 1967.

Pollack, J. B. and C. Sagan, "The microwave phase effect of Venus", Icarus, 4, 62-103, 1965a.

Rogers, A. E. E., T. Hagfors, R. A. Brockelman, R. P. Ingalls, J. I. Levine, G. H. Pettengill, F. S. Weinstein, "A radar interferometer study of Venus at 3.8 cm", Lincoln Laboratory Tech. Rep. No. 444, Lincoln Laboratory, M. I. T., 1968.

(IIIC) ATMOSPHERIC PROPERTIES OF VENUS

(a) COMPOSITION

The recent in-situ analysis by Venera 4 [Vinogradov, 1968] has firmly established CO_2 as the major constituent of the sensible atmosphere of Venus, amounting to at least ∿8%, and probably no less than 90%, of the gases present in it. This is in agreement with results deduced from the Mariner V S-band oscillation experiment, and is consistent with earlier spectroscopic observations, which failed to identify any other major component in the atmosphere of Venus [Koenig et al., 1967].

It is not clear which gases make up the remainder of the Venusian atmosphere, apart from a number of constituents that have been identified in trace amounts - on the order of $\lesssim 10^{-3}$ fractional abundance - by either spectroscopic methods or through analysis aboard Venera 4. The presence of N_2 in substantial amounts is not yet ruled out, but the Venera 4 experiment set a limit of ∿7% to its fractional abundance. Likewise, the total mass of atmospheric gases is not known with certainty, in view of the discrepancies between the Venera 4 results, and conclusions drawn from the Mariner V experiment, to be discussed in greater detail in section (IIIC) (c).

Table IIIC.1 presents a summary of estimates of fractional abundance, reported recently by various investigators [2nd Arizona Conference on Planetary Atmospheres, 1968].

The chemical composition of the ionosphere, deduced from the observed electron concentration above ∿100 km and its altitude profile, appears to change from a preponderance of CO^+ ions at lower altitudes to the overwhelming abundance of protons beyond an altitude of 750 km [Mariner Stanford Group, 1967].

Table IIIC.1

Fractional abundance of molecular species in the atmosphere of Venus

Species	%	Source
CO_2	∿90	Vinogradov
N_2	<7	"
H_2O	.04<.?<.7	"
He	.01	McElroy
CO	∿.0045	Benedict
O_2	∿.003	Hunten
HCl	∿.0001	Benedict
CH_4	<.00007	Kuiper
COS	<.00005	"
N_2O	<.00005	Benedict
NH_3	<.000005	"
HF	<.000001	"

(b) TEMPERATURE PROFILE

The temperature profile of the Venusian atmosphere appears to be well established down to the level where the temperature reaches ∿550°K. This profile is based on various astronomical observations, the results of Mariner V, and in-situ measurements by Venera 4 [De Vaucouleurs and Menzel, 1959; Kaplan, 1962; 2nd Arizona Conference on Planetary Atmospheres, 1968; McElroy, 1968]. The altitude of the 550°K level is, however, not firmly determined, nor is the variation of temperature below it well understood in a form compatible with the absorption properties of the predominantly CO_2 atmosphere in the microwave region [Ho et al., 1966; Gale et al., 1968; Thaddeus, 1968].

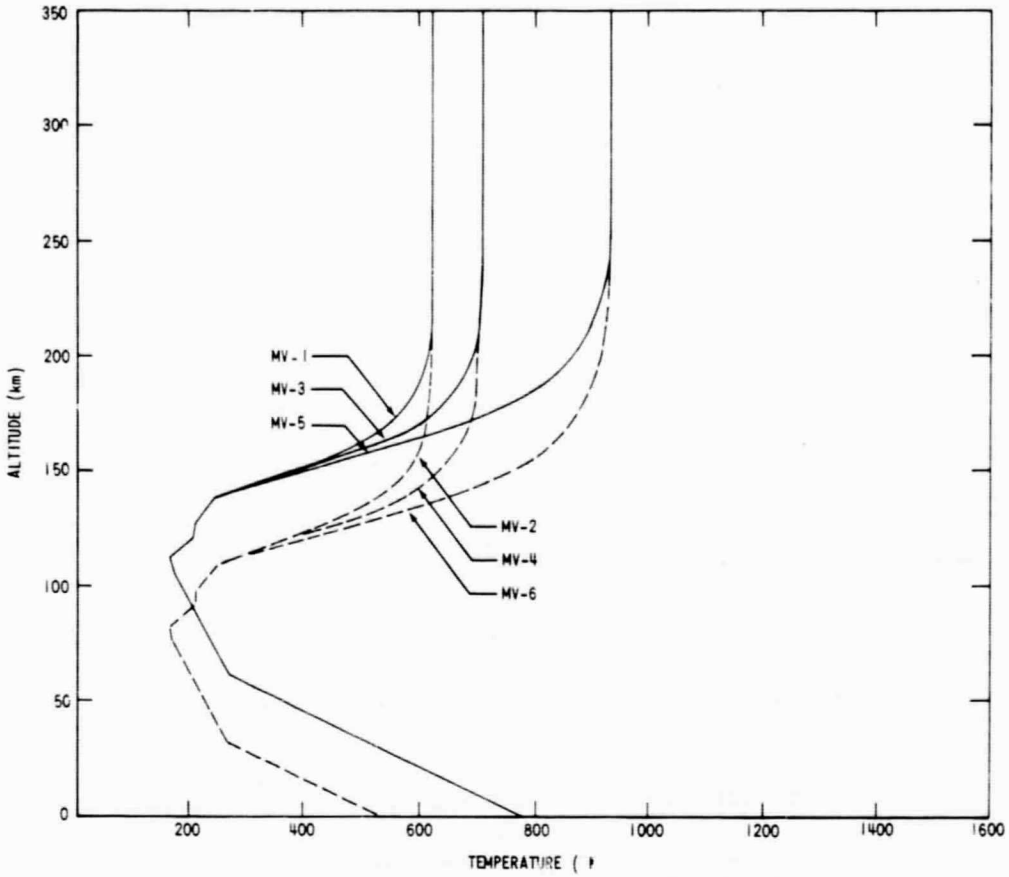

FIGURE IIIC1. - ATMOSPHERIC TEMPERATURE PROFILE OF VENUS
(AFTER NASA, 1968)

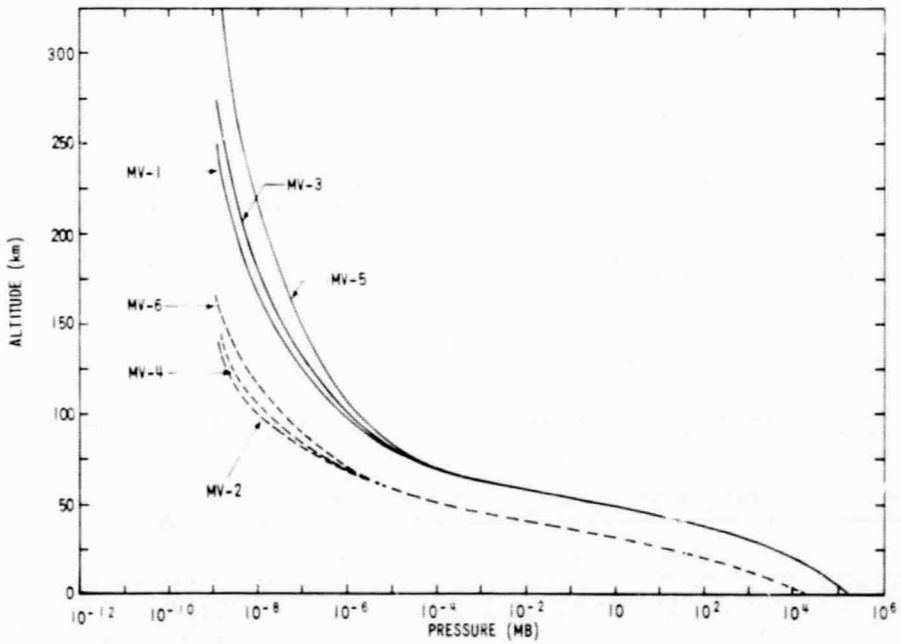

FIGURE IIIC2. - ATMOSPHERIC PRESSURE PROFILE OF VENUS
(MODELS MV-1 THROUGH MV-6 FROM NASA, 1968)

This uncertainty is reflected in the low altitude portion of the Venusian model atmosphere temperature profiles shown in Figure IIIC1. At altitudes above the 550°K level the temperature variation presented rests on a firmer empirical basis [see above]. The diverging curves at high altitudes show the dependence of temperature in the upper atmosphere on the variation in solar ultraviolet flux [NASA Design Criteria, 1968].

(c) PRESSURE AND DENSITY PROFILES

The full extent of present uncertainty about the properties of the Venusian atmosphere is manifest in the lower altitude portion of the pressure and density profiles, presented in Figures IIIC2 and IIIC3 [adopted from NASA Design Criteria, 1968]. The estimated surface pressure ranges from ∿16.5 to ∿165 earth atmospheres, depending on the interpretation of the Mariner V and Venera IV results, and their assumed correlation with the radar measurements of the planetary radius.

Venera 4 was deployed into the atmosphere from an altitude above the surface marked by a radar altitude marker as ∿26±1.3 km [Avduevskiy et al., 1968]. From there on, for a period of ∿94 minutes, until loss of radio contact with the probe, atmospheric parameters were monitored by the probe: temperature was measured over the entire period of descent, and a final reading of ∿544°K was obtained; pressure and density were directly measured down to levels where their ambient values exceeded the probe's instrumental limits. The Venera 4 pressure and density data below those levels are results of extrapolation, which yielded for the terminal pressure a value of ∿16.5-∿20.5 at. The total path covered by the probe in the atmosphere was deduced from the time sequence of measured atmospheric parameter values, and the known aerodynamic properties of the probe. The path length, so obtained, was 28±1 km, consistent with the assumption that Venera 4 did, indeed, land on the planet's surface.

Mariner V, on the other hand, performed a measurement of the atmospheric refractivity profile, as a function of distance from the center of Venus, and not of altitude above the surface [Kliore et al., 1967]. This profile was obtained only down to the level at which the refractivity becomes critical, corresponding to a pressure of ∿5 at and a planetocentric distance of ∿6092 km.

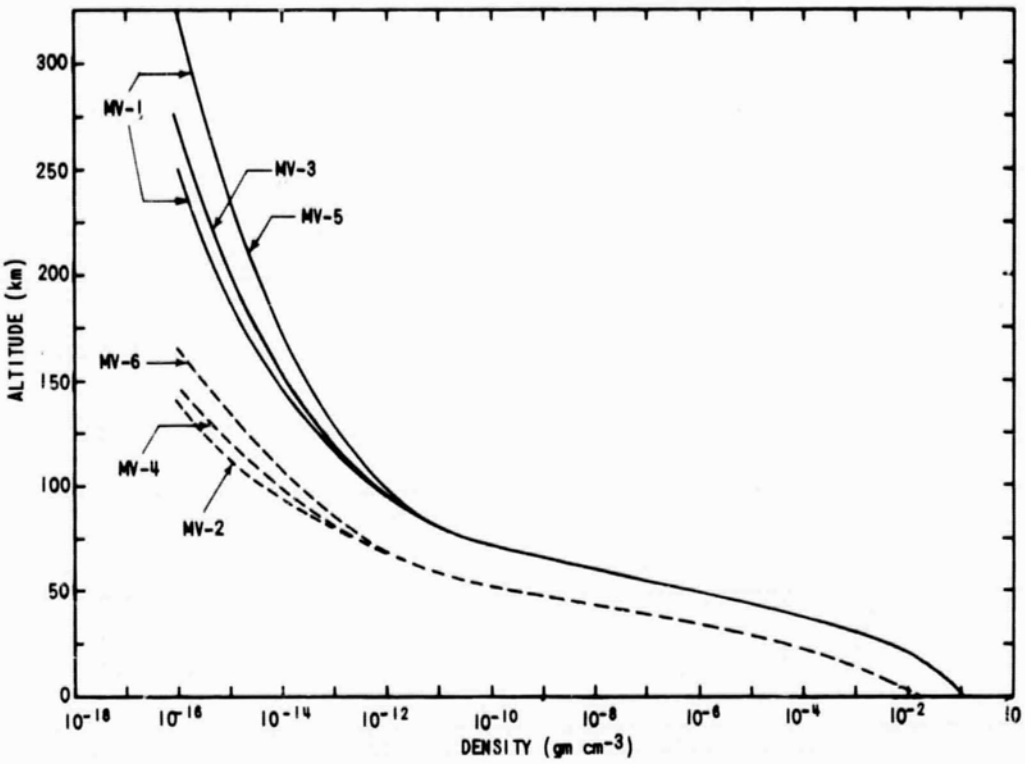

FIGURE IIIC3. - ATMOSPHERIC DENSITY PROFILE OF VENUS (MODELS MV-1 - MV-6 FROM NASA, 1968)

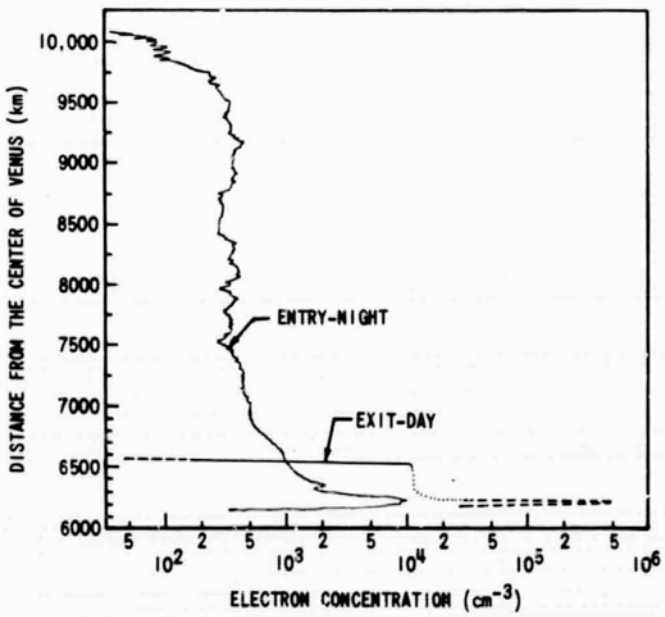

FIGURE IIIC4 - IONOSPHERIC ELECTRON PROFILES OF VENUS (AFTER MARINER STANFORD GROUP, 1967)

According to the Venera 4 results this pressure level is at an elevation of ∿14 km above the surface. This, however, is in conflict with the ∿5056 km radar radius of Venus [see Sec. (IIIA) (e)], which indicates that a distance of ∿6092 km corresponds to an altitude of ∿36 km above the planet's surface, and not 14 km. Though it is not ruled out, that Venera 4 landed at an elevated region of the surface, the required altitude of 22 km is contradicted by all other evidence from radar observations. A widely accepted solution to this dilemma is the assumption that contact with Venera 4 was lost when the latter was at an altitude of ∿22 km, and had not yet reached the surface. The question is, however, not yet completely settled.

The range of values of Venusian atmospheric parameters that has to be taken into account in view of the uncertainty, discussed above, is presented in Tables IIIC.2-III7 [adopted from NASA Design Criteria, 1968].

(d) IONOSPHERE

Thanks to the Mariner V dual-frequency occultation experiment [Mariner Stanford Group, 1967] the ionospheric structure of Venus is relatively well explored. It displays a striking differences between the bright and dark hemispheres of the planet, which is illustrated in Figure IIIC4. As a result of presumed interaction with the solar wind the daytime ionosphere terminates abruptly at a distance of ∿500 km from the surface. The observed peak electron density, at ∿150 km, was $\sim 5 \times 10^5$ cm^{-3}. On the night side the electron density reached a maximum of $\sim 10^4$ cm^{-3} at a similar altitude, but did not lapse to the interplanetary level of ∿10 cm^{-3} below a distance of ∿3500 km from the surface.

(e) CLOUDS AND HAZE

The high visual albedo of Venus (∿.73), and its featureless appearance in near infrared and red light favor the assumption that the planet is shrouded in a thick permanent cloud layer. The nature of the clouds, and the composition as well as characteristic dimensions of the cloud particles, are still subject to uncertainty [Koenig et al., 1967].

At shorter wavelengths, and especially in the ultraviolet, strongly time dependent markings have been observed [Smith, 1967], which may indicate the presence of atmospheric motion at the levels penetrated by these observations.

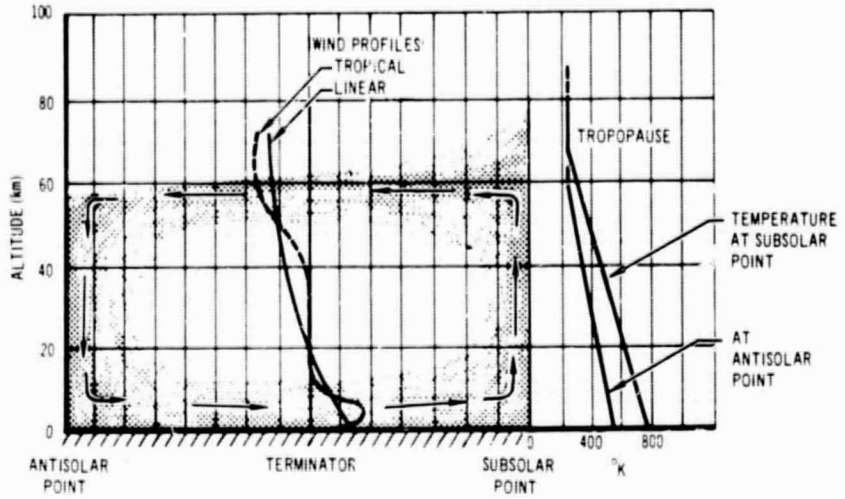

FIGURE IIIC5. - SUGGESTED CIRCULATION IN THE ATMOSPHERE OF VENUS (AFTER KOENIG ET AL., 1967)

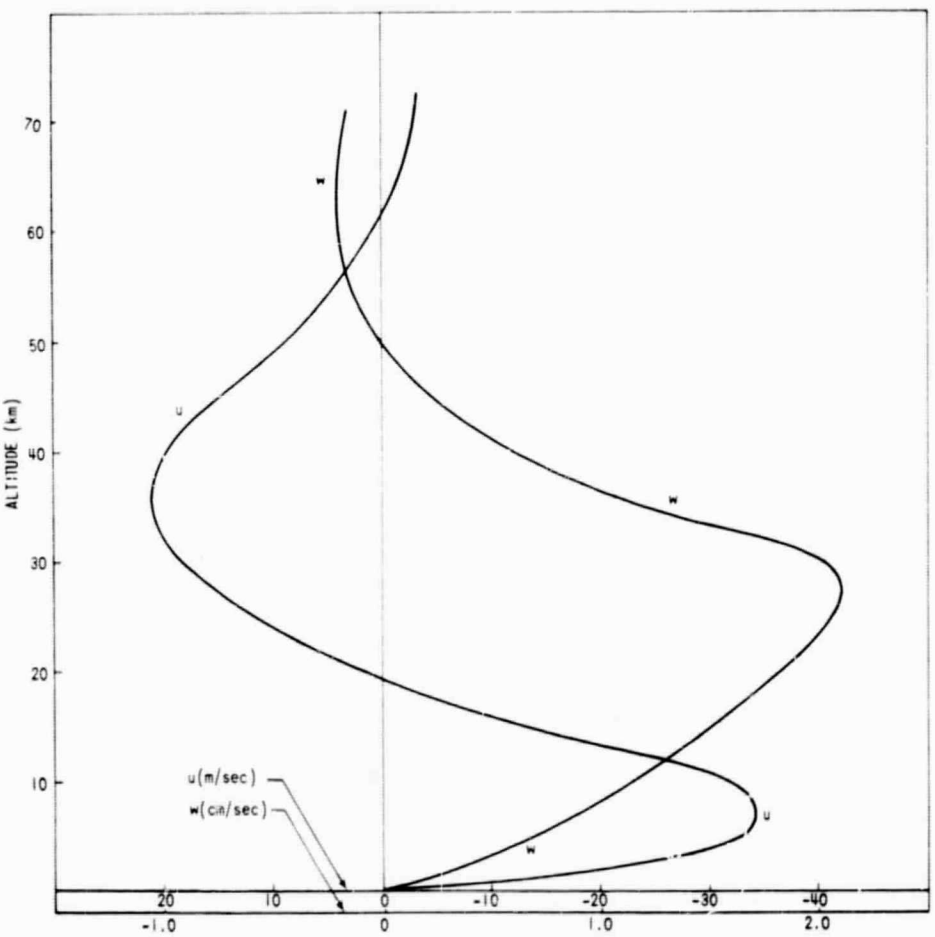

FIGURE IIIC6. - COMPUTED HORIZONTAL AND VERTICAL (U AND w) WIND VELOCITIES FOR VENUS (AFTER OHRING ET AL., 1965).

(f) CIRCULATION AND WINDS

The absence of any observational data on the nature of meteorological processes in the atmosphere of Venus, coupled with the lack of firm data on the temperature distribution at the surface, permits only highly conjectural predictions on circulation patterns and winds. If substantial polar cooling is absent, and the Coriolis acceleration can be neglected on account of Venus' slow rotation, a symmetric circulation pattern appears plausible, with hot gases rising at the subsolar point, and, after cooling, descending at the antisolar point [see Figure IIIC 5].

Maximum wind velocities have been calculated [Ohring et al., 1965] on the assumption of a synchronous rotation period for Venus, by means of a linearized flow model, including further simplifying approximations. The results of this model computation are shown in Figure IIIC 6; in view of the tentative character of their underlying assumptions, these results should be regarded with proper caution.

(g) ATTENTUATION OF HIGH FREQUENCY RADIO WAVES

On account of the observed variation with frequency of the microwave temperature of Venus and its radar cross section, noticeable attenuation may be attributed to the atmosphere in the S, X, and K frequency bands. The attenuation at normal incidence may be expressed as (Gale et al., 1968)

$$\Delta A = 75/\lambda^2 \quad \text{in dB}$$

where λ is measured in cm.

TABLE III C.2

NASA VENUS MODEL ATMOSPHERE MV-1 HIGH

DENSITY, MINIMUM SOLAR ACTIVITY

Altitude (km)	Temperature (°K)	Pressure (mb)	Density (gm cm^{-3})	Speed of Sound (m sec^{-1})	Molecular Weight (gm $mole^{-1}$)	Density Scale Height (km)	Number Density (cm^{-3})	Mean Free Path (m)	Viscosity (kg $m^{-1} sec^{-1}$)
0	770.0	1.69E 05	1.07E-01	425.	40.9	21.49	1.59E 21	9.45E-10	3.24E-05
5	733.3	1.27E 05	8.46E-02	422.	40.9	20.74	1.26E 21	1.20E-09	3.13E-05
10	696.6	9.39E 04	6.60E-02	415.	40.9	19.62	9.76E 20	1.54E-09	3.03E-05
15	660.0	6.81E-04	5.08E-02	404.	40.9	18.52	7.48E 20	2.02E-09	2.91E-05
20	619.9	4.85E 04	3.85E-02	393.	40.9	17.50	5.67E 20	2.66E-09	2.78E-05
25	579.9	3.38E 04	2.87E-02	381.	40.9	16.40	4.22E 20	3.57E-09	2.64E-05
30	540.0	2.29E 04	2.09E-02	368.	40.9	15.30	3.08E 20	4.90E-09	2.51E-05
35	494.1	1.51E 04	1.50E-02	354.	40.9	14.51	2.21E 20	6.81E-09	2.35E-05
40	448.3	9.55E 03	1.05E-02	338.	40.9	13.19	1.54E 20	9.77E-09	2.17E-05
45	402.6	5.75E 03	7.03E-03	322.	40.9	11.87	1.03E 20	1.46E-08	1.99E-05
50	357.0	3.26E 03	4.50E-03	305.	40.9	10.54	6.62E 19	2.28E-08	1.77E-05
60	273.3	8.15E 02	1.47E-03	270.	40.9	6.64	2.16E 19	6.98E-08	1.39E-05
70	255.8	1.62E 02	3.12E-04	263.	40.9	6.32	4.59E 18	3.28E-07	1.31E-05
80	231.1	2.81E 01	5.99E-05	251.	40.9	5.77	8.82E 17	1.71E-06	1.19E-05
90	207.9	4.03E 00	9.55E-06	240.	40.9	5.16	1.41E 17	1.07E-05	1.09E-05
100	185.7	4.67E-01	1.24E-06	195.	40.9	4.62	1.82E 16	8.26E-05	0.96E-05
120	203.3	4.22E-03	1.02E-08	237.	40.9	4.30	1.50E 14	1.00E-02	1.07E-05
140	265.8	9.46E-05	1.75E-10	271.	40.9	5.38	2.58E 12	5.85E-01	1.35E-05
160	471.9	9.37E-06	9.29E-12	358.	38.9	9.55	1.44E 11	1.05E 01	2.26E-05
180	583.8	2.30E-06	1.67E-12	420.	35.1	14.04	2.86E 10	5.27E 01	2.66E-05
200	612.7	7.67E-07	4.62E-13	453.	30.7	17.04	9.06E 09	1.66E 02	2.75E-05
220	620.4	3.06E-07	1.56E-13	492.	26.3	19.97	3.57E 09	4.22E 02	2.78E-05
240	621.5	1.40E-07	6.15E-14	531.	22.7	23.24	1.63E 09	9.22E 02	2.78E-05
260	621.8	7.15E-08	2.76E-14	565.	20.0	26.85	8.33E 08	1.81E 03	2.78E-05
280	622.1	3.93E-08	1.37E-14	595.	18.1	30.37	4.58E 08	3.29E 03	2.78E-05
300	622.4	2.29E-08	7.34E-15	621.	16.6	33.45	2.67E 08	5.65E 03	2.79E-05
320	622.7	1.40E-08	4.13E-15	647.	15.3	36.04	1.63E 08	9.27E 03	2.79E-05
340	623.0	8.89E-09	2.41E-15	675.	14.0	38.27	1.03E 08	1.46E 04	2.79E-05
360	623.3	5.90E-09	1.45E-15	709.	12.7	40.34	6.86E 07	2.20E 04	2.79E-05
380	623.6	4.09E-09	8.92E-16	753.	11.3	42.47	4.75E 07	3.17E 04	2.79E-05
400	623.9	2.97E-09	5.63E-16	807.	9.8	44.91	3.45E 07	4.36E 04	2.79E-05
420	624.1	2.26E-09	3.66E-16	874.	8.4	47.93	2.63E 07	5.74E 04	2.79E-05
440	624.4	1.80E-09	2.44E-16	953.	7.1	51.88	2.09E 07	7.23E 04	2.79E-05
460	624.7	1.48E 09	1.69E-16	1041.	5.9	57.17	1.72E 07	8.76E 04	2.79E-05
480	625.0	1.26E-09	1.21E-16	1134.	5.0	64.29	1.47E 07	1.03E 05	2.79E-05
500	625.3	1.10E-09	9.07E-17	1226.	4.3	73.78	1.28E 07	1.18E 05	2.80E-05

TABLE III C.3

NASA VENUS MODEL ATMOSPHERE MV-2

LOW DENSITY, MINIMUM SOLAR ACTIVITY

Altitude (km)	Temperature (°K)	Pressure (mb)	Density (gm cm^{-3})	Speed of Sound (m sec^{-1})	Molecular Weight (gm $mole^{-1}$)	Density Scale Height (km)	Number Density (cm^{-3})	Mean Free Path (m)	Viscosity (kg $m^{-1}sec^{-1}$)
0	534.0	1.67E 04	1.65E-0	351.	44.0	14.21	2.26E 20	6.38E-09	2.48E-05
5	489.2	1.06E 04	1.14E-0	337.	44.0	13.04	1.57E 20	9.21E-09	2.32E-05
10	444.4	6.43E 03	7.66E- 3	322.	44.0	11.87	1.05E 20	1.38E-08	2.13E-05
15	399.7	3.71E 03	4.91E- 3	307.	44.0	10.69	6.72E 19	2.14E-08	1.95E-05
20	355.1	2.01E 03	2.99E 3	291.	44.0	9.52	4.10E 19	3.52E-08	1.73E-05
25	310.6	1.00E 03	1.71E 03	274.	44.0	8.34	2.34E 19	6.17E-08	1.53E-05
30	273.3	4.51E 02	8.73E 04	259.	44.0	6.15	1.19E 19	1.21E-07	1.35E-05
35	265.0	1.92E 02	3.83E-04	256.	44.0	5.98	5.24E 18	2.75E-07	1.31E-05
40	255.8	7.94E 01	1.64E-04	252.	44.0	5.86	2.25E 18	6.41E-07	1.27E-05
45	244.1	3.17E 01	6.87E-05	247.	44.0	5.65	9.41E 17	1.53E-06	1.21E-05
50	231.1	1.21E 01	2.77E-05	241	44.0	5.35	3.79E 17	3.81E-06	1.15E-05
60	207.9	1.50E 00	3.81E-06	230.	44.0	4.78	5.22E 16	2.76E-05	1.05E-05
70	185.7	1.47E 01	4.20E-07	218.	44.0	4.28	5.75E 15	2.51E-04	0.92E-05
80	171.1	1.13E-02	3.51E-08	209.	44.0	3.84	4.80E 14	3.00E.03	0.82E-05
90	203.3	9.35E-04	2.43E-09	227.	44.0	4.03	3.33E 13	4.33E-02	1.04E-05
100	214.8	1.10E-04	2.71E-10	234.	44.0	4.70	3.72E 12	3.88E-01	1.08E-05
110	265.8	1.57E-05	3.13E-11	260.	44.0	5.06	4.29E 11	3.36E-00	1.31E-05
120	366.6	3.70E-06	5.33E-12	305.	44.0	6.54	7.30E 10	1.97E-01	1.78E-05
130	471.9	1.28E-06	1.43E-12	334.	43.9	8.98	1.96E 10	7.36E-01	2.24E-05
140	542.9	5.34E-07	5.18E-13	359.	43.8	11.15	7.12E 09	2.02E 02	2.51E-05
150	583.8	2.44E-07	2.19E-13	373.	43.6	12.39	3.03E 09	4.76E 02	2.65E-05
160	602.9	1.17E-07	1.01E-13	375.	43.2	13.10	1.40E 09	1.03E 03	2.71E-05
170	612.7	5.77E-08	4.81E-14	381.	42.5	13.72	6.82E 08	2.11E 03	2.75E-05
180	620.3	2.93E-08	2.33E-14	390.	41.1	14.20	3.42E 08	4.22E 03	2.77E-05
190	620.8	1.54E-08	1.16E-14	402.	38.8	14.34	1.80E 08	8.02E 03	2.77E-05
200	621.3	8.53E-09	5.76E-15	424.	34.9	14.55	9.94E 07	1.45E 04	2.77E-05
210	621.5	5.09E-09	2.91E-15	461.	29.5	14.88	5.94E 07	2.43E 04	2.78E-05
220	621.7	3.36E-09	1.49E-15	523.	22.9	15.41	3.91E 07	3.68E 04	2.78E-05
230	621.8	2.46E-09	7.85E-16	617.	16.5	16.31	2.87E 07	5.03E 04	2.78E-05
240	622.0	1.98E-09	4.32E-16	746.	11.3	17.88	2.31E 07	6.24E 04	2.78E-05
250	622.1	1.71E-09	2.55E-16	903.	7.7	20.70	1.99E 07	7.23E 04	2.78E-05
260	622.3	1.55E-09	1.64E-16	1069.	5.5	25.76	1.80E 07	8.01E 04	2.78E-05
270	622.4	1.43E-09	1.17E-16	1220.	4.2	34.59	1.67E 07	8.63E 04	2.78E-05
280	622.6	1.35E-09	9.18E-17	1336.	3.5	49.19	1.57E 07	9.16E 04	2.78E-05

TABLE III C.4

NASA VENUS MODEL ATMOSPHERE MV-3

HIGH DENSITY, MEAN SOLAR ACTIVITY

Altitude (km)	Temperature (°K)	Pressure (mb)	Density (gm cm^{-3})	Speed of Sound (m sec^{-1})	Molecular Weight (gm $mole^{-1}$)	Density Scale Height (km)	Number Density (cm^{-3})	Mean Free Path (m)	Viscosity (kg $m^{-1} sec^{-1}$)
0	770.0	1.69E 05	1.07E-01	425.	40.9	21.49	1.59E 21	9.45E-10	3.24E-05
5	733.3	1.27E 05	8.46E-02	422.	40.9	20.74	1.26E 21	1.20E-09	3.13E-05
10	696.6	9.39E 04	6.60E-02	415.	40.9	19.62	9.76E 20	1.54E-09	3.03E-05
15	660.0	6.81E 04	5.08E-02	404.	40.9	18.52	7.48E 20	2.02E-09	2.91E-05
20	619.9	4.85E 04	3.85E-02	393.	40.9	17.50	5.67E 20	2.66E-09	2.78E-05
25	579.9	3.38E 04	2.87E-02	381.	40.9	16.40	4.22E 20	3.57E-09	2.64E-05
30	540.0	2.29E 04	2.09E-02	368.	40.9	15.30	3.08E 20	4.90E-09	2.51E-05
35	494.1	1.51E 04	1.50E-02	354.	40.9	14.51	2.21E 20	6.81E-09	2.35E-05
40	448.3	9.55E 03	1.05E-02	338.	40.9	13.19	1.54E 20	9.77E-09	2.17E-05
45	402.6	5.75E 03	7.03E-03	322.	40.9	11.87	1.03E 20	1.46E-08	1.99E-05
50	357.0	3.26E 03	4.50E-03	305.	40.9	10.54	6.62E 19	2.28E-08	1.77E-05
60	273.3	8.15E 02	1.47E-03	270.	40.9	6.64	2.16E 19	6.98E-08	1.39E-05
70	256.2	1.62E 02	3.12E-04	263.	40.9	6.30	4.59E 18	3.29E-07	1.31E-05
80	231.2	2.82E 01	6.01E-05	251.	40.9	5.81	8.85E 17	1.70E-06	1.19E-05
90	208.3	4.05E 00	9.58E-06	240.	40.9	5.17	1.41E 17	1.07E-05	1.09E-05
100	185.8	4.71E 01	1.25E-06	196.	40.9	4.64	1.84E 16	8.20E-05	0.96E-05
120	203.9	4.24E-03	1.02E-08	237.	40.9	4.39	1.51E 14	1.00E-02	1.08E-05
140	263.2	9.38E-05	1.75E-10	270.	40.9	5.18	2.58E 12	5.84E-01	1.34E-05
160	502.4	9.82E-06	9.16E-12	369.	39.0	9.65	1.42E 11	1.06E-01	2.38E-05
180	641.4	2.68E-06	1.78E-12	430.	35.6	14.97	3.02E 10	4.99E 01	2.85E-05
200	691.5	9.77E-07	5.39E-13	473.	31.7	18.55	1.02E 10	1.47E 02	3.01E-05
220	705.5	4.18E-07	1.98E-13	511.	27.8	21.56	4.29E 09	3.51E 02	3.06E-05
240	709.0	2.02E-07	8.32E-14	547.	24.3	24.69	2.06E 09	7.30E 02	3.07E-05
260	709.4	1.07E-07	3.90E-14	582.	21.5	28.24	1.09E 09	1.38E 03	3.07E-05
280	709.6	6.10E-08	2.01E-14	613.	19.4	31.90	6.23E 08	2.42E 03	3.07E-05
300	709.8	3.66E-08	1.11E-14	639.	17.8	35.38	3.74E 08	4.03E 03	3.07E-05
320	709.9	2.30E-08	6.44E-15	664.	16.6	38.44	2.34E 08	6.43E 03	3.07E-05
340	710.1	1.49E-08	3.89E-15	687.	15.4	41.08	1.52E 08	9.92E 03	3.07E-05
360	710.2	9.98E-09	2.43E-15	713.	14.4	43.38	1.02E 08	1.48E 04	3.07E-05
380	710.4	6.90E-09	1.55E-15	743.	13.2	45.50	7.04E 07	2.14E 04	3.07E-05
400	710.5	4.94E-09	1.01E-15	779.	12.0	47.60	5.03E 07	2.99E 04	3.07E-05
420	710.7	3.65E-09	6.66E-16	823.	10.8	49.86	3.72E 07	4.05E 04	3.07E-05
440	710.8	2.80E-09	4.50E-16	877.	9.5	52.46	2.86E 07	5.28E 04	3.07E-05
460	711.0	2.22E-09	3.10E-15	941.	8.2	55.64	2.27E 07	6.65E 04	3.07E-05
480	711.1	1.82E-09	2.19E-16	1014.	7.1	59.66	1.86E 07	8.11E 04	3.07E-05
500	711.2	1.54E-09	1.59E-16	1095.	6.1	64.83	1.57E 07	9.61E 04	3.07E-05
550	711.6	1.11E-09	8.04E-17	1308.	4.3	85.29	1.13E 07	1.33E 05	3.07E-05

TABLE III C.5

NASA VENUS MODEL ATMOSPHERE MV-4

LOW DENSITY, MEAN SOLAR ACTIVITY

Altitude (km)	Temperature (°K)	Pressure (mb)	Density ($gm\ cm^{-3}$)	Speed of Sound ($m\ sec^{-1}$)	Molecular Weight ($gm\ mole^{-1}$)	Density Scale Height (km)	Number Density (cm^{-3})	Mean Free Path (m)	Viscosity ($kg\ m^{-1} sec^{-1}$)
0	534.0	1.67E 04	1.65E-02	351.	44.0	14.21	2.26E 20	6.68E-09	2.48E-05
5	489.2	1.06E 04	1.14E-02	337.	44.0	13.04	1.57E 20	9.21E-09	2.32E-05
10	444.4	6.43E 03	7.66E-03	322.	44.0	11.87	1.05E 20	1.38E-08	2.13E-05
15	399.7	3.71E 03	4.91E-03	307.	44.0	10.69	6.72E 19	2.14E-08	1.95E-05
20	355.1	2.01E 03	2.99E-03	291.	44.0	9.52	4.10E 19	3.52E-08	1.73E-05
25	310.6	1.00E 03	1.71E-03	274.	44.0	8.34	2.34E 19	6.17E-08	1.53E-05
30	273.3	4.51E 02	8.73E-04	259.	44.0	6.15	1.19E 19	1.21E-07	1.35E-05
35	265.4	1.92E 02	3.82E-04	256.	44.0	5.97	5.23E 18	2.75E-07	1.31E-05
40	256.2	7.95E 01	1.64E-04	252.	44.0	5.84	2.25E 18	6.42E-07	1.27E-05
45	244.3	3.18E 01	6.89E-05	247.	44.0	5.65	9.43E 17	1.53E-06	1.21E-05
50	231.2	1.21E 01	2.78E-05	241.	44.0	5.37	3.80E 17	3.79E-06	1.15E-05
60	208.3	1.50E 00	3.82E-06	230.	44.0	4.79	5.23E 16	2.75E-05	1.06E-05
70	185.8	1.49E-01	4.24E-07	218.	44.0	4.30	5.80E 15	2.49E-04	0.92E-05
80	171.0	1.15E-02	3.55E-08	209.	44.0	3.84	4.86E 14	2.97E-03	0.82E-05
90	203.9	9.39E-04	2.44E-09	228.	44.0	4.11	3.34E 13	4.32E-02	1.04E-05
100	211.4	1.11E-04	2.78E-10	232.	44.0	4.60	3.81E 12	3.78E-01	1.07E-05
110	263.2	1.56E-05	3.14E-11	259.	44.0	4.87	4.30E 11	3.36E 00	1.30E-05
120	378.4	3.71E-06	5.19E-12	310.	44.0	6.47	7.11E 10	2.03E 01	1.84E-05
130	502.4	1.35E-06	1.42E-12	345.	43.9	9.12	1.95E 10	7.39E 01	2.37E-05
140	591.0	6.02E-07	5.37E-13	375.	43.8	11.58	7.38E 09	1.95E 02	2.67E-05
150	641.4	2.95E-07	2.41E-13	385.	43.7	13.34	3.33E 09	4.33E 02	2.84E-05
160	674.9	1.52E-07	1.17E-13	396.	43.4	14.65	1.63E 09	8.86E 02	2.96E-05
170	691.5	8.05E-08	6.01E-14	403.	42.9	15.31	8.44E 08	1.71E 03	3.01E-05
180	700.8	4.38E-08	3.16E-14	410.	42.0	15.75	4.52E 08	3.19E 03	3.04E-05
190	705.5	2.44E-08	1.69E-14	419.	40.6	16.13	2.50E 08	5.76E 03	3.06E-05
200	707.8	1.40E-08	9.10E-15	432.	38.3	16.37	1.43E 08	1.01E 04	3.06E-05
210	709.0	8.37E-09	4.95E-15	453.	34.8	16.63	8.56E 07	1.68E 04	3.07E-05
220	709.4	5.32E-09	2.72E-15	487.	30.1	16.98	5.43E 07	2.65E 04	3.07E-05
230	709.4	3.64E-09	1.51E-15	540.	24.5	17.46	3.72E 07	3.88E 04	3.07E-05
240	709.5	2.70E-09	8.57E-16	618.	18.7	18.22	2.76E 07	5.23E 04	3.07E-05
250	709.6	2.16E-09	5.00E-16	725.	13.6	19.45	2.21E 07	6.52E 04	3.07E-05
260	709.7	1.85E-09	3.04E-16	858.	9.7	21.49	1.88E 07	7.65E 04	3.07E-05
270	709.8	1.65E-09	1.96E-16	1010.	7.0	24.89	1.68E 07	8.57E 04	3.07E-05
280	709.8	1.52E-09	1.36E-16	1163.	5.3	30.54	1.55E 07	9.31E 04	3.07E-05
290	709.9	1.42E-09	1.02E-16	1302.	4.2	39.68	1.45E 07	9.93E 04	3.07E-05

TABLE III C.6

NASA VENUS MODEL ATMOSPHERE MV-5

HIGH DENSITY, MAXIMUM SOLAR ACTIVITY

Altitude (km)	Temperature (°K)	Pressure (mb)	Density ($gm\ cm^{-3}$)	Speed of Sound ($m\ sec^{-1}$)	Molecular Weight ($gm\ mole^{-1}$)	Density Scale Height (km)	Number Density (cm^{-3})	Mean Free Path (m)	Viscosity ($kg\ m^{-1} sec^{-1}$)
0	770.0	1.69E-05	1.07E-01	425.	40.9	21.49	1.59E 21	9.45E-10	3.24E-05
5	733.3	1.27E-05	8.46E-02	422.	40.9	20.74	1.26E 21	1.20E-09	3.13E-05
10	696.6	9.39E-04	6.60E-02	415.	40.9	19.62	9.76E 20	1.54E-09	3.03E-05
15	660.0	6.81E-04	5.08E-02	404.	40.9	18.52	7.48E 20	2.02E-09	2.91E-05
20	619.9	4.85E-04	3.85E-02	393.	40.9	17.50	5.67E 20	2.66E-09	2.78E-05
25	579.9	3.38E-04	2.87E-02	381.	40.9	16.40	4.22E 20	3.57E-09	2.64E-05
30	540.0	2.29E-04	2.09E-02	368.	40.9	15.30	3.08E 20	4.90E-09	2.51E-05
35	494.1	1.51E-04	1.50E-02	354.	40.9	14.51	2.21E 20	6.81E-09	2.35E-05
40	448.3	9.55E-03	1.05E-02	338.	40.9	13.19	1.54E 20	9.77E-09	2.17E-05
45	402.6	5.75E-03	7.03E-03	322.	40.9	11.87	1.03E 20	1.46E-08	1.99E-05
50	357.0	3.26E-03	4.50E-03	305.	40.9	10.54	6.62E 19	2.28E-08	1.77E-05
60	273.3	8.15E-02	1.47E-03	270.	40.9	6.64	2.16E 19	6.98E-08	1.39E-05
70	256.3	1.62E-02	3.12E-04	263.	40.9	6.33	4.59E 18	3.29E-07	1.31E-05
80	231.7	2.83E-01	6.01E-05	251.	40.9	5.79	8.84E 17	1.70E-06	1.20E-05
90	208.9	4.08E-00	9.62E-06	240.	40.9	5.18	1.42E 17	1.06E-05	1.10E-05
100	187.0	4.79E-01	1.26E-06	196.	40.9	4.64	1.85E 16	8.12E-05	0.97E-05
120	203.0	4.45E-03	1.08E-08	237.	40.9	4.31	1.59E 14	9.50E-03	1.07E-05
140	272.3	1.03E-04	1.86E-10	274.	40.9	5.41	2.73E 12	5.51E-01	1.38E-05
160	555.8	1.20E-05	1.02E-11	388.	39.1	9.76	1.57E 11	9.61E-00	2.56E-05
180	760.0	3.81E-06	2.18E-12	464.	36.2	16.22	3.63E 10	4.15E-01	3.21E-05
200	862.3	1.62E-06	7.52E-13	512.	33.2	21.13	1.36E 10	1.11E-02	3.50E-05
220	905.9	7.96E-07	3.19E-13	551.	30.2	25.09	6.37E 09	2.37E-02	3.62E-05
240	922.8	4.28E-07	1.52E-13	585.	27.2	28.60	3.36E 09	4.48E-02	3.66E-05
260	928.9	2.47E-07	7.86E-14	618.	24.6	32.09	1.93E 09	7.82E-02	3.68E-05
280	930.5	1.51E-07	4.36E-14	649.	22.3	35.76	1.18E 09	1.28E-03	3.69E-05
300	931.3	9.66E-08	2.56E-14	677.	20.5	39.47	7.51E 08	2.01E-03	3.69E-05
320	932.1	6.41E-08	1.58E-14	702.	19.1	43.20	4.98E 08	3.03E-03	3.69E-05
340	932.8	4.38E-08	1.01E-14	725.	17.9	46.74	3.40E 08	4.43E-03	3.69E-05
360	933.6	3.07E-08	6.69E-15	746.	16.9	49.99	2.38E 08	6.34E-03	3.69E-05
380	934.4	2.19E-08	4.53E-15	766.	16.1	52.91	1.70E 08	8.86E-03	3.70E-05
400	935.1	1.60E-08	3.14E-15	787.	15.2	55.53	1.24E 08	1.22E-04	3.70E-05
420	935.9	1.19E-08	2.20E-15	809.	14.4	57.93	9.19E 07	1.64E-04	3.70E-05
440	936.6	8.99E-09	1.57E-15	834.	13.6	60.19	6.95E 07	2.17E-04	3.70E-05
460	937.4	6.93E-09	1.13E-15	862.	12.7	62.40	5.35E 07	2.81E-04	3.71E-05
480	938.1	5.44E-09	8.26E-16	894.	11.8	64.64	4.20E 07	3.59E-04	3.71E-05
500	938.9	4.36E-09	6.10E-16	932.	10.9	67.03	3.36E 07	4.48E-04	3.71E-05
550	940.7	2.73E-09	2.99E-16	1052.	8.6	74.32	2.10E 07	7.17E-04	3.71E-05
600	942.5	1.91E-09	1.59E-16	1208.	6.5	85.20	1.47E 07	1.02E-05	3.72E-05
650	944.3	1.47E-09	9.28E-17	1386.	5.0	102.34	1.13E 07	1.34E-05	3.72E-05

TABLE III C.7

NASA VENUS MODEL ATMOSPHERE MV-6

LOW DENSITY, MAXIMUM SOLAR ACTIVITY

Altitude (km)	Temperature (°K)	Pressure (mb)	Density (gm cm^{-3})	Speed of Sound (m sec^{-1})	Molecular Weight (gm $mole^{-1}$)	Density Scale Height (km)	Number Density (cm^{-3})	Mean Free Path (m)	Viscosity (kg $m^{-1}sec^{-1}$)
0	534.0	1.67E 04	1.65E-02	351.	44.0	14.21	2.26E 20	6.38E-09	2.48E-05
5	489.2	1.06E 04	1.14E-02	337.	44.0	13.04	1.57E 20	9.21E-09	2.32E-05
10	444.4	6.43E 03	7.66E-03	322.	44.0	11.87	1.05E 20	1.38E-09	2.13E-05
15	399.7	3.71E 03	4.91E-03	307.	44.0	10.69	6.72E 19	2.14E-08	1.95E-05
20	355.1	2.01E 03	2.99E-03	291.	44.0	9.52	4.10E 19	3.52E-08	1.73E-05
25	310.6	1.00E 03	1.71E-03	274.	44.0	8.34	2.34E 19	6.17E-08	1.53E-05
30	273.3	4.51E 02	8.73E-04	259.	44.0	6.15	1.19E 19	1.21E-07	1.35E-05
35	265.2	1.92E 02	3.83E-04	256.	44.0	5.97	5.24E 18	2.75E-07	1.31E-05
40	256.3	7.95E 01	1.64E-04	252.	44.0	5.86	2.25E 18	6.42E-07	1.27E-05
45	244.6	3.18E 01	6.88E-05	247.	44.0	5.66	9.42E 17	1.53E-06	1.21E-05
50	231.7	1.21E 01	2.77E-05	241.	44.0	5.36	3.80E 17	3.80E-06	1.16E-05
60	208.9	1.52E 00	3.84E-06	230.	44.0	4.80	5.26E 16	2.74E-05	1.06E-05
70	187.0	1.51E-01	4.28E-07	218.	44.0	4.30	5.86E 15	2.46E-04	0.93E-05
80	172.5	1.19E-02	3.65E-08	210.	44.0	3.87	4.99E 14	2.89E-03	0.83E-05
90	203.0	9.88E-04	2.58E-09	227.	44.0	4.04	3.53E 13	4.09E-02	1.03E-05
100	216.7	1.18E-04	2.87E-10	235.	44.0	4.72	3.93E 12	3.66E-01	1.09E-05
110	272.3	1.72E-05	3.35E-11	263.	44.0	5.09	4.58E 11	3.15E-00	1.34E-05
120	399.3	4.31E-06	5.72E-12	319.	44.0	6.67	7.83E 10	1.84E-01	1.95E-05
130	555.8	1.68E-06	1.60E-12	363.	43.9	9.27	2.19E 10	6.59E-01	2.55E-05
140	675.4	8.14E-07	6.36E-13	394.	43.9	11.97	8.73E 09	1.65E-02	2.96E-05
150	760.0	4.41E-07	3.05E-13	418.	43.8	14.72	4.20E 09	3.43E-02	3.21E-05
160	826.0	2.53E-07	1.61E-13	433.	43.6	17.28	2.22E 09	6.49E-02	3.40E-05
170	862.3	1.51E-07	9.15E-14	444.	43.4	18.11	1.27E 09	1.14E-03	3.51E-05
180	890.2	9.24E-08	5.38E-14	453.	43.1	19.61	7.52E 08	1.92E-03	3.59E-05
190	905.9	5.74E-08	3.25E-14	459.	42.6	20.04	4.59E 08	3.14E-03	3.64E-05
200	916.7	3.63E-08	1.99E-14	466.	41.8	20.81	2.87E 08	5.03E-03	3.67E-05
210	922.8	2.33E-08	1.23E-14	474.	40.7	21.07	1.83E 08	7.89E-03	3.68E-05
220	926.8	1.52E-08	7.70E-15	485.	39.0	21.50	1.19E 08	1.21E-04	3.70E-05
230	928.9	1.02E-08	4.84E-15	500.	36.8	21.73	7.93E 07	1.82E-04	3.70E-05
240	930.1	7.00E-09	3.06E-15	522.	33.8	22.09	5.45E 07	2.64E-04	3.71E-05
250	930.5	5.00E-09	1.95E-15	553.	30.2	22.43	3.89E 07	3.70E 04	3.71E-05
260	930.9	3.73E-09	1.25E-15	596.	26.0	22.89	2.90E 07	4.97E 04	3.71E-05
270	931.3	2.91E-09	8.10E-16	655.	21.6	23.54	2.26E 07	6.37E 04	3.71E-05
280	931.7	2.38E-09	5.31E-16	730.	17.3	24.46	1.85E 07	7.80E 04	3.71E-05
290	932.1	2.03E-09	3.55E-16	825.	13.6	25.79	1.57E 07	9.15E 04	3.71E-05
300	932.5	1.79E-09	2.43E-16	937.	10.5	27.72	1.39E 07	1.04E 05	3.71E-05
310	932.8	1.63E-09	1.72E-16	1062.	8.2	30.57	1.26E 07	1.14E 05	3.71E-05
320	933.2	1.51E-09	1.26E-16	1194.	6.5	34.74	1.17E 07	1.23E 05	3.71E-05
330	933.6	1.42E-09	9.66E-17	1325	5.3	40.82	1.10E 07	1.31E 05	3.72E-05

(IIIC) ATMOSPHERIC PROPERTIES OF VENUS - REFERENCES

Avduevskiy, V. S., M. Ya. Marov and M. K. Rozhdestvenskiy, "The model of the planet Venus on the results of measurements made by the Soviet interplanetary station Venera 4", report at the 2nd Arizona Conference on Planetary Atmospheres, March 1968.

2nd Arizona Conference on Planetary Atmospheres, Tucson, Arizona, March 1968, J. Atmos. Sci., 25, pp. 533-671, 1968.

De Vaneouleurs, G. and D. H. Menzel, "Results of the occultation of Regulus by Venus", Nature, 188, 28-33, 1959.

Gale, W. A., M. Liwshitz and A. C. E. Sinclair, priv. communic.

Ho, W., I. A. Kaufman and P. Thaddeus, "Laboratory measurement of microwave absorption in models of the atmosphere of Venus", J. Geophys. Res., 71, 5091-5108, 1966.

Kaplan, L. D., "A preliminary model of the Venus atmosphere", JPL Tech. Rep. No. 32-379, 1962.

Koenig, L. R., F. W. Murray, C. M. Michaux and H. A. Hyatt, "Handbook of the physical properties of the planet Venus", NASA SP-3029, 1967.

Kliore, A., G. S. Levy, D. L. Cain, G. Fjeldbo and S. I. Rasool, "Atmosphere and ionosphere of Venus from the Mariner V S-band occultation measurement", Science, 158, 1683-1688, 1967.

Mariner Stanford Group, "Venus ionosphere and atmosphere as measured by dual-frequency radio occultation of Mariner V", Science, 158, 1678-1683, 1967.

McElroy, M. B., "The upper atmosphere of Venus", J. Geophys Res., 73, 1513-1521, 1968.

NASA Design Criteria, Venus model atmosphere 1968, in preparation.

Ohring, G., W. Tand and J. Marianok "Planetary meterology", NASA CR-280, 1965.

Smith, B. A., "Rotation of Venus: continuing contradictions", Science, 158, 114-116, 1967.

Thaddeus, P., personal communication, 1968.

Vinogradov, A. P., Report at the 2nd Arizona Conference on Planetary Atmospheres, 1968.